THESIS FOR THE DEGREE OF DOCTOR OF PHILOSOPHY

Chemical Transformation of Inorganic Species in Thermochemical Conversion of Waste-Derived Fuels

The Role of Oxygen Carriers

IVANA STANIČIĆ

Department of Space, Earth and Environment

CHALMERS UNIVERSITY OF TECHNOLOGY

Gothenburg, Sweden 2023

Chemical Transformation of Inorganic Species in Thermochemical Conversion of Waste-Derived Fuels

The Role of Oxygen Carriers

ISBN 978-91-7905-873-9

Doktorsavhandling vid Chalmers Tekniska Högskola

Ny serie nr 5339

ISSN 0346-718X

Department of Space, Earth and Environment

Division of Energy Technology

Chalmers University of Technology

SE-412 96 Gothenburg

Sweden

Telephone + 46 (0)31-772 1000

Cover:
Scanning Electron Microscopy (SEM) image of the surface of the oxygen carrier ilmenite.

Printed by Chalmers Reproservice

Gothenburg, Sweden 2023

Chemical Transformation of Inorganic Species in Thermochemical Conversion of Waste-Derived Fuels

The Role of Oxygen Carriers

IVANA STANIČIĆ

Division of Energy Technology
Department of Space, Earth and Environment
Chalmers University of Technology

Abstract

Waste-derived fuels are used increasingly in heat and power production systems in Sweden. Thermal conversion of waste-derived and biomass fuels offers the possibility of achieving carbon dioxide-neutral or even negative emissions. To limit global warming, it is essential to integrate these systems with carbon capture and storage. However, using alternative fuels raises challenges due to their complex compositions and their contents of heavy metals and other inorganic species. Chemical looping technologies have great potential for lowering costs for CO_2 capture and reducing emissions of pollutants, such as NO_x. These processes utilize metal oxides, or oxygen carriers (OCs), to transfer oxygen from air to fuel. However, the fates of the inorganic ash species in the presence of OCs are not well understood. The aim of this thesis is to provide a better understanding of the chemical transformations that occur in chemical looping applications, focusing on the heavy metals Zn, Cu, and Pb.

In this thesis, the reaction pathways of Zn, Cu and Pb are studied using combined theoretical and experimental approaches. Samples derived from combustion and gasification processes that utilize OCs are studied in detail by XRD, SEM-EDX and XPS. Zn and Cu are observed to interact with the OC and form ferrites under both combustion and gasification conditions. The formation of ferrites is shown to play an important role in the pathways for these elements. For the Fe-Ti-based OC ilmenite, Zn is incorporated into the ash layer while Cu is found to accumulate inside the ilmenite particles. The interaction between Zn and ilmenite is studied in greater detail in laboratory-scale experiments. It is observed that reaction with Zn is promoted after ilmenite has undergone consecutive reduction and oxidation cycles, owing to the formation of an Fe-rich layer on the external surface. Pb is concentrated in the fly ash regardless of the chemical looping technology and OC types investigated in this thesis.

The chemical speciation of Zn, Cu, and Pb in chemical looping processes is further considered with respect to the oxygen carrier type, temperature, reduction potential, and other ash components. The correlation of theoretical and experimental observations enables the identification of systems that were not well-described by thermodynamic equilibrium calculations (TECs). To improve the predictive potentials of TECs, thermodynamic databases are expanded by incorporating data i) available in the literature, and ii) from first principle calculations. For the latter, thermodynamic data is obtained for experimentally identified crystalline phases that are not available in the literature. This expansion has contributed to the updated and most comprehensive thermodynamic database for combined OC and ash systems. The database was implemented to study the phase stability during chemical looping combustion (CLC) of waste-derived fuels, providing the first insights into the chemical speciation of inorganic ash species. The results indicate that a major fraction of the problematic compounds exits the fuel reactor with the gas, preventing corrosion of the heat transfer surfaces in the air reactor.

Keywords: Waste-derived fuels, heavy metals, oxygen carriers, thermodynamic equilibrium calculations, chemical looping

List of Publications

This thesis is based on the following papers, which are referred to in the text according to their Roman numerals:

I. Staničić I, Andersson V, Hanning M, Mattisson T, Backman R, Leion H. *Combined manganese oxides as oxygen carriers for biomass combustion — Ash interactions.* Chemical Engineering Research and Design. (**2019**), 149, 104-120.

II. Staničić I, Hanning M, Deniz R, Mattisson T, Backman R, Leion H. *Interaction of oxygen carriers with common biomass ash components.* Fuel Processing Technology (**2020**), 200, 106313.

III. Staničić I, Mattisson T, Backman R, Cao Y, Rydén M. *Oxygen carrier aided combustion (OCAC) of two waste fuels - Experimental and theoretical study of the interaction between ilmenite and zinc, copper and lead.* Biomass and Bioenergy. (**2021**), 148, 106060.

IV. Staničić I, Cañete Vela I, Backman R, Maric J, Cao Y, Mattisson T. *Fate of lead, copper, zinc and antimony during chemical looping gasification of automotive shredder residue.* Fuel (**2021**), 302, 121147.

V. Staničić I, Backman R, Cao Y, Rydén M, Aronsson J, Mattisson T. *Fate of trace elements in Oxygen Carrier Aided Combustion (OCAC) of municipal solid waste.* Fuel (**2022**), 311, 122551.

VI. Staničić I, Brorsson J, Hellman A, Mattisson T, Backman R. *Thermodynamic Analysis on the Fate of Ash Elements in Chemical Looping Combustion of Solid Fuels Iron-Based Oxygen Carriers.* Energy & Fuels (**2022**) 36(17), 9648-9659.

VII. Brorsson J, Staničić I, Mattisson T, Hellman A. *Thermodynamic Properties for Metal Oxides from First-principles.* (**2023**) Submitted for publication.

VIII. Andersson V, Staničić I, Kong X, Leion H, Mattisson T, Pettersson J.B.C. *Alkali Desorption from Ilmenite Oxygen Carrier Particles used in Biomass Combustion.* (**2023**) Submitted for publication.

IX. Kong X,/Staničić I, Andersson V, Mattisson T, Pettersson J.B.C. *Phase Recognition in SEM-EDX Chemical Maps using Positive Matrix Factorization.* (**2023**) Submitted for publication.

X. Staničić I, Olsson E. O. L, Wu H, Glarborg P, Leion H, Mattisson T. *Investigating the Gas-solid Interaction between Ilmenite and Zinc for Chemical Looping.* Energy & Fuels (**2023**) DOI: 10.1021/acs.energyfuels.3c01052.

XI. Staničić I, Brorsson J, Hellman A, Rydén R, Mattisson T *Thermodynamic analysis on the fate of ash elements in chemical looping combustion of solid fuels─Manganese-based oxygen carriers.* (**2023**) Submitted for publication.

Contribution report

Ivana Staničić has contributed to the papers in the following ways:

I. Principal author with main responsibility for the characterization, analysis, thermodynamic calculations, writing, and parts of the experimental work.

II-V Principal author with main responsibility for the characterization, analysis, thermodynamic calculations, and writing.

VI. Principal author with main responsibility for the thermodynamic calculations, analysis, and writing.

VII. Supporting author with responsibility for implementing derived phases in thermodynamic databases, evaluation, discussion, and editing of the paper.

VIII. Supporting author with main responsibility for the part dealing with characterization, analysis, discussion, and editing of the paper.

IX. Shared first authorship with responsibility for the methodology, visualization, and writing.

X. Principal author with main responsibility for the experimental work (including characterization), analysis, thermodynamic calculations and writing.

XI. Principal author with main responsibility for the thermodynamic calculations, analysis, and writing.

Related peer-reviewed papers not included in this thesis

Purnomo V, Staničić I, Mei D, Soleimanisalim A H, Mattisson T, Rydén M, Leion, H. *Performance of iron sand as an oxygen carrier at high reduction degrees and its potential use for chemical looping gasification* Fuel (**2023**), 339, 127310

Related conference papers not included in this thesis

Staničić, I., Cañete Vela, I., Maric, J., Mattisson, T., Cao, Y., & Backman, R. *Fate of lead, copper, zinc and phosphorous in dual fluidized bed gasification of automobile shredder residue* Nordic Flame Days (**2019**).

Cañete Vela, I., Staničić, I., Maric, J., Mandviwala C., Seemann, M. *Ash-rich fuel gasification in fluidized bed, enhancing gas conversion by partial bed material recirculation* Nordic Flame Days (**2019**).

Staničić I., Backman R., Rydén M., Mattisson T. *Trace element behavior in fluidized bed applications utilizing oxygen carriers*. Proceedings of 24th International Conference on Fluidized Bed Conversion (**2022**).

Staničić, I., Brorsson, J., Rydén, M., Mattisson, T. *Thermodynamic analysis on the fate of ash elements in Chemical Looping Combustion of solid fuels using manganese oxide.* Proceedings of 6th International Conference on Chemical Looping (**2022**).

Acknowledgements

I would like to express my heartfelt gratitude to the following individuals who have played a pivotal role in shaping my Ph.D. journey:

First and foremost, I am deeply thankful to my supervisor, Tobias Mattisson, for the guidance, unwavering belief in my abilities, and constant encouragement. Your mentorship has not only pushed me to reach my full potential but has also been instrumental in shaping my research skills and intellectual growth.

I would also like to extend my profound appreciation to my supervisor, Magnus Rydén. Thank you for always making time for me, and for your assistance in structuring my thoughts. Your expertise and constructive feedback have been invaluable for my journey.

I extend my sincere appreciation to Rainer Backman for introducing me to the intricate world of thermodynamics and guiding me through its challenges. Your support has been greatly appreciated.

I have been incredibly lucky to have supportive and inspirational colleagues. Thank you, Henrik Leion for making it possible to conduct research around the world, and for your continuous support throughout this journey. Pavleta Knutsson, your inspiration and heartfelt support have meant a great deal to me. Marie Iwanow and Katarina Bergkvist, I am grateful for the dedication and the hours you have invested in helping me navigate unfamiliar territory. A special thanks to my chemical looping colleagues and friends; Nasrin, Joakim, Fredrik, Victor, Robin, Xiaoyun, Ivan, Jonatan, Daofeng, Mariane and Felicia for creating a supportive and stimulating research environment.

Sebastian, thank you for being the best office mate. I truly value our lengthy discussions on a wide range of topics, from palace cats to thermodynamics. You have the ability to turn any day into a positive one, and I am truly grateful for that.

Viktor, thank you for being an exceptional colleague and an incredible friend. It brings me immense joy that we have embarked on this journey together, supporting and uplifting one another. Our friendship has made the challenges more manageable, and the successes more meaningful.

I am grateful that I was provided the opportunity to conduct part of my Ph.D. at the Technical University of Denmark. I would like to thank the research group for their warm welcome, and I would like to express my sincere gratitude to Hao Wu, Peter Glarborg and Emil Lidman Olsson for their support throughout my exchange. Special thanks to Emil who was always there to help whenever I found myself struggling.

I would also like to extend my heartfelt appreciation to my friends and family for their support through the highs and lows of this journey. I am beyond fortunate to have you by my side.

Last but certainly not least, Amer, I am grateful for your unwavering support and continuous encouragement. I cherish you deeply and look forward to the many wonderful moments we will continue to share together.

I would like to acknowledge the fundings that have made this work possible. The initial three years of this research have received financial support from Formas, Swedish Research Council for Environment, Agricultural Sciences and Spatial Planning (Grant No. 2017-01095). The subsequent two years have been funded by the Swedish Research Council (Grant No. 2016-06023).

Gothenburg, May 2023

List of Abbreviations and Nomenclature

AR	Air Reactor
BA	Bottom Ash
BECCS	Bio-Energy with Carbon Capture and Storage
BT	Branches and Treetops
CCA	Copper Chromated Arsenate
CFB	Circulating Fluidized Bed
CLC	Chemical Looping Combustion
CLG	Chemical Looping Gasification
DFB	Dual Fluidized Bed
EDX	Energy Dispersive X-ray
FA	Fly Ash
FBC	Fluidized Bed Combustion
FR	Fuel Reactor
MSW	Municipal Solid Waste
OC	Oxygen Carrier
OCAC	Oxygen Carrier Aided Combustion
PMF	Positive Matrix Factorization
SEM	Scanning Electron Microscopy
TE	Trace Elements
TEC	Thermodynamic Equilibrium Calculation
WtE	Waste-to-Energy
XPS	X-ray Photoelectron Spectroscopy
XRD	X-Ray Diffraction
c_p	Heat capacity
G	Gibbs Free Energy
G_m^{Φ}	Molar Gibbs Free Energy of phase Φ
H_f°	Standard enthalpy of formation (1 bar and 298.15 K)
ΔH_t	Enthalpy change during phase transition
L_{ij}	Interaction parameter
$L(n, M)$	Lagrangian function
M_j	Lagrange multiplier
S_f°	Standard entropy of formation (1 bar and 298.15 K)
n_i^{Φ}	Molar quantity of phase constituent *i* in phase Φ
$a_{i,j}$	Stoichiometric coefficient
b_j	Molar quantity of system component *j*
μ_i	Chemical potential of species *i*

Table of Contents

1

INTRODUCTION

The concentrations of greenhouse gases in the atmosphere are increasing as a result of anthropogenic activities. The main reason for this increase is the extensive use of fossil fuels, whereby one-quarter of the total emissions originates from electricity and heat production. [1] As a result, the global mean temperature has increased. The warming linked to these anthropogenic emissions will persist for centuries to millennia and cause long-term changes in the climate system. [2] Significant reductions of greenhouse gas emissions will be necessary, in addition to large-scale removal of CO_2 from the atmosphere. [3-6] One way of reducing carbon emissions is to use Carbon Capture and Storage (CCS). However, to limit global warming reducing emissions will not in itself be sufficient to reach the climate goals, so it will become necessary to remove CO_2 from the atmosphere i.e., negative emissions. [7, 8] One important technology that enables the removal of CO_2 from the atmosphere is Bio-Energy with Carbon Capture and Storage (BECCS), and it is a key technology for meeting the climate goals. [9, 10] Since biomass is a limited resource, it is also important to consider bio-based streams that are readily available and do not compete directly with other important uses of biomass. Here, municipal, industrial, agricultural and forest residues could be possibilities. The focus of this work is on the former two residue types, and a brief overview of these fractions is given in Section 3.3.

The largest contributor to anthropogenic climate change is CO_2, and the second largest is methane. [11, 12] One of the major anthropogenic sources of methane emissions is waste landfills. [13] Globally, municipal solid waste (MSW) has been managed mainly by landfilling in open dump sites, followed by recycling and thermal treatment. [14] However, since the beginning of the 21st Century, disposal of waste in landfills has been reduced by more than half in the European Union (EU) as a result of the Waste Framework Directive (2008/98/EC) and Landfill Directive (Council Directive 1999/31/EC) while incineration with energy recovery has increased fourfold. [15] The Waste Framework Directive encapsulates the main concepts related to waste management. The waste hierarchy, presented in Figure 1, defines an order of priority for different management options going from the most-preferred option, which is prevention, to the least-desired option, disposal.

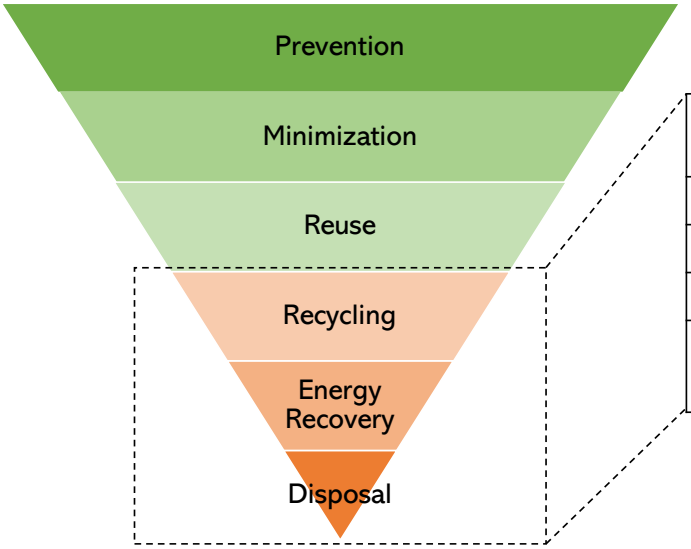

Treated MSW (2021)	Sweden	EU27
Recycling – Material	19.9	29.9
Recycling – Organic	19.5	19.2
Energy recovery	59.7	26.5
Disposal Landfilling and incineration without energy recovery	<1	23.1

Figure 1. The waste management hierarchy along with the different treatment processes for municipal solid waste (MSW). The values for treated waste in Sweden and the EU-27 (2021) are given in wt.% [15].

When prevention, minimization, reuse, and recycling are not feasible options, energy recovery is preferred over disposal. [16] With increasing population and economic growth rates [17, 18], the energy demand will increase and will require a steady supply of affordable renewable energy with minimal environmental impacts. In line with this development, the global Waste-to-Energy (WtE) technology markets can be expected to increase dramatically. About 40 % of the generated MSW worldwide is currently disposed of in some type of landfill. [19] The corresponding value in Sweden is less than 1%. [15] The reason for this is partially attributable to high recycling rates, but also to the use of waste to generate heat and electricity (Figure 1). Annually, Sweden recovers heat and electricity from 6 million tonnes of waste, with high fractions of bio-based materials such as wood and paper. [20] Combining WtE facilities with CCS opens up the possibility to use the streams to achieve negative emissions. [7, 8]

Sweden has more than 150 units that produce electricity and supply heat for district heating. About 70 of these units utilize fluidized beds and 15 of them burn waste fuels as their main feedstock. Fluidized bed boilers use small particles, referred to as 'bed material'. One common type of bed material is silica sand. However, it has been shown that replacing the bed material in fluidized beds with metal oxides, so-called Oxygen Carriers (OCs), confers certain advantages in terms of evening out the temperature and oxygen distributions in the boiler, as well as reducing the risk of agglomeration, and has positive effects on emissions. [21] In addition, lower levels of excess air may be needed during the combustion process, which would have advantages for post-combustion CO_2 capture. [21] Nine fluidized bed boilers with outputs in the range of 12-170 MW_{th} have been operated with OCs.

2

AIM AND SCOPE

The overall aim of this thesis is to increase understanding of the behaviors of inorganic ash compounds in applications where OCs are utilized. This goal is achieved using a wide range of experimental and modeling approaches. The inorganic species in focus of this thesis are the heavy metals Cu, Pb and Zn. Nonetheless, as the ash chemistries of these elements are interconnected with those of other ash species, for example sodium, potassium and calcium, the reaction paths of these elements will be discussed also. At the start of this project, there were no published studies on the behaviors and interactions of heavy metals and OCs. As these inorganic species are highly relevant with respect to ash characteristics, corrosion, and agglomeration, it is essential to study the fates of such species. The research questions in focus in this thesis are as follows:

1) How are inorganic species affected by the presence of OCs?
2) In what forms are inorganic species bound in OC particles?
3) How does the high reduction potential in the fuel reactor of CLC and CLG affect metal speciation?
4) Can multicomponent, multiphase equilibrium calculations predict the fates of inorganic species, and what measures can be taken to improve the predictive potential of this approach?

To answer these questions, experiments involving ash components and OCs have been carried out in a range of reactors, in addition to sampling in commercial units. These samples have been characterized using various tools, such as x-ray diffraction, scanning electron microscopy, and x-ray photoelectron spectroscopy, and the results have been compared with multicomponent, multiphase equilibrium calculations. With this approach, a rigorous and comprehensive view picture of the chemistry and pathways for important inorganic species is obtained.

This thesis includes the research described in the 11 appended papers, and all details of the work are described in these papers and associated *Supporting Information*. The thesis itself presents the key findings in two parts. Section 7, *Results and Discussion - Part I* summarizes the experimental observations and the correlations with thermodynamic predictions concerning the heavy metals Cu, Pb and Zn. The influences of the reduction potential, temperature, and other inorganic ash species on volatility and phase stability are presented. Section 8, R*esults and Discussion - Part II* deals with the implementation and improvement of the multicomponent, multiphase equilibrium calculations. The relationships between the appended papers and the results are elaborated upon below.

Part I. The chemical speciation of heavy metals on the OC surface and core is investigated in detail in **Papers III–V**. In **Paper V**, a series of samples is characterized with respect to the particle surface and cross-section, to elucidate the evolution of ash layer buildup over time. Furthermore, parameters such as temperature, reduction potential, and different fuels are studied in terms of thermodynamics for their influences on trace element partitioning. The interactions between ilmenite and gaseous Zn species are studied in detail in laboratory-scale experiments in **Paper X**, towards the goal of obtaining a more detailed understanding of the reaction for this important element. A method to analyze chemical maps is developed in **Paper IX** to distinguish between the interactions with ilmenite particles and other impurities in the sample, and to distinguish between possible phases within the ilmenite particles. This method is applied in **Paper VIII** to study the distribution of alkali metals in ilmenite derived from an industrial OCAC process using RWW. The partitioning of alkali and trace metals in CLC of waste-derived and biomass fuels is further studied using a thermodynamic approach for Fe-based OCs (**Paper VI**) and Mn-based OCs (**Paper XI**).

Part II. This section presents the advances made in this work concerning the use and generation of thermodynamic data. In **Papers III–V**, thermodynamic data for the trace elements are evaluated, and the databases are expanded using data from the literature. Thermodynamic databases are also assessed based on the results obtained from laboratory-scale experiments in **Papers I** and **II**, in which the interactions between Fe- and Mn-based OCs and the major ash components Ca, K, P, and Si are studied. However, as there are no data available in the literature for several relevant phases, a method is developed in **Paper VII** to calculate the relevant thermodynamic properties from first principles. The databases are, thereafter, expanded with the identified compounds in **Papers I** and **II** using the method presented in **Paper VII**. The extended databases are used to study the phase distributions in CLC processes of Fe-based and Mn-based OCs in **Papers VI** and **XI**, respectively.

A summary of the appended papers and their content is presented in Figure 2.

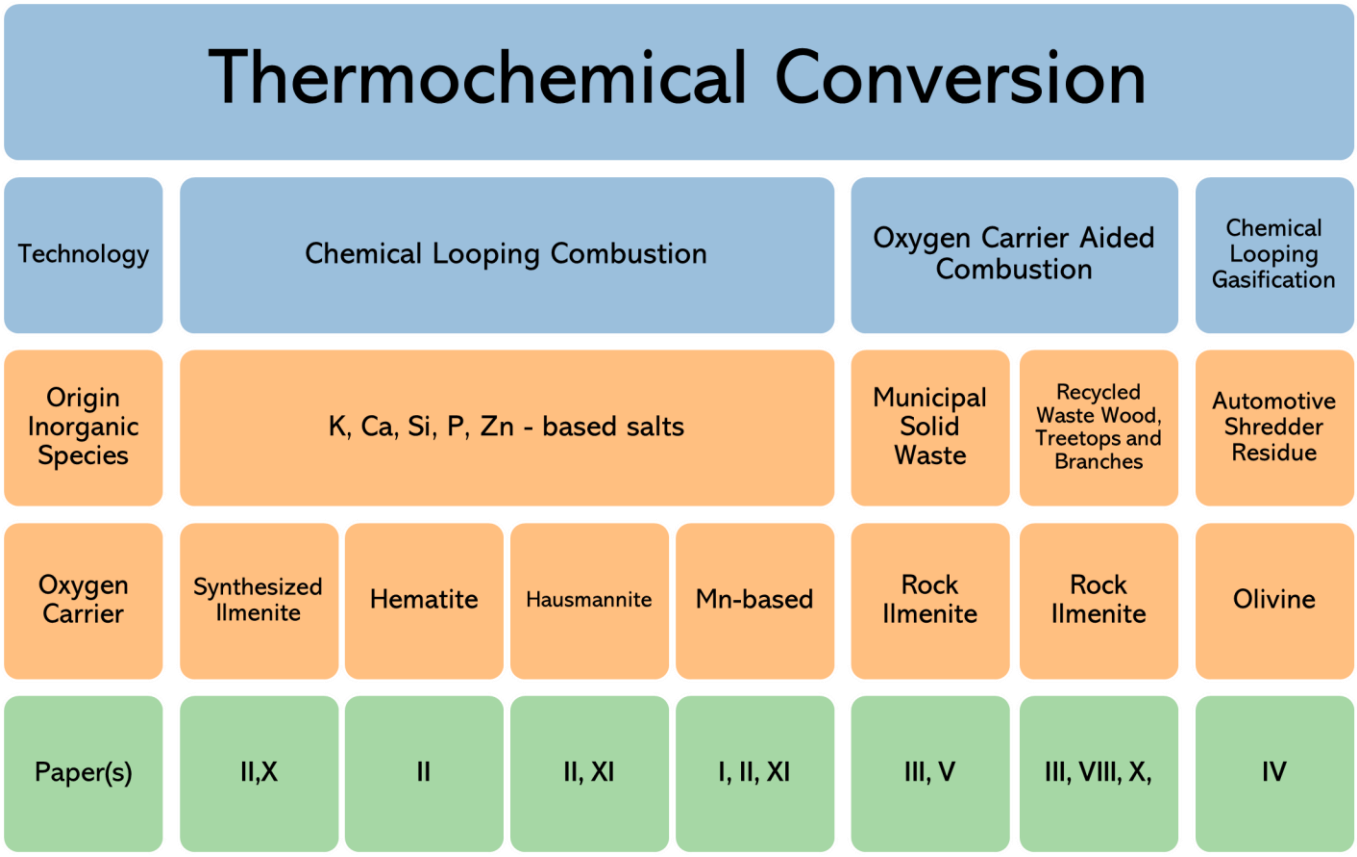

Figure 2. Summary of the technologies, origin of the inorganic species and oxygen carriers investigated in this thesis and the appended papers.

3

BACKGROUND

3.1 Chemical Looping Technologies

The flexibility, efficiency, and stability characteristics of circulating fluidized bed (CFB) boilers, as well as their ability to handle a wide range of fuels for co-combustion, make them highly suitable for the thermochemical conversion of waste-derived fuels. [22] Oxygen Carriers (OCs) can be used in single or dual fluidized beds for the thermochemical processing of waste-derived fuels, as illustrated in Figure 2. The following sections provide an overview of the reactions that occur in each process.

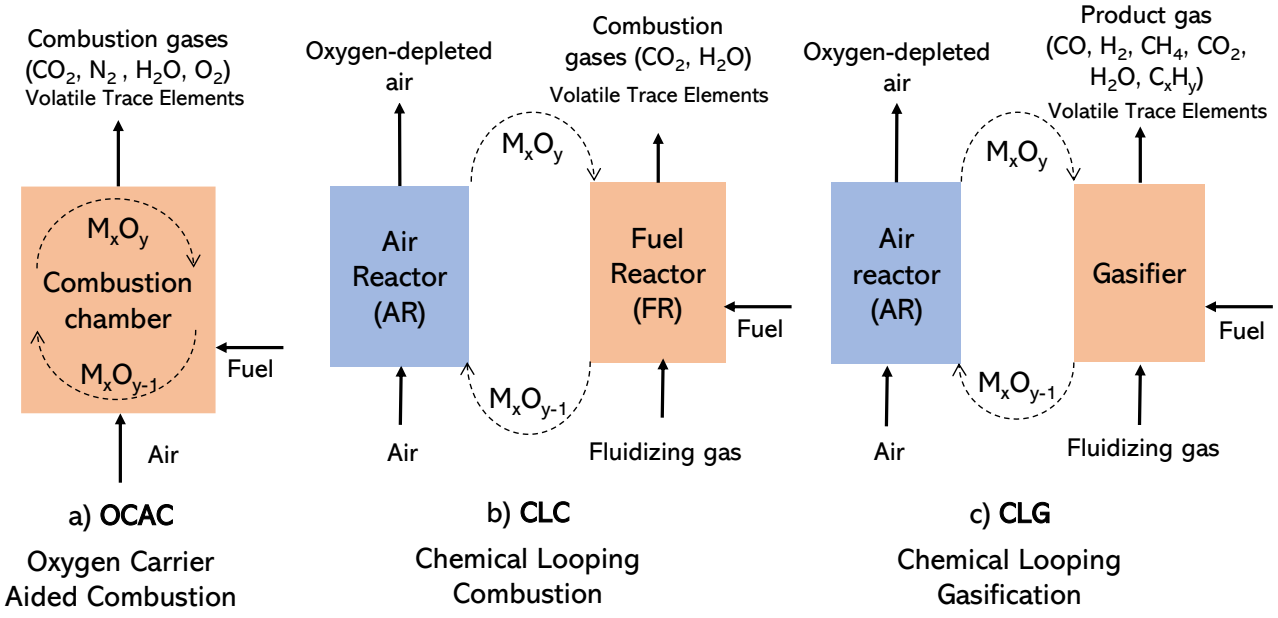

Figure 3. Schematic of three processes that utilize metal oxides (M_xO_y) as oxygen carriers: a) Chemical Looping Combustion (CLC); b) Chemical Looping Gasification (CLG); and c) Oxygen Carrier Aided Combustion (OCAC).

An important advantage of OCs is that they can replace the conventional bed material in existing CFB boilers. In recent years, OCs have been evaluated in several WtE facilities in Sweden. This technology is called Oxygen Carrier Aided Combustion (OCAC) [23-25] (Figure 3a). Although OCAC has been successfully demonstrated at industrial scale, [23, 25] research into this technology is still relatively limited. [24, 25] During OCAC, the OCs are reduced in

the fuel-rich parts and oxidized in the oxygen-rich parts, according to reactions (1) and (2), generating even oxygen availability and temperature in the boiler

$$(2n+m)\ M_xO_y + C_nH_{2m} \rightarrow (2n+m)\ M_xO_{y-1} + m\ H_2O + n\ CO_2 \quad (1)$$

$$M_xO_{y-1} + \frac{1}{2}O_2 \rightarrow M_xO_y \quad (2)$$

The knowledge gained from OCAC operation provides insights into ash interactions with OCs and the expected behavior during Chemical Looping Combustion (CLC). CLC involves two interconnected fluidized bed reactors, the Air Reactor (AR) and the Fuel Reactor (FR), as shown in Figure 3b. In the FR, the fuel is converted to CO_2 and H_2O in a nitrogen-free environment. After condensation of H_2O, a highly concentrated stream of CO_2, suitable for CCS, can be obtained. Implementing CCS in CLC is advantageous, as all the converted carbon is obtained in the concentrated stream from the FR. Here, the OCs transport heat and oxygen between the two reactors. Initially, the OC is reduced by the fuel in the FR according to reaction (1). The OC is then transported to the AR, which is fluidized with air. The air oxidizes the OCs according to reaction (2) before they are returned to the FR and the cycle is repeated. CLC is an attractive option because the cost and energy penalty associated with CO_2 capture are amongst the lowest compared to other technologies. [26] Furthermore, the use of biomass in CLC has gained interest as an option for BECCS. [26-28]

Another technology that utilizes two interconnected fluidized beds is Dual Fluidized Bed (DFB) gasification. [29] This process is based on converting fuel to a valuable gas. DFB gasification entails a boiler and a gasifier, which are connected by loop seals. The bed material, which is usually silica sand or olivine sand, is circulated between the two reactors. The bed is heated in the boiler and, thereafter, transported to the gasifier. In the gasifier, the fuel is first devolatilized, and the remaining char undergoes gasification forming CO and H_2 according to the reactions (3) and (4). The ratio between the two is further controlled by the water-gas shift reaction (5).

$$C + H_2O \rightarrow CO + H_2 \quad (3)$$

$$C + CO_2 \rightarrow 2\ CO \quad (4)$$

$$CO + H_2O \leftrightarrow CO_2 + H_2 \quad (5)$$

Replacing the bed material in a DFB setup with OCs will create a Chemical Looping Gasification (CLG) process, as illustrated in Figure 3c. [30] In the gasifier, here also referred to as the FR, the OCs will react the gasification products according to reactions (1) and (6-7). The OCs are circulated back to the AR and re-oxidized according to reaction (2), before the process is repeated. The outlet from the FR contains large amounts of not completely oxidized products (CO, H_2 and CH_4 for example), which can be further utilized for production of chemicals or fuels. One advantage of using OCs is that the combustion heat is "replaced" by the heat of oxidation in the AR, i.e., no fuel combustion is necessary for the AR.

$$M_xO_y + nH_2 \rightarrow M_xO_{y-1} + nH_2O \quad (6)$$

$$M_xO_y + nCO \rightarrow M_xO_{y-1} + nCO_2 \quad (7)$$

3.1.1 Chemical Looping with Oxygen Uncoupling

The conversion of solid fuels is complex and involves several steps and many possible reactions. First, the fuel is heated, the moisture content is evaporated, and then the fuel undergoes devolatilization. The remaining char, mainly C, is gasified by the fluidizing steam or CO_2 according to reactions (3) and (4). The volatile species and products from the gasification are oxidized by the OC. However, char gasification with steam as an oxidizing agent is rather slow relative to the other combustion reactions, so it becomes the rate-limiting step for fuel conversion. [31] To achieve complete conversion of the fuel, the char requires a long residence time in the bed. However, there is a way to circumvent the slow gasification step. Certain OCs can release gaseous oxygen at relevant conversion temperatures, according to reaction (8). The char can then react directly with gaseous oxygen, such that the slow gasification step is bypassed.

$$M_xO_y \rightarrow M_xO_{y-1} + \frac{1}{2}O_2 \tag{8}$$

This reaction scheme referred to as Chemical Looping with Oxygen Uncoupling (CLOU). [32] CLOU avoids the gas-solid reaction between OCs and volatiles, which requires direct contact. Instead, gaseous oxygen can react directly with the volatiles and facilitate complete conversion, despite inadequate mixing of the OC and fuel.

3.2 Oxygen Carrier Selection

The utilization of OCs can affect the boiler chemistry and, thereby, the fates of inorganic species. The outcome will depend on the ash content of the fuel, the specific mineralogy, experimental conditions, and OC composition. [33] Many studies have been conducted on different types of OCs, mineral ores and byproducts from industries, and on synthetic materials with varying support materials and preparation methods. It is important to understand the interactions between OCs and inorganic species as they can lead to deactivation, agglomeration, and attrition of the OC. One major problem in fluidized bed reactors is the agglomeration of bed particles, which in the worst-case scenario can cause defluidization. These agglomerates are usually caused by alkali reactions with silica, leading to the formation of sticky alkali silicates with low melting temperatures. [34, 35] Moreover, ash components at the surface or in the bulk of the OC may alter the reaction kinetics. For example, the reaction rate can be decreased if gas diffusion is hindered by an ash layer that is formed on the surfaces of the particles, although the presence of ash components on OCs can also have a catalytic effect. In addition to affecting the conversion process itself, the OCs can exert a significant effect on the pathways and fates of the ash elements, which could have environmental implications, as well as raising the possibility to recycle valuable elements. The focus of this thesis will be on two types of OCs: iron (Fe)-based OCs, due to their implementation at the industrial level; and manganese (Mn)-based OCs, owing to their promising CLOU properties.

3.2.1 Iron-based Oxygen Carriers

Iron-based OCs are both environmentally friendly and economically viable due to their abundance. [36] Fe-based OCs have high melting temperatures, which reduces the risk of agglomeration. [37] However, they suffer from the disadvantage that they exhibit a comparably low oxygen transport capacity. [38] Despite this, various Fe ores have shown favorable attributes as OCs when operated in CLC pilot-scale units. [39, 40] One example is ilmenite concentrate, hence referred to as ‘ilmenite’ or ‘rock ilmenite’, which is obtained after crushing and processing the Fe and Ti rich mineral ore. Ilmenite has been extensively examined as an

OC [23, 25, 41-44] due to its good fluidization properties, high melting point, good mechanical integrity, and because it can be utilized without much pretreatment. Thus, ilmenite has been used as an OC in several commercial WtE units in Sweden that have demonstrated OCAC. [25]

Several studies have been conducted with the focus on the interactions between Fe-based OCs and major ash-forming elements. [45-47] For example, subjected to consecutive oxidation and reduction cycles, the ilmenite particles undergo structural changes, such as the formation of cracks and increased porosity [48], together with segregation of Fe to the particle surface and enrichment of Ti in the particle core [41, 46-48]. This process is referred to as *activation*. During operation with solid fuels, a calcium-rich double layer with Fe in-between has been observed. [41, 47] With a longer exposure time, potassium migrates into the ilmenite particle core. [47] However, depending on the chemical association of potassium when interacting with ilmenite it can lead to different outcomes. [49] For example, in the presence of steam, the salts K_2CO_3, K_2SO_4, and KCl react to form KOH (g). The formation of gaseous KOH enhances the interaction with ilmenite and results in the production of potassium-titanates. [49] Research has also been conducted on the ash layer build-up and interaction with sulfur when utilizing ilmenite in OCAC. [45-47] These studies have shown that during oxidation sulfur uptake occurs in the form of calcium and potassium sulfates, while SO_2 is released during reduction.

3.2.2 Manganese-based Oxygen Carriers

Manganese oxides are an attractive option as OCs for CLOU. However, they release gaseous oxygen mainly at low temperatures and the kinetics of re-oxidation is slow. This problem can be circumvented by combining Mn with other metals, such as Fe, silicon, calcium, nickel, magnesium, and Cu. [50] The thermodynamic properties of combined oxides such as Mn–Fe, Mn–Si, and Mn–Fe–Si have all shown promise. [51-56] Perovskite materials have attracted interest for both CLC and CLOU. [57-59] Perovskites have the general formula $ABO_{3-\delta}$, where A and B represent different cations. The oxygen deficiency (δ) of perovskites can be altered by changing the temperature, pressure, and/or oxygen partial pressure. As the conditions are different in the AR and FR, the perovskite will be oxidized in the AR and will release O_2 in the FR. The main focus has been on the single perovskite $CaMnO_{3-\delta}$. [60, 61] Despite the vast number of publications on CLOU materials [58, 62-70] and the performances of different Mn-based OCs [52, 62, 64, 70-72], data on the ash-induced crystalline phases in Mn-based systems are scarce. With the exception of one conference contribution [73], before the start of this work there were no published studies on improving our understanding of the interactions between Mn-based OCs and ash.

3.3 Inorganic Species in Waste-Derived Fuels

During fluidized bed combustion, two types of ashes are generated: the bottom ash (BA), and the fly ash (FA). These ashes contain high levels of metals, salts, and other components. These constituents may be toxic, although in some cases they may also have economic value. The ash composition is highly dependent upon the fuel type and can be problematic for waste-derived fuels due to high concentrations of alkali metals (K and Na) and heavy metals (Zn, Cu, and Pb). The ash compositions of wood fuels (chips, pellets), MSW, Recycled Waste Wood (RWW), and Automotive Shredder Residue (ASR) are presented in Table 1, which lists the minimum and maximum concentrations of important inorganic species in the ashes. The term ‘trace elements’ refers to elements that are present at concentrations <0.1 wt.%, and may include elements from a large span of the periodic table. These elements occur naturally in the ecosystem and their concentrations vary significantly, in part due to anthropogenic sources. A subclass of the trace elements is the heavy metals, which include Cd, Pb, Hg, Zn, and Cu. In

waste-derived fuels, these elements can be present in amounts that mean that are minor (0.1–1.0 wt.%). In this thesis, the term ‘trace elements’ and ‘heavy metals’ will be used interchangeably.

Table 1. Compositions of common inorganic species present in waste and biomass fuels of interest for this thesis. Minimum and maximum values are reported as wt.% dry for Ca, Si, Al, Fe, Na and K, and as mg/kg dry for Cr, Cu, Sb, Ni, Pb and Zn. [74-76]

		Wood fuels		Recovered Waste Wood		Municipal Solid Waste		Automotive Shredder Residue	
Paper(s)		**III–VI**, **VIII**, **XI**		**III**, **VI**, **VIII**, **X**, **XI**		**III**, **V, VI**		**IV**	
		Min	Max	Min	Max	Min	Max	Min	Max
Ca	wt.% dry	9.9	26.2	4.5	12.4	11.9	16.5	6.3	6.7
Si		5.7	23.5	5.4	17.2	15.5	20.2	13	14
Al		0.4	4.2	0.8	3.3	4.2	10.9	4.5	5.1
Fe		0.9	2.5	0.9	6.0	2.3	3.7	22	23
Na		0.3	0.7	0.6	1.9	2.6	3.3	1.6	1.6
K		6.7	9.0	1.0	2.6	1.4	1.7	0.9	0.9
Cr	mg/kg dry	40	118	81	3,191	400	1,340	1,300	4,000
Cu		68	165	75	1,912	1,200	9,600	11,700	17,400
Sb		-	-	2.5	53	-	-	-	-
Ni		12	147	14	106	100	470	840	2,000
Pb		-	-	140	28,611	640	9,300	1,800	2,300
Zn		1,867	3,130	2,420	184,167	2,700	6,000	43,000	46,900

Waste-derived fuels are inhomogeneous and can contain several individual waste fractions. A summary of their constituents is presented here, then the various applications in which heavy metals are utilized are highlighted. MSW consists of a wide range of components including food waste, paper, plastics, wood, textiles, rubbers, leathers, cardboards, yard waste, shoes and batteries. RWW is comprised of different wood fractions originating from construction, demolition and refurbishment work. ASR originate from end-of-life vehicles and consists of glass, fibers, rubbers, foams, wood, metals, and various plastics.

Zinc is used in numerous applications across various industries. Zn can be found in glass, cement, paints, pigments, foods, electronics, batteries and flame retardants. It is used for surface treatment, wood impregnation, additives in plastics and galvanization processes. Additionally, it is used in automotive applications, such as casting, coating, door handles and locks. Copper is widely used in wiring and electrical components. Another example is Copper Chromated Arsenate (CCA) which has been used as a wood preservative. In 2004, the EU introduced regulatory restrictions on CCA, resulting in a reduction of CCA-treated wood. [77] However, substantial quantities have been used daily and for a long time, and there are currently no EU directives stating that CCA-treated wood should be removed from their current applications. [78] Pb is frequently encountered in electronics, batteries and pigments. While Pb-based compounds were historically used as additives in for example PVC, their usage is now restricted due to regulatory measures. The primary source of Pb (and Zn) in RWW is due to the presence in surface-treated wood. [78]

3.4 Release of Inorganic Species

The chemistry of heavy metals in the presence of OCs is an unexplored field, although there is extensive knowledge regarding the chemistry during coal gasification and combustion. [79-82] Recently, a review on trace element behaviors in coal combustion and gasification highlighted the need for further understanding, particularly in fluidized bed systems. [79]

The complex behaviors of the trace elements may be linked to the intrinsic volatility of the species. For example, the transport of heavy metals during combustion can be described by the so-called *volatilization condensation theory*, which has been used to predict the locations of elements in fly ash particles based on boiling points. [83, 84] Elements with boiling points higher than the typical combustion temperature are part of the matrix's core, while elements that evaporate during combustion are incorporated into or deposited onto the fly ash particle surface. Based on the volatility of inorganic elements, they can be classified into different groups. [85] Figure 4 shows the classification and volatilities of the different inorganic species in coal combustion and gasification. The species that are relevant for this thesis are marked in red. The elements in Class III are highly volatile and commonly emitted to the gas phase. The elements in Class II are expected to evaporate and subsequently condense downstream of the combustion chamber. This condensation leads to an enrichment in smaller ash particles or aerosols. Class II elements are enriched in the FA and depleted in the BA. Class I elements have low volatility and are enriched in the BA relative to the FA.

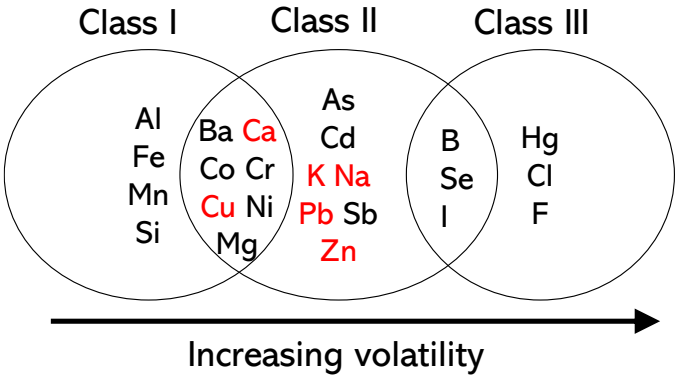

Figure 4. Classification of inorganic species in coal combustion and gasification of based on volatility. Adapted from [85].

For biomass and waste-derived fuels the situation is different since the volatilization behaviors of trace elements are not just linked to intrinsic volatility, but also to the availability of other inorganic species. For example, K may form both volatile compounds, such as KCl, and non-volatile compounds, such as K-silicates. Meaning that it could be a part of both Class I and II. However, there are also competing balances between the inorganic species since the affinity of Cl towards alkalis for example, is higher compared to other metals (H > K/Na > Pb > other heavy metals). Consequently, the availability of Cl to the heavy metals is governed by the presence of alkali metals. [86]

When metal chlorides form, they follow the flue gas into the convection path of the boiler, where they can cause corrosion and fouling. [87] It has been reported that heavy metal chlorides can induce corrosion at temperatures as low as 250°–300°C [88], and the formation and behaviors of such heavy metal chlorides are not yet as deeply understood as those of alkali metals. This is particularly problematic in thermal treatment of waste-derived fuels. [89] The increased mobility of metal chlorides can also promote reactions with the bed material. [34] Thus, the alkali and heavy metal balance in the boiler can also be affected by the interaction

with the bed material. If the chosen bed material does not interact and capture metals, it may reduce the risk of agglomeration. [90] However, it could lead to increased concentrations of metal chlorides in the gas phase, increasing the likelihood of deposition of alkali and heavy metal components downstream of the heat transfer surfaces.

As shown in Figure 4**,** heavy elements (Pb, Zn, Cd, Sb, and Ni) are expected to be concentrated in the FA, which makes this ash fraction ecologically harmful. High concentrations of heavy metals in ashes increase their toxicity levels and, as a consequence, the handling costs, preventing their use as fertilizers in soils and forests. [91] For these reasons, the FA has been in focus for metal extraction, especially with respect to the removal of Zn, Cu, and Pb. [92-95] In systems that utilize OCs, a complex chemistry can be expected with the chemical transformation of metals in the gas phase and the interactions between the gas phase, ash components [80], and OCs. There are many possible reaction paths when one element is released from the fuel before it reaches and interacts with the OC. The underlying chemistry will most likely depend upon the volatility, composition of the surrounding gas phase, and solid surface activity. [96]

3.5 Role of Thermodynamics

Thermodynamic Equilibrium Calculations (TECs) have been applied widely to understand and predict ash-related problems [97-99] and the chemistries of combustion and gasification processes. [100-104] TECs are based on minimizing the Gibbs free energy, which calculates the chemical equilibrium composition of a system considering the thermodynamic data for all possible phases and compounds.

Thermodynamic databases can vary considerably in terms of both quality and content. Available thermodynamic databases include JANAF [105], IVTANTHERMO [106], SGTE [107], MTDATA [108], Thermo-Calc [109], HSC Chemistry [110], and FACT [111]. Previous studies have evaluated, compared and optimized the available data. For example, Talonen (2008) evaluated the data for 14 heavy metals (As, Cd, Co, Cr, Cu, Hg, Mn, Ni, Pb, Sb, Tl, V, Mo, and Zn) under both oxidizing and reducing conditions. [112] The differences between the databases were evident, in that HSC included 700 heavy metal species (the highest number), whereas FACT had 423 and JANAF only 150 metal species. Subsequently, data for Cd, Cr, Cu, As, and Pb were reviewed and compared for the SGTE, FACT and HSC databases by Lundholm et al. [113] The number of compounds and the thermodynamic data varied significantly across the databases, and the variability was lower for condensed phases and higher for gaseous species. Recent research has focused more on waste-derived fuels, and a comprehensive review of the available databases and models for waste and biomass combustion processes has been presented by Lindberg et al. [114] The authors concluded that there was no available thermodynamic database for the complete system (Na^+, K^+, Ca^{2+}, Mg^{2+}, Zn^{2+}, Pb^{2+})/(CO_3^{2-}, SO_4^{2-}, S^{2-}, O^{2-}, Cl^-). However, the NaCl–KCl–$CaCl_2$–$MgCl_2$–$ZnCl_2$–$PbCl_2$ subsystem is available in the FTsalt database in the FactSage software, where the thermodynamic properties of the $ZnCl_2$ and $PbCl_2$ systems have been evaluated. The most comprehensive thermodynamic database is the FToxid database in FactSage for solid/liquid silicates and oxides of Al_2O_3, As_2O_3, B_2O_3, CaO, CoO, CrO, Cr_2O_3, Cu_2O, FeO, Fe_2O_3, GeO_2, K_2O, MgO, MnO, Na_2O, NiO, PbO, SiO_2, SnO, TiO_2, Ti_2O_3, ZnO and ZrO_2.The introduction of $KAlO_2$/$NaAlO_2$ in the slag phase has improved the accuracy of the liquid properties. [111]

Several studies investigated the fates of trace elements during coal combustion and gasification using thermodynamic calculations. Many groups have used the FactSage software to study ash interactions and trace element partitioning. [97, 102, 115] Frandsen et al. [100] investigated the fates of several trace elements during the combustion and gasification of coal using the

GFEDBASE database [116]. Trace element behavior in fluidized beds have been studied by Konttinen et al. [104] and Kramb et al. [117]. Becidan et al. [103] have studied separate waste fractions of MSW and their influences on the behaviors of alkali metals and trace elements during combustion. Enestam et al. [118] have evaluated the condensation behaviors of Pb and Zn in the bubbling fluidized bed combustion of RWW.

4

MATERIALS AND METHODS

A summary of the investigated OCs, both their oxidized and reduced forms, and the inorganic compounds and species investigated, the scale from which the samples were derived, and the relevant publication are presented in Table 2. The Fe-based (**Papers II** and **X**) and Mn-based OCs (**Papers I** and **II**) were studied at a laboratory scale. Solid samples have also been obtained from two industrial OCAC plants (**Papers III**, **V**, and **VIII**) and one semi-commercial DFB gasifier (**Paper IV**)

Table 2. List of investigated oxygen carriers, inorganic species, the scales studied, and the relevant publications. Possible oxygen transfer reactions for oxygen carriers under chemical looping conditions are presented for each OC. The reactions are based on thermodynamic data, and the observed crystalline phases. M, metal.

Oxygen Carrier	Provider	Possible Oxygen Transfer Reaction	Investigated Inorganic Compounds and Species	Scale	Paper
"MnFe"	VITO	$6\ M_2O_3 \rightarrow 4\ M_3O_4 + O_2$	$CaCO_{3\ (s)}$ $K_2CO_{3\ (s)}$ $CaHPO_{4\ (s)}$	Laboratory	**I**
"MnFeAl"	VITO				**I**
"MnSi"	VITO	$\frac{2}{3}\ Mn_7SiO_{12} + 4\ SiO_2 \rightarrow \frac{14}{3}\ MnSiO_3 + O_2$			**I**
		$2\ M_3O_4 + 6\ MnSiO_3 \rightarrow 6\ Mn_2SiO_4 + O_2$			
		$\frac{3}{2}Mn_7SiO_{12} + \frac{10}{3}MnSiO_3 \rightarrow 4\ Mn_2SiO_4 + O_2$			
"MnSiTi"	VITO	$\frac{2}{3}\ Mn_7SiO_{12} + \frac{14}{3}\ TiO_2 \rightarrow \frac{14}{3}\ MnTiO_3 + \frac{2}{3}\ SiO_2 + O_2$			**I**
		$\frac{2}{3}\ Mn_7SiO_{12} + 4\ SiO_2 \rightarrow \frac{14}{3}\ MnSiO_3 + O_2$			
		$\frac{3}{2}Mn_7SiO_{12} + \frac{10}{3}MnSiO_3 \rightarrow 4\ Mn_2SiO_4 + O_2$			
Hausmannite	Elkem AS via SINTEF	$2\ Mn_3O_4 \rightarrow 6\ MnO + O_2 > 850°C$ $6\ Mn_2O_3 \rightarrow 4\ Mn_3O_4 + O_2 < 850°C$	$CaCO_{3\ (s)}$ $K_2CO_{3\ (s)}$ $SiO_{2\ (s)}$ $CaCO_3 + SiO_2$ $K_2CO_3 + SiO_2$		**II**
Hematite	Höganäs	$6\ Fe_2O_3 \rightarrow 4\ Fe_3O_4 + O_2$			**II**
Synthesized ilmenite	VITO	$2\ Fe_2O_3{\cdot}TiO_2 + 2\ TiO_2 \rightarrow 4\ FeO{\cdot}TiO_2 + O_2$ $2\ Fe_2O_3{\cdot}TiO_2 + 2\ TiO_2 \rightarrow 4\ Fe_3O_4 + 12\ TiO_2 + O_2$ $2\ Fe_3O_4 + 6\ TiO_2 \rightarrow 6\ FeTiO_3 + O_2$			**II**
	CSIC		$Zn_{\ (g)}$ $ZnCl_{2\ (g)}$		**X**
Ilmenite	Titania A/S		$Zn_{\ (g)}$ $ZnCl_{2\ (g)}$		**X**
			Zn, Cu, Pb (MSW)	Industrial	**III, V**
			Zn, Cu, Pb (RWW)	Industrial	**III, VIII, X**
Olivine	Sibelco Nordic	$(Mg_x, Fe_{1-x})_2SiO_4 + (1-x)\ Fe_2O_3 + (1-x)\ SiO_2 \rightarrow (Mg,Fe_{1-x})_2SiO_4 + (1-x)\ O_2$	Zn, Cu, Pb, Sb (ASR)	Semi-industrial	**IV**

4.1 Analytical Methods

Characterization of solid ash samples was performed in a stepwise fashion using a range of techniques. The total concentration of metal was first obtained, albeit without any information on the chemical state of the metal in question. Thereafter, the crystalline phases were determined, with no knowledge regarding the distribution of the phases within the sample or particle. Thus, the morphologies and chemical distributions of sample surfaces and cross-sections were investigated with scanning electron microscopy (SEM). Lastly, the samples were investigated using XPS, which detects low-concentration elements and their chemical states. Taken together, these techniques provide a good overview of the compositions of the solid samples. These results can be further utilized or compared with thermodynamic equilibrium calculations the TECs. The approach for studying inorganic species in the solid samples is presented in Figure 5, and the specific techniques in question are presented in more detail below.

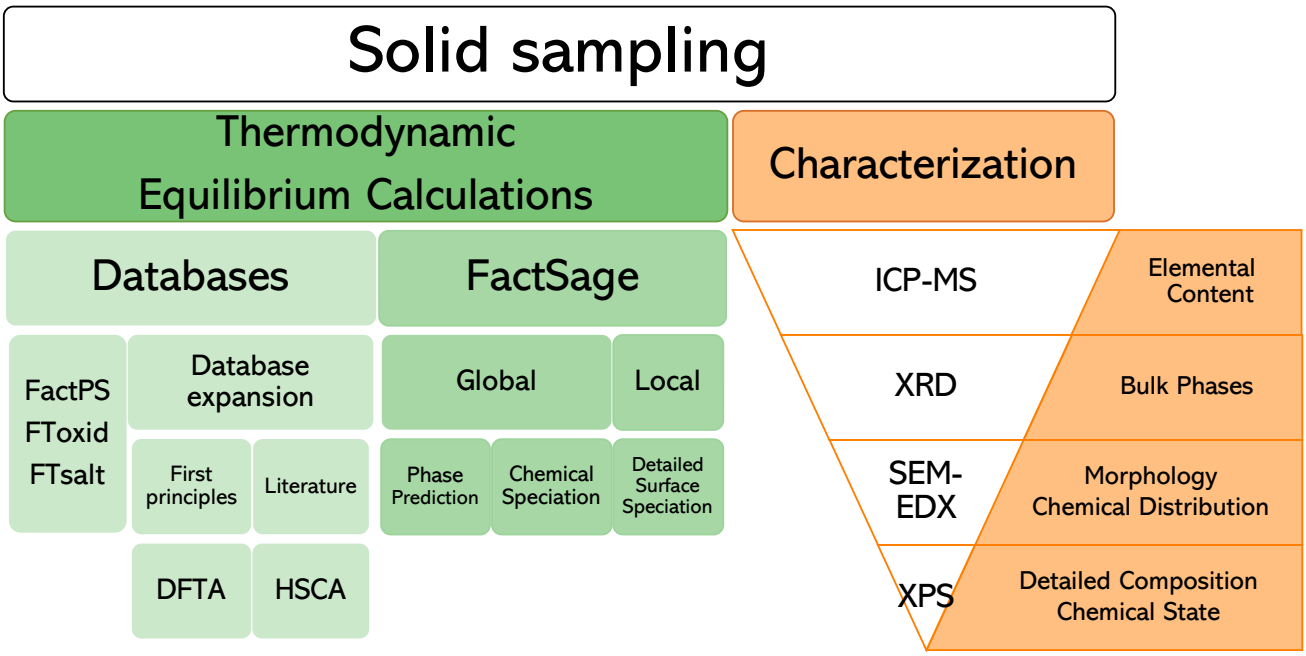

Figure 5. Summary of the theoretical and experimental approaches used for studying the inorganic species in solid samples.

Elemental content. The concentrations of elements in solid samples were determined by Inductively Coupled Plasma – Sector Field Mass Spectrometry (ICP-SMFS), which has the lowest detection limits of any ICP-MS method. The analysis was carried out by the external company, ALS Scandinavia AB. Solid samples were prepared by borate fusion. The sample was first mixed with lithium tetraborate, and then heated until a homogenous melt was obtained. The mixture was then dissolved in HNO_3 and the solution was analyzed by ICP-SMFS according to ISO 17294-2: 2016.

Crystalline Phases. Crystalline phases were determined using powder X-Ray Diffraction (XRD) with $CuK_{\alpha 1}$ radiation in the Bruker D8 Advanced system (**Papers I**–**V**), and in the PANalytical Empyrean (**Paper X**). The samples were lightly crushed in a mortar before being analyzed. Scans were made using the settings (40k V, 40 mA) over a 2θ-range between 20° and 80° with a step size of 0.05° and a counting time of 2 s/step. The recorded spectra were compared qualitatively to diffraction patterns from existing databases (ICDD PDF-4+), to obtain crystallographic information. Diffraction patterns from the databases were used for qualitative evaluations. Thus, spectra were collected from the entire sample, not only the surface but also the bulk. This gave an overview of all the phases present in the sample. Since the interaction between OCs and inorganic species occurs through the particle surfaces, it is also of interest to utilize a surface characterization method.

Morphology and chemical distribution. Morphology was examined using SEM. The microscope was coupled to an Energy-Dispersive X-ray spectroscopy (EDX), to allow the study of elemental distributions. Two preparation methods were used to study the particle surfaces and cross-sections. The morphology was studied by mounting the particles on conductive carbon tape. To study the particle cross-sections, particles were immobilized in a mixture of epoxy and hardener. When cured, the samples were polished stepwise to expose the particle cross-section. Thus, knowledge of the distributions of inorganic ash species within the particles and ash layers could be obtained. For this purpose, backscattered electron signals were used for imaging. The system used for imaging and chemical mapping was the Quanta 200FEG coupled to the Oxford EDX system (**Papers I**–**V** and **VIII**), and using Prisma ESEM from Thermo Scientific (**Paper X**).

To ensure that a representative particle was analyzed, samples were studied stepwise using the following procedure. First, chemical mappings of a multitude of particles were analyzed concerning the chemical distribution of the heavy metals across the sample. Thereafter, the magnification was increased and a selection of particles representing the sample was further studied by chemical mapping, point analyses, and line scans. The ash layers were investigated in more detail using a depth profile. The ilmenite samples obtained from Händelö and Örtofta were heterogeneous. Nevertheless, based on the particle size, the concentrations of ash compounds in the particles, and the morphology, it was possible to compare the particles based on residence time. Fresh ilmenite particles have less time to interact with the ash compounds. With increased exposure time, particles are covered with a calcium layer that migrates toward the ilmenite core. Therefore, particles that are covered in calcium are considered to have been exposed to ash for a longer period.

Trace elements and chemical states. X-ray Photoelectron Spectroscopy (XPS) was used for surface material characterization, as it provides elemental and chemical state information for solid samples. Another strength of this method is the low detection limits, allowing the detection of elements at levels as low as 0.1 at%, which is critical for studying low-concentration trace metals. The PHI 5000 VersaProbe III Scanning XPS Microprobe (base pressure, 1×10^{-9} bar) was used with a monochromated Al-source (25 W) and beam size of 100 μm. A dual-beam flood of low-energy electrons and low-energy argon ions was used to provide charge neutralization for measurements of non-conductive materials. Analysis points were based on x-ray-induced secondary electron imaging (SXI), allowing one to accurately specify accurately the points. Surface features were investigated by mounting the particles on carbon tape, while studies of cross-sections required molding of the particles in epoxy. Surface contaminants were removed by blowing the sample with dry nitrogen gas. The survey scan was performed in the range of 0–1,250 eV (pass energy, 224 eV; step size, 0.4 eV) for the compositional analysis. The high-resolution narrow scan was performed in specific regions for chemical state analysis (26 eV; step size, 0.1 eV). The energy scale calibration (ISO 15472) was performed by aligning

the core level peaks of Au $4f_{7/2}$, Ag $3d_{5/2}$, and Cu $2p_{3/2}$ at 83.95 eV, 368.21 eV, and 932.64 eV, respectively. Charge referencing was made to the adventitious C 1s line at 284.8 eV, to calibrate the binding energies of other elements. The region spectra were fitted using the Multipak software. Peak constraints regarding the area ratios and spin-orbit separation were defined as reported in the literature. [119, 120] In the quantitative analyses of surface composition, the peak areas of each element were normalized according to the atomic sensitivity factors (ASF) provided by the software Multipak 9.7.0.1. [119] For the chemical state identification, selected region spectra were recorded that covered the C 1s, O 1s, K 2p, Na 1s, Pb $4f_{7/2}$, Cu $2p_{3/2}$, and Zn $2p_{3/2}$ peaks.

4.2 Positive Matrix Factorization

Positive Matrix Factorization (PMF) is a multivariate factor analysis technique that is used to analyze a wide range of data. As part of this thesis, the method was developed for phase recognition in chemical maps obtained by SEM-EDX. The procedure involves converting chemical maps into vectors. Initially, the images are digitized and arranged using MatLab. Thereafter, the high number of variables in these datasets are reduced by PMF to combinations of species, called ‘factors’. [121] The open-source software EPA PMF 5.0 was used for the data treatment. [122] The procedure is described in detail in **Paper IX**.

5

THERMODYNAMIC EQUILIBRIUM CALCULATIONS

In the work covered in this thesis, TECs were performed using the FactSage 7.2-8.2 software. [111] TECs are based on minimizing the Gibbs free energy, which calculates the chemical equilibrium composition of a system considering the thermodynamic data for all possible phases and compounds. A detailed description of the procedure is given in Section 5.4.

5.1 Local and Global TECs

Two types of calculations, global and local, were performed in this work. Local TECs were based on local conditions in the boiler. Simplified systems, with only a few components, were investigated to understand specific reactions. Local calculations were also utilized to identify missing compounds in the databases, as they could be related to experimental results by using, for example, the composition of the particle surface or cross-section as input. For this purpose, the surface composition, as obtained by XPS, was used as input to the calculations. Studying the outermost surface of a specific particle is important, as this area is in direct contact with the surrounding gas phase and is the primary point of interaction. The calculation output provides the equilibrium compositions of the gaseous, stoichiometric, and solid solution components.

Global equilibrium calculations were used to study the phase stability and phase distribution, as well as the effect of parameter variation on the interaction between ash components and OCs. These calculations used the following flows as input: i) fuel composition; ii) bed material; and iii) fluidizing gas. The TE phase stability in chemical looping was investigated for the fuel-bed material combinations of: ASR-olivine, MSW-ilmenite, MSW-silica sand, and RWW-ilmenite.

5.1.1 Global TECs – CLC of Solid Fuels

In **Papers VI** and **XI**, the expanded databases were utilized to study the phase transitions and the chemical distribution of TEs during CLC of solid fuels. Four OCs were studied, namely ilmenite, Fe oxide, Mn oxide, and Mn ore. The amount of OC needed to maintain a temperature of 950°C in the FR was determined with a heat balance over the FR, as it has been shown previously that it is often the transport of sensible heat from the AR to FR that dictates the minimum circulation rate that is required. [123] The following assumptions were made: (i) the FR is adiabatic; (ii) the OC entering the FR is fully oxidized with a temperature of 1,050°C;

and (iii) the FR is fluidized with CO_2, preheated to 400°C. Temperature and reduction levels were assumed to be homogeneous in the reactors. The oxygen concentration in the AR exhaust gas was 5% and the AR was fluidized with air that was preheated to 400°C. Further details are presented in **Papers VI** and **XI**.

5.2 Oxygen Partial Pressure

As described in Section 3, the fluidizing gas and gas atmospheres in the reactors differ between chemical looping technologies. The boiler in OCAC is fluidized with air, while the FRs in CLC and CLG are commonly fluidized using H2O or recirculated CO2. For this reason, the OCs and gaseous components are expected to be in a more reduced state in the FR in CLC and CLG. Furthermore, the oxygen transfer from OCs to the fuel is expected to be lower in CLG compared to CLC, as only partial combustion is desired in the former technology. [124] Thus, one of the most important parameters investigated in this thesis is the oxygen partial pressure, as it is expected to vary both within the reactors and across technologies, and this will have an impact on the chemical speciation of inorganic species. The reduction potential is coupled to the available oxygen in the boiler, which determines the oxidation state of the inorganic species. Therefore, the phase distribution was studied over a range of reduction potentials, also expressed as the logarithmic oxygen partial pressure. The gas phase compositions during the conversion of a waste-derived fuel are illustrated in Figure 6. The figure shows the gas compositions at different λ-values and their relationships to the major components of CO_2, CO, H_2O, and H_2, as well as HCl, H_2S, and SO_2. Different thermochemical conversion processes and their relationships to the oxygen partial pressure may be distinguished in the figure. For example, pyrolysis is carried out at air-fuel equivalence ratios between 0 and 0.25, gasification occurs at up to 1.0, and combustion occurs above 1.0. [125]

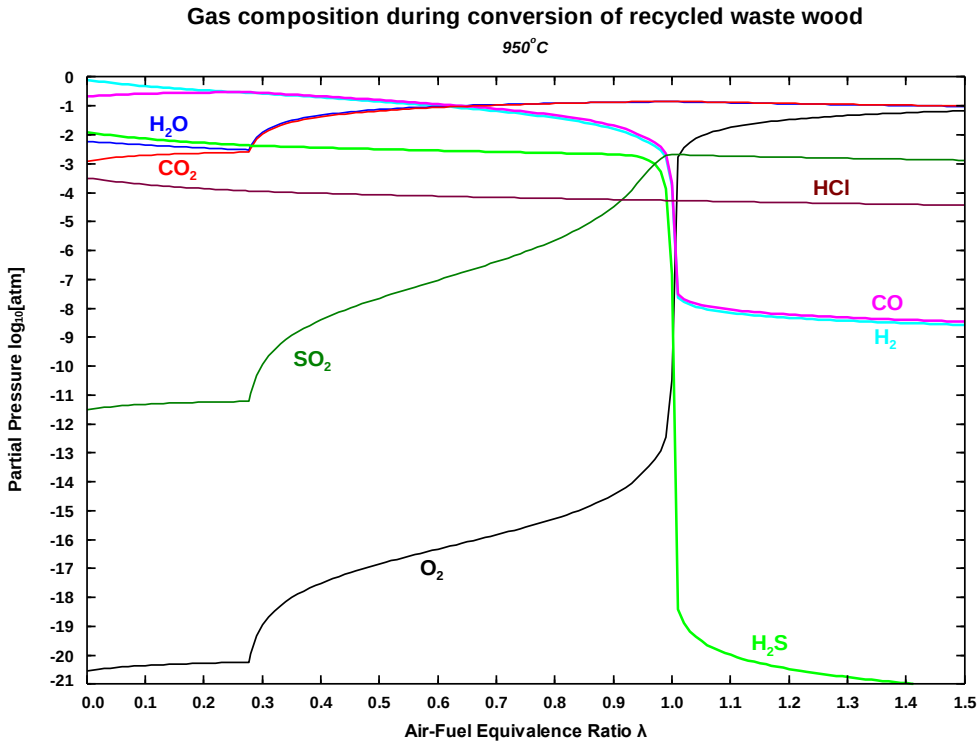

Figure 6. Gas composition during thermochemical conversion of recycled waste wood at 950°C as a function of the air-fuel equivalence ratio λ.

During combustion, air is supplied in excess, and the oxygen partial pressure at the outlet of these applications is around 5 vol%, $pO_2 = 10^{-1.3}$ atm. Similar conditions are encountered in OCAC and, for example, in the AR during CLC and CLG. In the FR, the oxygen is supplied by the OC and the oxygen partial pressure can be determined from the known concentrations of CO and CO_2. This ratio is referred to as the reduction potential pCO/pCO_2. The equilibrium oxygen partial pressure at a specific temperature can be calculated with the equilibrium constant K_{eq}, from the reaction: $CO+½O_2 \rightarrow CO_2$ according to Equation (9).

$$pO_2(T) = \left(\frac{p(CO_2)}{p(CO)} \frac{1}{K_{eq}(T)}\right)^2 \quad (9)$$

A summary of the oxygen partial pressures in the FR-outlet during CLC is presented in Table 3. The values are based on the gas-phase composition reported in the literature. The table shows that oxygen partial pressures around $pO_2 = 10^{-13.5}$ atm are expected in an FR that is operating at 950 °C.

Table 3. The oxygen partial pressures from the FR during CLC, calculated from the outlet gas-phase compositions reported in the literature.

Oxygen carrier	Unit	$\log_{10}(pO_2)$ at 950°C [atm]	Reference
Hematite, ilmenite, manganese oxides	Tubular furnace	-12.8	**Papers I** and **II**
Ilmenite	Tubular furnace	-13.4	[49]
LD-slag and iron mill scale	TGA[A], tubular furnace	-13.4	[126]
Ilmenite	TGA[A]	-(14.8–17.5)	[127]
Ilmenite and calcium manganite	100 kW, continuous	-12.9	[128]
Tierga iron ore	Fluidized batch reactor	-(14.8–15.2)	[129]
Iron ore	Fluidized batch reactor	-13.1	[39]
Hematite	1 kW_{th}, continuous	-(14.4–14.9)	[130]
Iron ore	Fluidized batch reactor	-21.9[B]	[131]

[A] Thermogravimetric analysis.
[B] Gas composition of synthetic MSW-derived syngas.

When utilizing OCs, the outermost parts of the particles will be in contact with the surrounding gas, with a composition similar to that shown in Figure 6. However, the particle core will not be in contact with the surrounding gas and, therefore, higher reduction potentials can be encountered locally across particles. Therefore, lower oxygen partial pressures not only represent the different fuel reactors, but also the oxygen-deficient parts of the boiler and conditions deeper inside the particle.

5.3 Database Expansion

In the work covered in this thesis, TECs were performed using the FactSage software, together with the FTsalt and FToxid databases, and the pure-substance database FactPS. These databases were combined with other databases, and DFT-generated data, as explained below and presented in Figure 7.

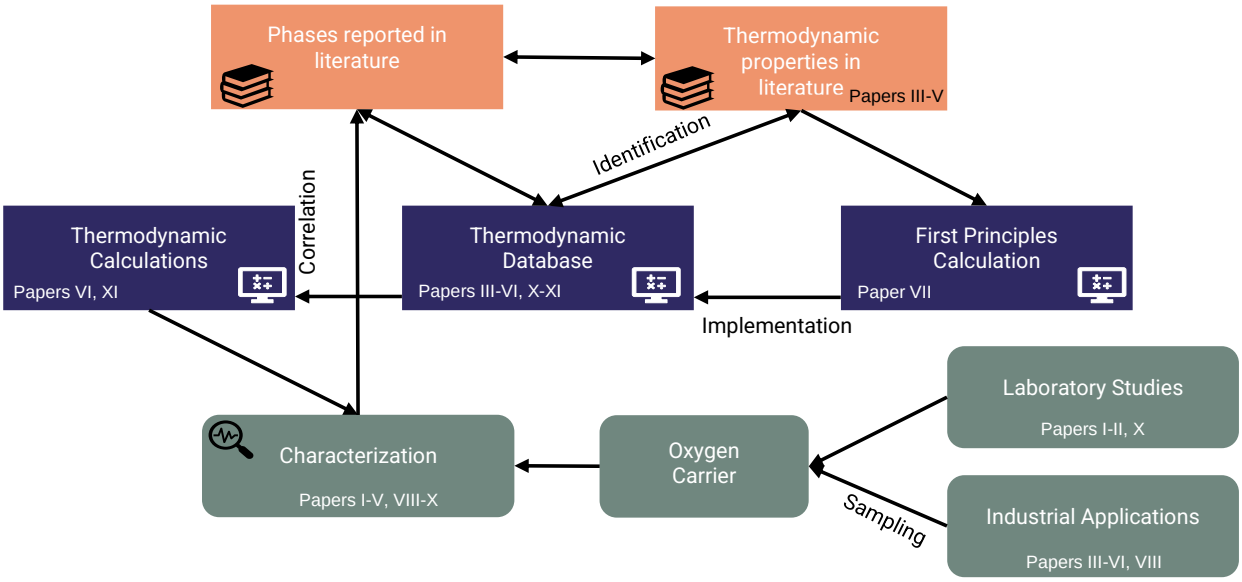

Figure 7. The methodology used for expanding the databases and the relationships to the appended papers.

5.3.1 Thermodynamic Properties from the Literature

Based on the available data in the literature, important thermodynamic data not available in the Fact databases were extracted for both stoichiometric solid phases and one Mn-based perovskite, as described below.

Stoichiometric phases. As stated in Section 3.5, HSC Chemistry contains the most data concerning heavy metals. Therefore, heavy metal compounds were extracted from HSC to create a new database, referred to as HSCA. HSCA includes compounds from HSC Chemistry 9 **(Papers III** and **IV)** and HSC Chemistry 10 (**Papers V–VI**, **X** and **XI**). The compounds added to this database are summarized in *Appendix*, and include trace elements and compounds of As, Co, Cr, Cu, Mn, Mo, Ni, Pb, V, and Zn. Thus, improving the quality of the calculations concerning these species.

Non-stoichiometric perovskite. Perovskite materials, especially $CaMnO_{3-\delta}$, are of interest for both CLC and CLOU. However, thermodynamic data are only available for stoichiometric $CaMnO_3$, which leads to significant discrepancies between experiments and calculations (for details, see **Paper XI**). This perovskite contains oxygen defects, the proportion (δ) of which is determined by the oxygen partial pressure of the surrounding gas. The problem is, thus, to develop a method that can be used to estimate the variations of the enthalpy, entropy, and heat capacity with the non-stoichiometry δ. To address this issue, a semi-empirical model, originally proposed by Goldyreva et al. [132] was used to calculate the differences in the heat capacity, formation enthalpy and entropy of $CaMnO_{3-\delta}$ relative to $CaMnO_3$. Thermal data were generated for different degrees of oxygen vacancies by adding correction terms, calculated via a semi-empirical model for δ in the range of 0–0.5, in steps of δ=1/64. This information was, in turn, combined with the data for the stoichiometric phase derived from the FToxid database.

5.3.2 Thermodynamic Properties from First Principles

In cases where little or no data are available in the literature, one solution is to generate thermodynamic data from first-principles calculations. Some previous studies have utilized first-principles calculations to study iron-based OCs. [57, 133] However, implementation in thermodynamic databases for multicomponent, multiphase equilibrium calculations has not been performed previously to our knowledge. Combining calculated thermodynamic properties with data from existing databases makes it possible to investigate the stabilities of missing compounds. This new data can contribute to increasing understanding and to accurately predicting or explaining experimental observations.

The method utilizes a procedure similar to that proposed by Benisek and Dachs for predicting thermodynamic parameters for complex metal oxides. [134] A schematic overview of the procedure is given in Figure 8. In this approach, ground-state configurations are first identified by constructing cluster expansions. These expansions are also used to calculate the contribution to the heat capacity of chemical ordering. The reaction energies are computed using density functional theory, as well as the phononic contribution to the heat capacity under the harmonic approximation. Following the procedure presented by Benisek and Dachs, the results from these ab initio calculations were combined with experimental data from the NIST-JANAF thermochemical tables, to determine the enthalpy and entropy at room temperature, together with the temperature-dependence of the heat capacity. Using this approach, data for experimentally identified compounds were calculated from **Papers I** and **II**, for which no data could be found in the literature.

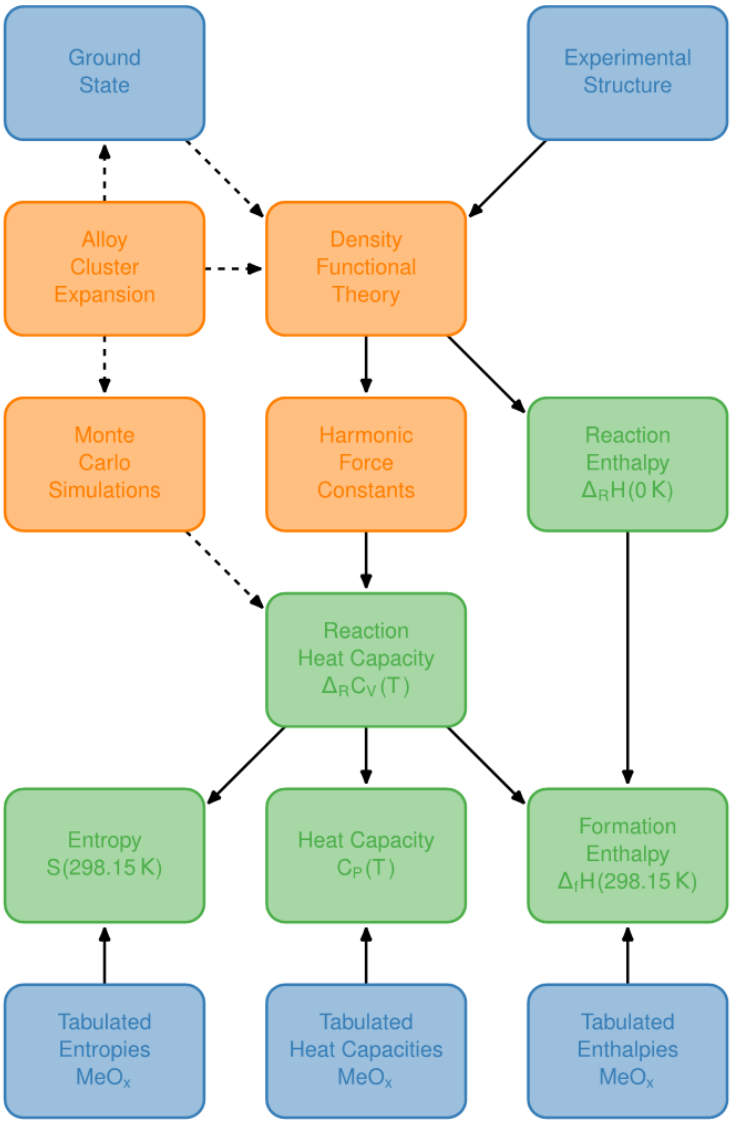

Figure 8. Schematic illustration of the procedure for estimating the entropy, formation enthalpy, and heat capacity using a combination of first-principles calculations and tabulated experimental data for metal oxides (MeO_x).

5.4 Minimizing Gibbs Free Energy

The main equations and procedure for the TECs will be presented in this section. For detailed information, the reader is referred to other sources. [111, 135 , 136, 137] Thermodynamic equilibrium calculations are used to determine the stable chemical and physical forms in a system. Data are stored in databases that include information on the standard reference state (T_{ref}=298.15 K, P_{ref} =1 bar) of enthalpy (H_f°) and entropy (S_f°), enthalpy change and temperature during phase transitions ($\Delta H_t, T_t$), and polynomial expressions of heat capacities ($c_p(T)$). These are then used to calculate the enthalpy, Equation (10), and entropy. Equation (11), at given temperature T.

$$H(T) = H_f^\circ + \int_{T_{ref}}^{T} c_p(T)dT + \sum \Delta H_t \tag{10}$$

$$S(T) = S_f^\circ + \int_{T_{ref}}^{T} \left(\frac{c_p(T)}{T}\right) dT + \sum \left(\frac{\Delta H_t}{T_t}\right) \tag{11}$$

The Gibbs free energy (G) is defined as in Equation (12) and can be calculated using the stored values from the databases, and from Equations (10) and (11). [137]

$$G(T) = H(T) - TS(T) \tag{12}$$

In multiphase, multicomponent systems, equilibrium at constant pressure and temperature occurs at a minimum Gibbs free energy, and the minimization of G is performed under a mass balance constraint. The equilibrium condition is to minimize the Gibbs free energy in Equation (13):

$$\mathrm{G} = \sum_{\Phi} \left(\sum_{i} n_i^{\Phi} \right) G_m^{\Phi} \tag{13}$$

where G_m^{Φ} is the molar Gibbs free energy and n_i^{Φ} is the molar quantity of the phase constituent i in the phase Φ. The outer sum runs over all phases (Φ) and the inner sum runs over the respective phase amount (n_i^{Φ}). Along with the equilibrium condition to minimize Equation (13), the mass balance, Equation (14), needs to be conserved:

$$\sum_{\Phi} \sum_{\mathrm{i}} n_i^{\Phi} a_{i,j}^{\Phi} = b_j \tag{14}$$

where n_i is the molar quantity of species i, $a_{i,j}$ is the stoichiometric coefficient, and b_j is the molar quantity of component j. Furthermore, the Gibbs phase rule also needs to be satisfied. The Gibbs phase rule describes the number of components (C) and phases (P) that can be varied freely in a system. For example, the three variables in a chemical system are temperature, pressure, and chemical composition. In a multicomponent system, the mole fractions in a phase can all be varied freely except for one, since the sum must be equal to one. Thus, in one phase the composition is defined by (C-1) fraction terms. In total, this results in P(C-1)+2 number of variables, including two state variables that can be varied freely (temperature and pressure). Given that the system is in equilibrium, the chemical potential μ_i^{Φ} for a given chemical component must be equal in all coexisting phases. This results in a total of C(P-1) constraints. The net number of degrees of freedom (F) is then determined by adding all the variables and subtracting the number of thermodynamic constraints, resulting in F= 2+P(C-1)-C(P-1)=2+C-P. This correlates the number of phases under equilibrium directly to the number of components.

Several methods can be used to minimize the Gibbs energy in multicomponent systems with the constrictions defined above. [138, 139] For example, the Lagrange method of undetermined multipliers can be applied. The minimization of the Lagrangian function L in Equation (15) is equivalent to the minimization of Equation (13).

$$L(n, M) = G - M_j \left(\sum_{\Phi} \sum_{\mathrm{i}} n_i^{\Phi} a_{i,j}^{\Phi} - b_j \right) \tag{15}$$

where M_j is the Lagrange multiplier and b_j is the amount of the j^{th} system component (often element). Consequently, a set of equations is derived according to Equation (16).

$$\frac{\partial L(n, M)}{\partial n_i} = \left(\frac{\partial G}{\partial n_i} \right)_{T,P}^{\Phi} - \sum_{\Phi} \sum_{\mathrm{i}} a_{i,j}^{\Phi} M_j = 0 \tag{16}$$

The mass balance constraint may be represented by the matrix $a_{i,j}$. To illustrate, a simple example describing the system ZnO–Fe_2O_3 in air is used. The corresponding stoichiometric

matrix $a_{i,j}$ is presented in Table 4. Usually, there are more species i than components j in a system.

Table 4. Example of the stoichiometric matrix $a_{i,j}$ for ZnO and Fe_2O_3 exposed in air.

Phase Φ	Constituents	Species i	Stoichiometric coefficient $a_{i,j}$ of system components j			
			N	O	Zn	Fe
Gas	N_2	Gas_N_2	2			
	O_2	Gas_O_2		2		
	Zn	Gas_Zn			1	
	ZnO	Gas_ZnO		1	1	
Stoichiometric solids	Zn	Solid_Zn			1	
	ZnO	Solid_ZnO		1	1	
	Fe	Solid_Fe				1
	FeO	Solid_FeO		1		1
	Fe_2O_3	Solid_ Fe_2O_3		3		2
	Fe_3O_4	Solid_ Fe_3O_4		4		3
	$ZnFe_2O_4$	Solid_ $ZnFe_2O_4$		4	1	2

To calculate the equilibrium composition, an iterative procedure can be used to obtain a set of molar quantities that yield the lowest value of the Gibbs free energy while satisfying the mass balance constraint and the phase rule. For a given composition b_j, n_i^{Φ} and M_j need to be determined. This requires an initial estimation, which is tuned in each iteration. At equilibrium, the Lagrange multiplier M_j represent the chemical potential of the system components. It is evident from the matrix in Table 4 that the number of equations will increase when adding components, species, and phases to the system. The numerical complexity is further increased when, for example, solid solutions are included. From Equations (13) and (16), it is evident that expressions for the Gibbs free energy are needed for each of the phases of stoichiometric, gas compounds, and solutions. In the following sections, different contributions and expressions for Gibbs free energy will be discussed.

5.4.1 Gibbs Free Energy for Stoichiometric Solids

Pure stoichiometric substances require that the Gibbs free energy $G_m^{\phi}(T,P)$ is known as a function of temperature (T) and pressure (P). Three different contributions may be distinguished and treated separately.

$$G_m^{stochiometric\ solids}(T,P) = G_{lattice}^{\phi} + G_{magnetic}^{\phi} + G_{pressure}^{\phi} \tag{17}$$

1. The major contribution is expected to originate from $G_{lattice}^{\phi}$. This term depends on the database standard enthalpy of formation, standard entropy of formation, and the heat capacity. The calculation of $G_{lattice}^{\phi}$ is performed using Equation (12), which utilizes the stored data and combines Equations (10) and (11).
2. $G_{magnetic}^{\phi}$ depends on the critical temperature (T_c) and the magnetic moment (β). The lattice structure is considered in the function $f\left(\frac{T}{T_C}\right)$, which differs depending on whether the temperature range is above or below the critical temperature.

$$G_{magnetic}^{\phi} = RTf\left(\frac{T}{T_C}\right) ln(\beta + 1) \tag{18}$$

3. $G^{\phi}_{pressure}$ depends on the standard molar volume (V^o), compressibility at 1 bar (K(T)), and thermal expansion (α(T)). Compressibility and thermal expansion coefficients are commonly expressed as polynomials. However, the pressure term is usually negligible and only a few substances have the relevant data available.

$$G^{\phi}_{pressure} = f(V^o, \propto(T), K(T), T) \tag{19}$$

5.4.2 Gibbs Free Energy for Gas-Phase Components

The gas phase is often treated as ideal during calculations, although it is possible to include virial coefficients and use the truncated virial equation of state to treat real gases:

$$\frac{PV}{RT} = 1 + \frac{BP}{RT} \tag{20}$$

where B is estimated from the critical temperature T_c, critical pressure P_c, and acentric factor ω. When treating an ideal gas, B is set to zero and minimization of the Gibbs free energy is performed to determine the fraction of species in the gas phase. Thereafter, Equation (21) is used to determine G^{gas}_m, where y_i represents the mole fraction among species.

$$G^{gas}_m(T,P) = \sum_i y_i G_i + RT \sum_i y_i ln y_i + RT lnP \tag{21}$$

5.4.3 Gibbs Free Energy for Solutions

While stoichiometric compounds require temperature and pressure, a solution also requires the quantity of each phase component $G^{\phi}_m(T,P,x_i)$, for example, solid solutions that have a range of compositions. Thus, for solution phases (ϕ), the Gibbs free energy consists of three contributions:

$$G^{\phi}_m(T,\mathrm{P},x_i) = G^{\phi,standard\ state}_m + G^{\phi,ideal}_m + G^{\phi,excess}_m \tag{22}$$

1. The properties of a solution are usually described relative to the properties of the pure phase components at the same pressure and temperature. The first term in Equation (22) is called the standard state term and contains the contribution of pure phase components. $G^{\phi,standard\ state}_m = \sum_i x_i G^{\phi}_i$, where x_i is the mole fraction of constituent i.

1. For an ideal solution, the term $G^{\phi,ideal}_m = RT \sum_i x_i ln x_i$ is considered, which arises due to the entropy of ideal mixing of the constituents.

2. The non-ideal or so-called 'excess' term needs to be described by some mathematical expression. This excess term is crucial for modeling eutectic mixtures or miscibility gaps. Therefore, it is important that these equations consider different types of bonds next to neighbors (AA, BB, and AB). Data are often available for binary systems, and these need to be extrapolated because information on higher-order systems is scarce. FactSage includes different solution models, for example, one and two-lattice polynomials [140], one and two-lattice quasichemical [141], and Redlich-Kister/Muggianu model. The complete set of available solution models can be found elsewhere. [142] Taking the one-lattice polynomial model as an example, random mixing of species is assumed (Bragg-Williams model) on a single lattice. The excess molar Gibbs free energy is expressed as a polynomial (of the type simple, Legendre, or Redlich-Kister) in terms of site fractions. Then, the binary parameters are interpolated

into ternary systems using either the Kohler, Toop, or Muggianu approximations, or a combination of these techniques. To illustrate the complexity of the expression for the excess term, a restricted version of the one-lattice polynomial model called one lattice Redlich-Kister/Muggianu model is presented below. The model is restricted because binary interaction terms are expressed only as Redlich-Kister polynomials and binary terms are interpolated into ternary by the Muggianu approximation. The Redlich-Kister/Muggianu model for a solid solution with only one lattice site with random occupation is presented in Equation (23). The interaction parameter, *L*, is often called the interaction energy.

$$G_m^{\phi,excess} = \sum_i \sum_{<j} x_i x_j \sum_{v=0}^{n_{i,j}} L_{ij}^v(T) \left(x_i - x_j\right)^v + \frac{\sum_i \sum_{<j} \sum_{<k} x_i x_j x_k \left(x_i L_i^{ijk}(T) + x_j L_j^{ijk}(T) + x_k L_k^{ijk}(T)\right)}{x_i + x_j + x_k} \quad (23)$$

In this thesis, the modules *Equilib* and *Phase Diagram* in FactSage were used. *Equilib* determines the combination of n_i^{Φ} and x_i/y_i that minimizes the total Gibbs free energy of the system at defined T and P values, including the gas phase, pure stoichiometric components, and solid solutions with data from selected databases. A flow sheet summarizing the procedure for multicomponent, multiphase equilibrium calculations is presented in Figure 9, and a summary of the solution phases and their associated solution models is presented in Table 5.

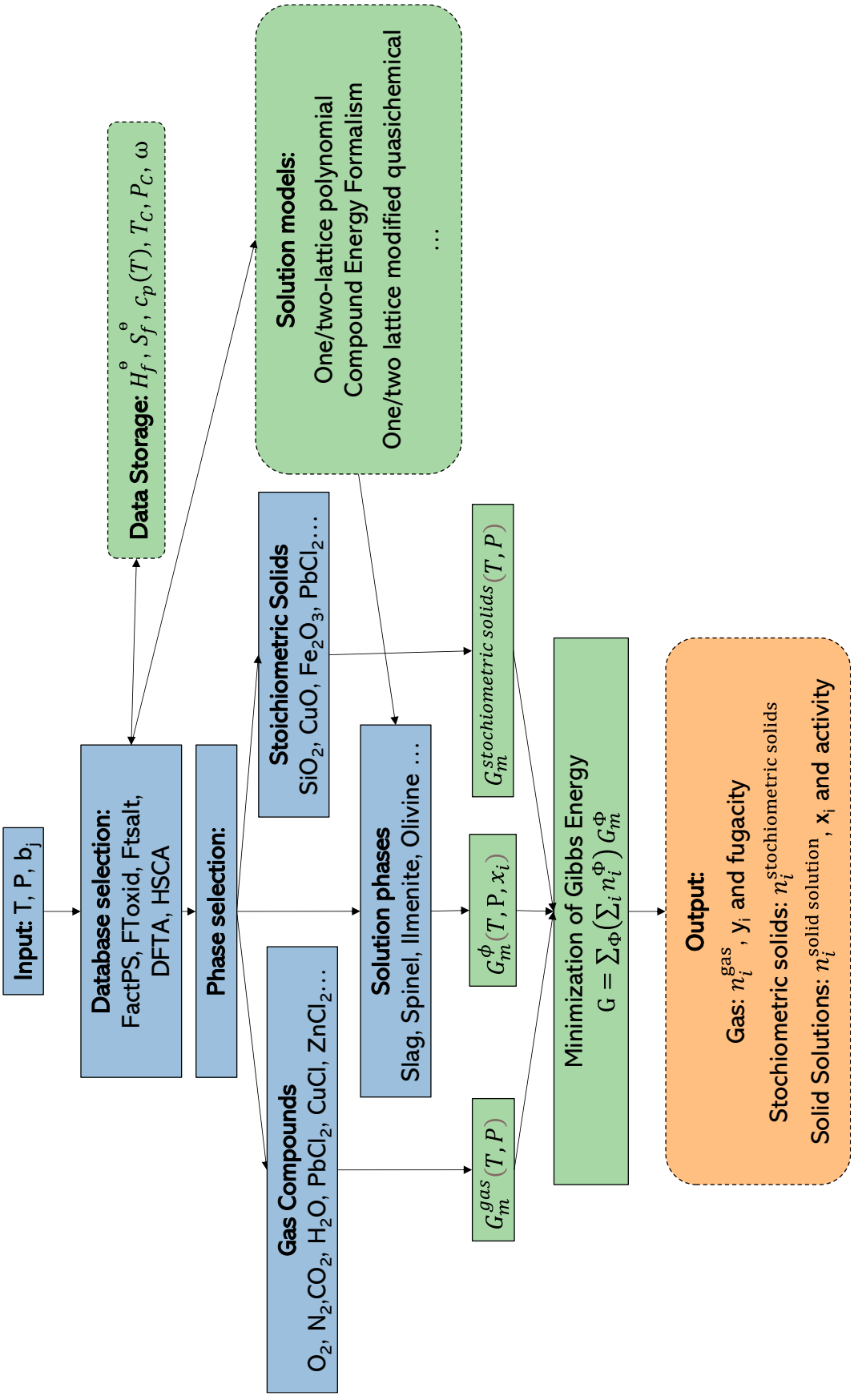

Figure 9. Workflow utilized in FactSage for TECs. User defined inputs and settings in blue, output in orange and solution models, data storage and calculations performed by FactSage program in green.

Table 5. List of the solutions, the associated solution model, number of end-members (EM) and elements in the solution, the general formula and major constituents.

Solid Solutions	Solution model	EM	Elements	General formula	Major constituents
Spinel	Compound Energy Formalism	100	8	AB_2O_4	A = Al, $Fe^{2+/3+}$,Mg, Zn B = Al, $Fe^{2+/3+}$,Mg, Zn,
Ilmenite		8	5	ABO_3	A = Fe^{2+}, Mg B= $Ti^{3+/4+}$
Olivine		49	9	$ABSiO_4$	A, B = Ca, Fe, Mg, Mn, Zn
Bredigite		2	4		$Ca_3(Ca,Mg)_4Mg(SiO_4)_4$
Tetragonal spinel		64	6	AB_2O_4	A = Mn, Fe B = Mn, Fe
Melilite		30	8	ABC_2O_7	A = Ca, Pb B = Mg, $Fe^{2+/3+}$, Al, Zn C = Al, $Fe^{2+/3+}$, Si
Willemite		16	6	$ABSiO_4$	A, B = Zn, Fe^{2+}, Mg
Leucite		2	5		$K_2Al_2Si_4O_{12}$-$K_2MgSi_5O_{12}$
Clinopyroxene		36	12	$ABCSiO_6$	A = Ca, Fe^{2+}, Mg B = Mg, $Fe^{2+/3+}$, Al C = Si, Al, Fe^{3+}
(Na)(Al,Fe)O2		6	5		SiO_2 + $Na(Fe,Al)O_2$
Rutile	Polynomial	3	3		TiO_2
Wollastonite		6	8		$CaSiO_3$
Monoxide		18	17	AO	Fe, Mn, Mg, Ca, Ca, Zn, Cu, Na
Perovskite		2	3		$Ca_2Ti_2O_6$ - $Ca_2Ti_2O_5$
M2O3		8	8	A_2O_3	A = Fe, Mn, Al
Pseudobrookite	Sublattice	8	5	AB_2O_4	A=Fe, Ti, Mg B=Ti
Titania Spinel		18	6	AB_2O_4	A = Fe, Mg B = $Ti^{3+/4+}$, Mg, Fe, Mn, Al
Nepheline	Modified quasichemical (quadruplets)	6	7		(Na,K)$AlSiO_4$, dissolving SiO_2
Slag-liq		126	28		SiO_2 + $(Na,K)AlO_2$ + (Na_2, K_2, Cu_2, Ca, Mg, Pb, Zn)(O,S)
Salt-F		18	10	AB	A = Na, K, Zn, Pb, Fe B = Cl, SO_4
Feldspar	Quasichemical (quadruplets)	6	9	$ABAlSi_2O_8$	A = K, Na, Ca B=Al, Si

6

EXPERIMENTAL SECTION

6.1 Laboratory Experiments

Laboratory-scale experiments were conducted in a fixed bed reactor to study the interactions between K- and Ca-bearing ash compounds and iron-based (**Paper II**) and Mn-based OCs (**Papers I** and **II**). The interactions between ilmenite and gaseous zinc species (**Paper X)** were studied in a separate setup based on a tubular fixed-bed reactor. These experimental setups are described below.

6.1.1 Experiments with Inorganic Salts

Laboratory-scale experiments were conducted to investigate the interactions of Fe-based and Mn-based OCs with potassium and calcium salts. By exposing the ash components together with OCs in oxidizing and reducing environments, it is possible to investigate the important interactions that occur in the AR or FR. OC and ash mixtures were exposed to oxidizing and reducing conditions in fixed-bed tubular furnaces. The setup is presented in Figure 10. The furnace was heated to 900°C and the holding time was 6 hours, after which the furnace was cooled down. Air was used for the oxidizing conditions, and 2.5% H_2, 47.5% Ar, and 50% H_2O were used for the reducing conditions, which correspond reasonably well with the reduction potential in an FR during CLC. The reduction potential (pH_2/pH_2O) is 0.05 and corresponds to an equilibrium partial pressure of O_2 of $\log_{10}p(O_2)$=-13.7 atm at 900°C. Post-exposures, samples were analyzed with XRD and SEM/EDX, as described further in Section 4.1.

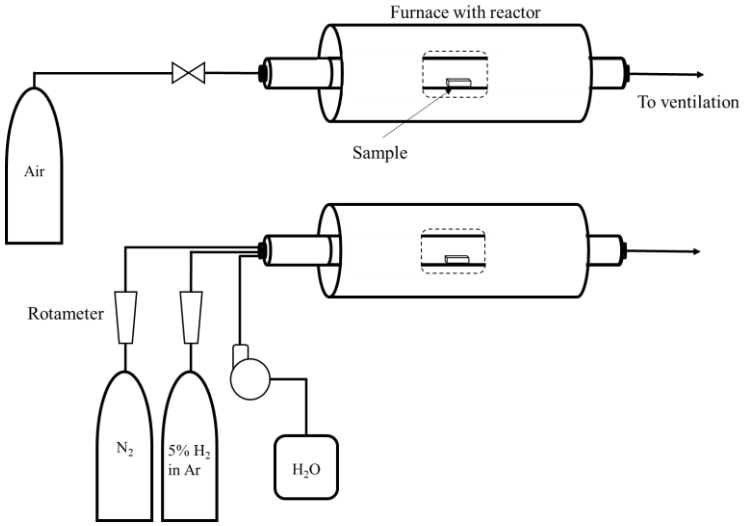

*Figure 10. Schematic overview of the experimental system used to study the interactions between inorganic salts and oxygen carriers (**Papers I** and **II**).*

6.1.2 Experiments with Gaseous Zinc Species

Laboratory-scale experiments were conducted to investigate the chemistry of the interactions between gaseous zinc compounds and ilmenite. Prior to the experiments with zinc, a fluidized bed reactor [143] was used to prepare some of the OC particles, as described further in **Paper X**. Experiments with zinc compounds and ilmenite were, thereafter, performed in a vertical reactor setup that consisted of a fixed-bed quartz reactor, enclosed in an electrically heated furnace. Downstream of the reactor, filters were installed to remove any particles entrained in the off-gas, and this was followed by heated gas lines and a gas analyzer, as schematically illustrated in Figure 11. The temperatures at the positions where metallic Zn and $ZnCl_2$ were located were 715°C and 640°C, corresponding to equilibrium partial pressures of 0.1 and 0.21 atm for Zn and $ZnCl_2$ vapors, respectively. The temperature at the position of the ilmenite was 900°C for the metallic zinc experiments and 850°C for the $ZnCl_2$ experiments, as these are average temperatures in an FR during CLC and OCAC, respectively. For the $ZnCl_2$ experiments, the nitrogen flow passed through a bottle filled with deionized water, thereby creating a flow with ~2 vol% H_2O. Common to the experiments with $ZnCl_2$ and Zn was that the system was heated in a nitrogen atmosphere and the samples were left to cool inside the reactor in a nitrogen atmosphere before being collected and analyzed. Experiments were conducted for 60 minutes to ensure complete devolatilization of the zinc compounds. The produced gases passed through heated filters and gas lines before reaching the Fourier Transform InfraRed (FTIR) spectrometer of type Gasmet DX-4000, with the sampling cell and lines being heated to 180°C to avoid condensation. The spectrometer monitored the concentrations of H_2O, HCl, and SO_2. Samples obtained after the experiments were analyzed with XRD and SEM/EDX, as described further in Section 4.1.

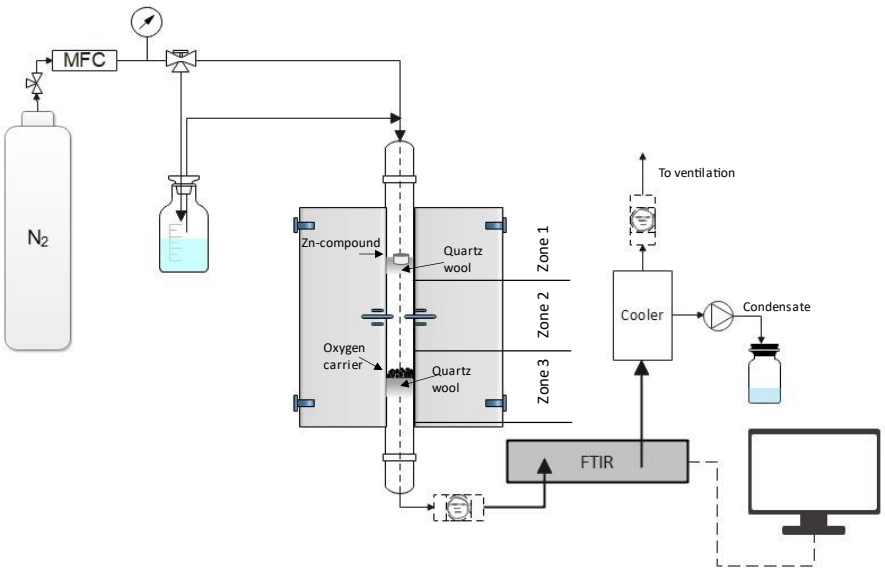

*Figure 11. Schematic overview of the experimental setup for investigating the interaction between gaseous zinc compounds and oxygen carriers (**Paper X**).*

6.2 Semi-Industrial-Scale Dual Fluidized Bed

Chalmers Power Central is a semi-commercial plant composed of a 10–12-MW_{th} circulating fluidized bed boiler and a 2–4-MW_{th} bubbling bed gasifier. The layout and sampling points of the system are presented in Figure 12. Bed material circulates between the gasifier (6) and boiler (2) via the particle distributor (4) and two loop seals (5) and (7). As the unit has a research purpose, the produced raw gas from the gasifier is not utilized, as it would be in a commercial plant, but is instead re-directed to the boiler where it is combusted. [76] The unit is connected to the district heating system, although the heat produced in the process is also used for heating the Chalmers campus. Wood chips are fed to the boiler (1), which operates at temperatures above 850°C. The bed material is heated in the boiler via an exothermic combusting process and circulated to the gasifier, where heat is released, enabling an endothermic gasification of the fuel. The flue gases from the boiler pass through a cyclone (3), to remove FA. A secondary cyclone (9) removes finer particles before entering the textile filter (10). Lime is added before the textile filter (10) to remove acidic gases such as SO_2 and HCl.

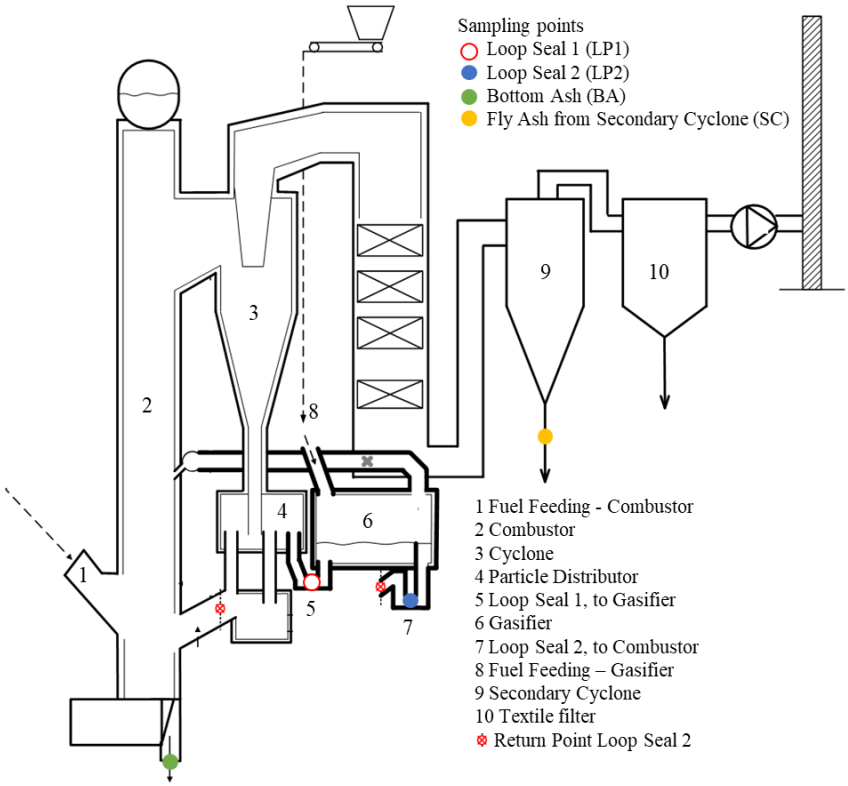

*Figure 12. Schematic of the Chalmers dual fluidized bed system (**Paper IV**). Sampling points are indicated in the figure. The red symbol represents the connection between loop seal 2 and the return to the boiler.*

During the experimental campaign, olivine sand was used as bed material. The gasifier was operated daily for 10 hours during weekdays for a period of 13 days, while the boiler was in continuous operation. Wood pellets were fed to the boiler and ASR was fed to the gasifier. The olivine bed was partially replaced, such that the addition and removal of bed material were made only in order to regulate the pressure in the boiler. Thus, ash accumulated in the bed during the 13 days of operation. The ash originated mainly from the ASR, as it contains 32%–47 wt.% ash, and wood pellets have a significantly lower ash content of <0.7 wt.%. ASR ash contains significant concentrations of metals, such as Fe, which means that the bed acquired OC properties during operation. This phenomenon has been further addressed by Pissot et al. [76].

6.3 Industrial-Scale Fluidized Bed Boilers

In this thesis, the BA and FA samples have been derived from two industrial units. The BA samples have been sieved to sizes <710 μm, to remove larger pieces, such as screws, hinges, nails, cables etc. The ash was, thereafter, magnetically separated twice. The magnetic separation was performed using a conveyor belt stretched across two horizontal cylinders. One cylinder constitutes an electric motor, while the other cylinder contains Rare Earth Roll (RER) magnets. The bed material is evenly fed onto the belt using a distributor. The non-magnetic material follows a parabolic path in the direction of the magnetic drum where it is collected in a bin, while the magnetic material follows the magnetic drum and is collected in a separate bin.

6.3.1 Kraftringen, Örtofta

The 115-MW_{th} CFB boiler at Örtofta, which is owned by the company Kraftringen, has been in operation since March 2014. The plant supplies heat to the local heating grid by burning biomass. A schematic of the plant is presented in Figure 13. During operation, approximately 60 tonnes of bed material are present in the system. Typically, silica sand with an average particle size of 0.25 mm is used as bed material, although in this case rock ilmenite was utilized (**Papers II** and **VIII**). During the OCAC campaign, the silica sand bed was successively replaced by ilmenite and the fuel consisted of recycled waste wood and wood chips. Bed samples were collected daily after the water-cooled bed ash extraction screw-feeders. Detailed information can be found elsewhere. [24]

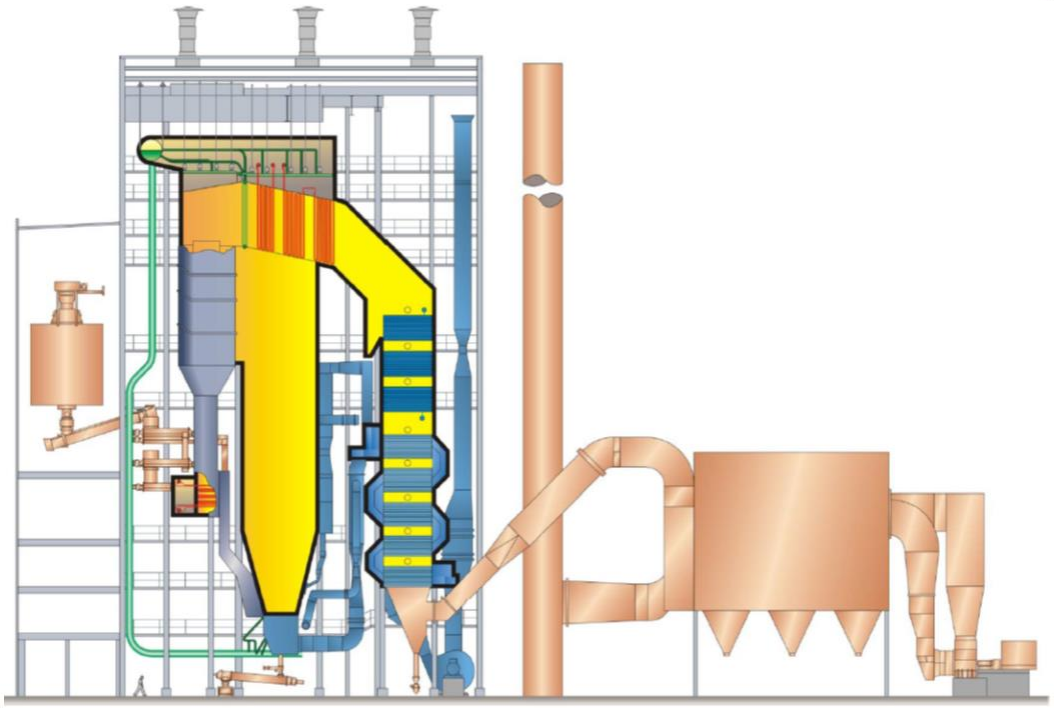

Figure 13. Schematic of the Kraftringen 115-MW_{th} CHP plant.

6.3.2 Händelöverket P14

The 75-MW_{th} CFB boiler in Norrköping has since November 2014 occasionally been operated with ilmenite (**Papers III** and **VI**). The plant provides heat to the local district heating network. Since November 2014, the boiler has occasionally been operated with ilmenite (**Papers III** and **VI**). A schematic of the Händelöverket P14 plant is presented in Figure 14, and more details are provided in the literature. [25] During the OCAC campaign, a mixture of rock ilmenite and silica sand was used as bed material. The fuel consisted of municipal solid waste and industrial waste. BA and FA samples were collected several times a day. Further details are presented in **Papers III** and **V**.

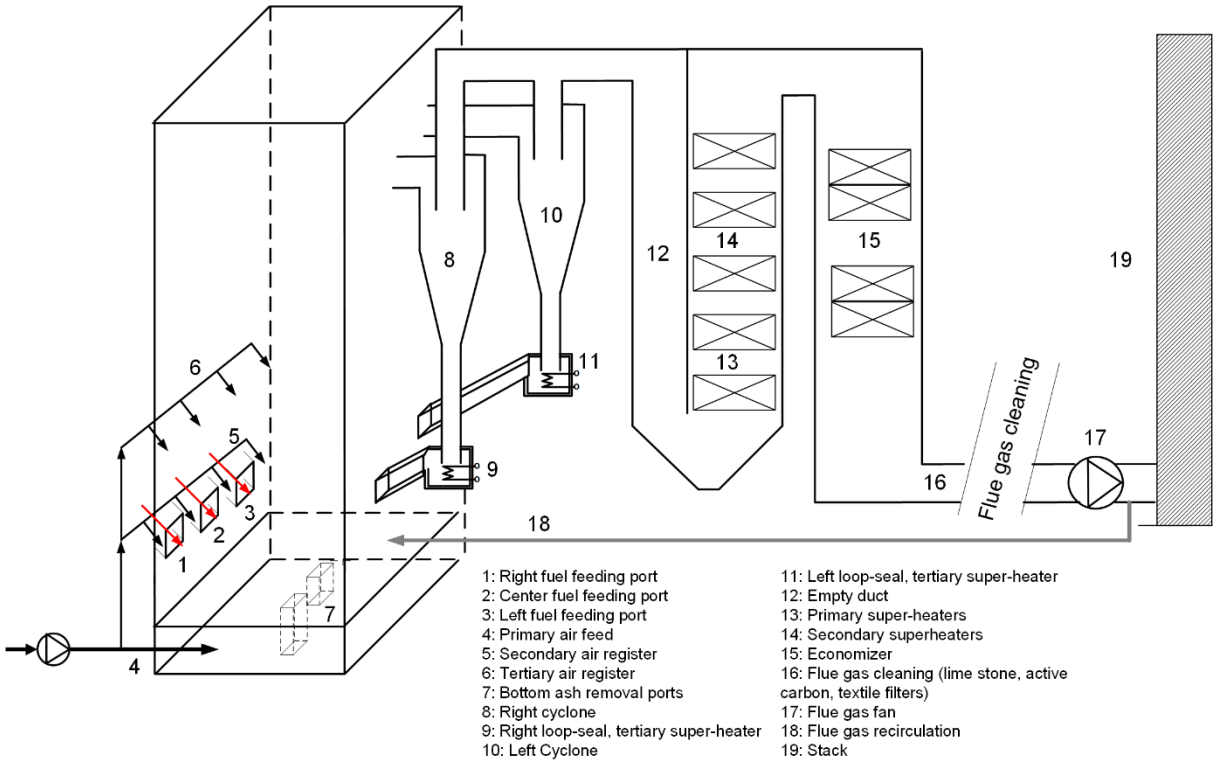

Figure 14. Schematic of the 75-MW_{th} Händelöverket P14 unit.[25]

7

Results and Discussion Part I

This part of the thesis presents the experimental and theoretical observations made regarding the interactions between the oxygen carriers and heavy metals. It begins by presenting the concentrations of heavy metals in the sampled ashes from OCAC. Thereafter, the identified crystalline phases in these ashes are compared with the phases predicted by TEC (Section 7.1). The subsequent sections delve into the chemical speciation of specific heavy metals, namely Zn, Cu and Pb (Sections 7.2–7.3). Each section focuses on one heavy metal and summarizes the observations made based on global TECs of the OCAC system, highlighting the influences of the oxygen partial pressure and temperature. It also provides an overview of the experimentally determined compounds, and lastly a list of heavy metal compounds relevant for chemical looping. Section 7.2 discusses the influence on the heavy metal speciation caused by other inorganic species, such as Si, S, Cl, K and Na. Section 7.6 focuses on the fates of the inorganic ash species, specifically in the context of CLC of solid fuels and compares both Mn-based and Fe-based OCs. Lastly, Section 7.7 summarizes the implications of the findings on the operation, recycling and environment.

Sampling from industrial boilers provides a unique opportunity to investigate the behaviors of OCs under realistic conditions in which complex fuels are utilized. The elemental analyses of selected BAs, utilizing various waste-derived fuels and OCs as bed materials, are summarized in Table 6. These samples were obtained from the commercial and semi-commercial units described in Section 6. Ilmenite was used in all experiments, with the exceptions being the experiments performed in the Chalmers unit when olivine was used for CLG, and two reference samples at Händelö and Örtofta, where sand constituted the bed material. Table 6 lists the bed type, fuel, conversion technology, and time with ilmenite feeding and magnetic fraction (when applicable). Before implementing ilmenite as bed material, the industrial boilers were operated with silica sand and, therefore, sand samples were obtained for reference. These samples were characterized by higher level of Si, and lower Fe and Ti concentrations. From mixed beds with both silica sand and ilmenite, an ilmenite-rich fraction was obtained by magnetic separation. Examples of the compositions of the magnetic accepted and magnetic rejected fractions obtained after 540 h of OCAC with MSW are presented in Table 6. The elemental analysis of the two ash fractions showed that the magnetic fraction was enriched in Fe and Ti, while the fraction rejected by the magnet was enriched in Si. During CLG of ASR, the BA consisted of olivine and the ASR, which has an ash content >30 wt.%. BA and FA samples were extracted after 13 days of operation, during which time there was almost no replacement of the bed

material. The ASR ashes were rich in metals (Table 1) and accumulated in the bed, yielding some oxygen-carrying capability.

Table 6. Elemental analysis of selected bottom ashes from different chemical looping applications.

Bed		Ilmenite	Sand*	Ilmenite	Sand	Ilmenite	Ilmenite	Ilmenite	Olivine
Fuel		RWW	RWW	MSW	MSW	MSW	MSW	MSW	ASR
Magnetic		-	-	Accept	Accept	Accept	Reject	Accept	n.a.
Application		OCAC	FBC	OCAC	FBC	OCAC	OCAC	OCAC	CLG
Magnetic fraction [wt.%]		70	25	26	9.6	19.6	19.6	41.6	-
Time with ilmenite feeding [h]		200	505*	100	0	550	550	893	ǂ
Unit	Paper(s)	**III, VIII, X**	**III**	**III**	**V×**	**V×**	**V×**	**V×**	**IV**
wt.% dry	Fe	19.0	2.1	16.2	11.0	22.5	1.3	23.3	7.7
	Ti	16.0	1.6	9.3	1.5	7.0	0.7	12.8	0.4
	Si	4.8	25.7	9.6	16.6	8.6	31.9	7.4	18.0
	Ca	10.8	8.2	9.0	15.6	13.0	9.6	10.8	7.3
	Mg	2.0	1.1	1.6	1.8	1.4	0.8	1.9	19.0
	Al	1.5	3.0	2.5	4.7	2.6	4.2	2.2	1.6
	Na	1.0	1.3	1.2	2.0	1.0	1.6	1.1	0.6
	K	1.8	4.3	0.5	0.9	0.4	1.1	0.4	1.8
	Mn	0.6	0.5	0.2	0.2	0.3	0.1	0.3	0.5
	S	0.7	0.2	0.9	2.7	1.3	0.7	1.4	0.2
mg/kg dry	Cr	883	203	677	2,050	2,590	299	1,040	650
	Pb	675	544	686	530	716	716	668	420
	Cu	810	702	3,180	2,390	6,310	6,020	5,210	3,400
	Zn	10,100	10,400	8,650	7,050	12,700	4,280	11,200	14,600

*200h after the start of silica sand feeding

× A time series available over 893h and a magnetic fraction in the range of 11.2–44.7 wt.%.

ǂ Sample obtained from the bottom of the boiler after 13 days of CLG with ASR

The variation in ash composition was reflective of both the bed material and fuel type. Calcium was the major ash component in all the samples, while the highest alkali concentrations were found in combination with silica sand. There were also some differences between the alkali metals, for example, the sodium concentration was higher than that of potassium in the MSW and ASR ashes, as compared to the BT and RWW. The zinc concentration was the TE with highest concentration and reached levels of around 1 wt.%. Comparing the magnetic accept and reject fractions of ilmenite from OCAC of MSW revealed an accumulation of Zn in the accepted fraction. Chromium was also concentrated in the MSW ashes, particularly in the magnetic accept fraction. Cu showed the lowest concentration in the RWW samples, while Pb was always present at around 600 mg/kg and was not influenced by the OC or the magnetic separation.

7.1 Phase Correlation – Crystalline Phases and Global TEC

A summary of the phases identified by XRD and predicted by global TEC is presented in Table 7. The magnetic accept ash fraction correlates with the TEC obtained for an ilmenite bed, while the magnetic reject fraction correlates with the TEC for a silica sand bed, as shown in **Paper V.** It should also be noted that minor and trace phases can be difficult to validate due to limitations associated with the characterization method. Furthermore, amorphous phases cannot be studied in detail, but they can indirectly be seen as a strongly enhanced background in the XRD patterns. As the OC takes up a large part of the bed, the major phases are related to the OC composition, while the intensity of the ash-induced phases is lower. Nevertheless, the table shows that the predicted and observed phases are well-aligned.

Table 7. Comparison of the phases predicted by global TECs and the crystalline phases experimentally observed by XRD (marked with ✓).

Oxygen Carrier	Ilmenite	Ilmenite	Ilmenite	Olivine
Application	OCAC	OCAC	OCAC	CLG
Fuel	RWW	MSW	MSW	ASR
Magnetic	Accept	Accept	Reject	-
Paper	**III**	**V**	**V**	**IV**
Pseudobrookite – Fe_2TiO_5	✓	✓		
Rutile – TiO_2	TEC, ✓	TEC, ✓		
Hematite – Fe_2O_3	TEC	TEC		
Perovskite – $Ca(Fe,Ti)O_3$	TEC, ✓	TEC, ✓		
Feldspar – $(Na,K)AlSi_3O_8$	TEC, ✓	TEC, ✓	TEC, ✓	TEC, ✓
Clinopyroxene – $Ca(Mg,Fe)Si_2O_6$	TEC, ✓	TEC, ✓	TEC, ✓	TEC, ✓
Spinel – $(Fe,Mg,Zn)_3O_4$	TEC, ✓	TEC, ✓		TEC, ✓
Nepheline – $NaAlSiO_4$	✓	✓		TEC
Anhydrite – $CaSO_4$		TEC, ✓	TEC, ✓	
Olivine – $(Mg,Ca,Fe)MgSiO_4$				TEC, ✓
Quartz – SiO_2	✓	✓	✓	✓
Melilite – $(Ca,Na)_2(Mg,Fe,Al)_3Si_2O_7$		✓	✓	TEC, ✓
Wollastonite – $CaSiO_3$			TEC, ✓	
Slag-liq	TEC	TEC	TEC	TEC

This shows that the global TECs are valuable in providing an overview of the expected oxidized or reduced state of the OC, as well as information on the possible interactions with the ash components. As the major crystalline phases are largely in line with the predicted thermodynamic phases, it is also expected that the calculations can provide further insights in the phase distribution of the TEs.

7.2 Chemical Speciation of Zinc

It is likely that local variations in the boiler related to variations in the temperature and oxygen partial pressure influence heavy metal speciation. Therefore, the influences of the oxygen partial pressure and temperature will be presented in more detail in the coming sections. First, figures are shown based on the TECs for the fuel-bed material combinations: ASR-olivine, MSW-ilmenite, MSW-silica sand, and RWW-ilmenite. Then, the experimental observations are presented and, lastly, the predicted phases are correlated with the experimental observations. Although it was not possible to validate the predicted gaseous phases, it is expected that the expanded databases, which include the gaseous components $Zn(OH)_2$, ZnOH, ZnC_2H_6, ZnH, ZnO, and ZnCl will contribute to describing this system.

The expected chemical speciations of Zn for different fuels and beds, as determined by TECs, are presented in Figure 15. The reader is referred to **Papers III–V** for details. For all the bed materials under oxidizing conditions, the most stable gaseous component is $ZnCl_2$. However, Zn is primarily found in the solid phase as a spinel $(Fe, Zn, Cr, Mg)_3O_4$, which is observed to be stable over a wide range of reduction potentials. The major spinel constituent up to the reduction potential of $10^{-3.9}$ is $ZnFe_2O_4$, after which $ZnCr_2O_4$ predominates. Zn-silicates (willemite and melilite) are also stable under these conditions. For ilmenite and sand as bed materials, a further increase in the reduction potential results in more Zn entering the gaseous phase as Zn(g). For olivine, however, an increase in the reduction potential leads to an increase in olivine $MgZnSiO_4$ and melilite $Ca_2ZnSi_2O_7$.

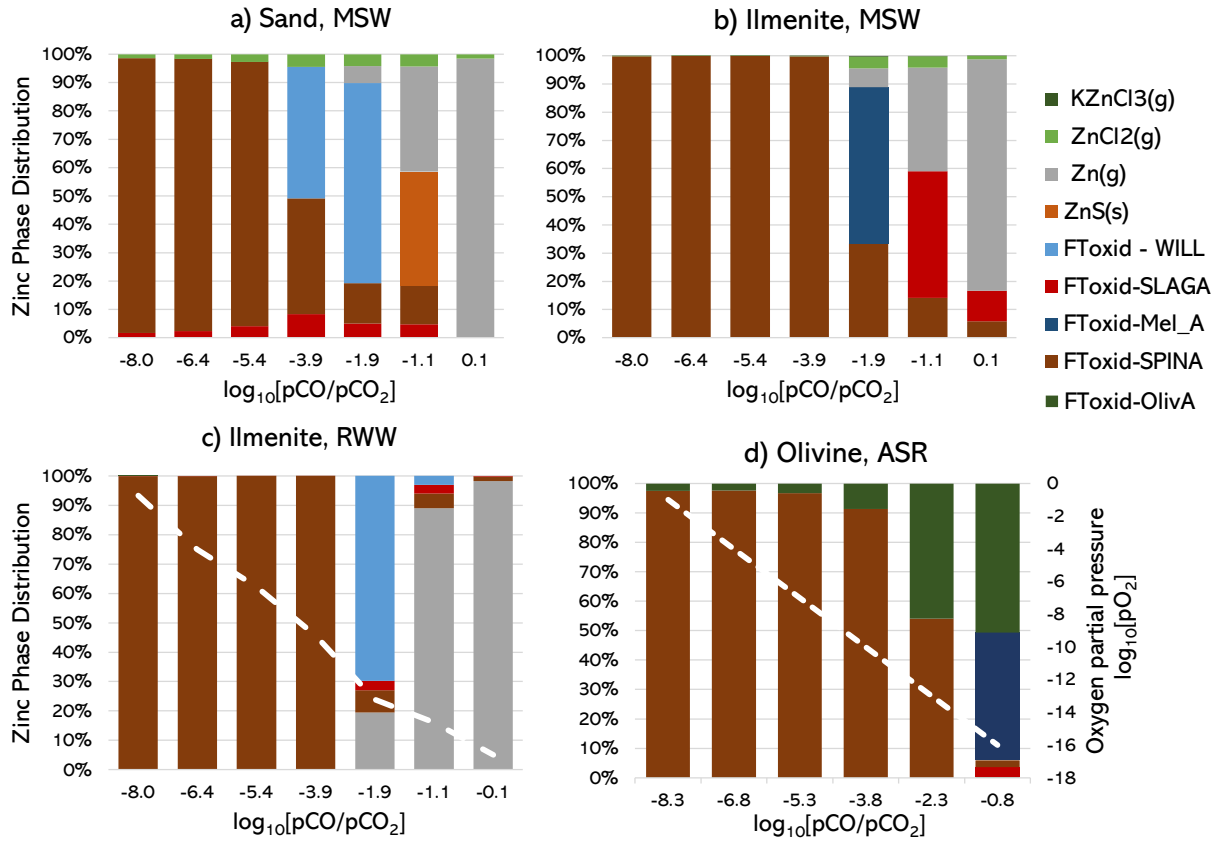

Figure 15. Chemical speciation of Zn and the influence of the reduction potential obtained by global TECs at 850°C and 1 atm. Thermochemical conversion of MSW was conducted with: a) silica sand; and b) ilmenite. c) Conversion of RWW was conducted with ilmenite, and d) conversion of ASR was carried out with olivine (830°C). The secondary y-axis relates to the reduction potential to the oxygen partial pressure, displayed as a white dashed line.

7.2.1 Influence of Temperature

Temperature variations in the range of 700°–1,100°C and oxidizing conditions were investigated in **Paper V** for OCAC of MSW utilizing ilmenite, silica sand or a mixture of the two. The results uncover only a weak influence on the Zn phase distribution. At temperatures above 950°C and 1000°C for silica sand and ilmenite, respectively, a slag phase forms, which dissolves the ZnO. For the ilmenite bed, the slag forms to a lesser extent compared with the silica sand bed, and the spinel is stable even at 1,100°C.

7.2.2 Zinc Distribution and Chemical States

The distributions of the heavy metals in the ash samples were investigated following the procedure described in Section 4. The chemical distribution was studied with respect to the OC surface, as well as the cross-section. Representative ilmenite surface and cross-sectional micrographs are illustrated in Figure 16.

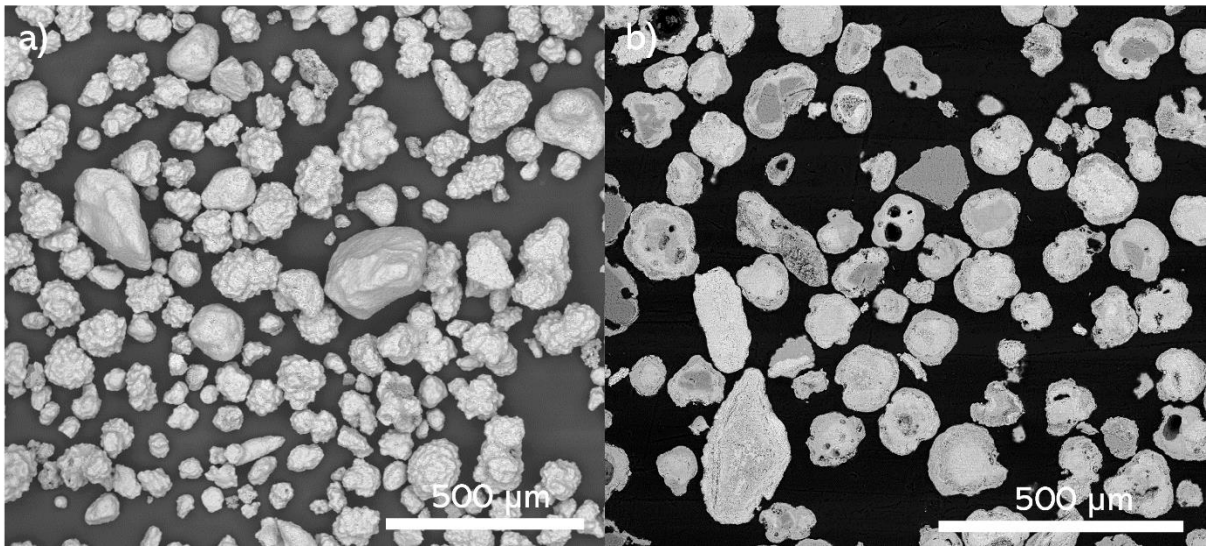

Figure 16. a) Surface micrograph of ilmenite derived from OCAC of RWW. b) Cross-sectional micrograph of the same ilmenite fraction.

From the chemical maps of the particle surfaces, Zn was found to cover the ilmenite (**Paper III**). Examination of the particle cross-section revealed that Zn accumulated in the ash layer along with Fe (**Paper V**). The chemical states of Zn in the FA, on the particle surface, and in the particle cross-section were further studied by XPS. A summary of the possible components in the BA and FA is presented in Table 8. The FA contained a combination of Zn-chlorides and some combined metal oxides. At the surfaces of the OC particles, the compound that is most commonly encountered is $ZnFe_2O_4$, although the presence of silicates and aluminates could also be observed. The ferrite observed in the particle cross-section in Table 8, likely originates from the incorporation of Zn into the ash layer.

Table 8. Summary of Zn-bearing components identified with XPS. The cross-sectional samples of ilmenite obtained from OCAC of MSW were studied by molding the particles in epoxy.

Technology	**OCAC**				**CLG**	
Fuel	MSW		RWW		ASR	
Bed material	Ilmenite		Ilmenite	Sand	Olivine	
Ash type	BA	FA	BA	BA	BA	FA
Surface	$ZnFe_2O_4$ Zn_2SiO_4	$ZnCl_2$ $ZnAl_2O_4$	$ZnFe_2O_4$	$ZnFe_2O_4$	$ZnFe_2O_4$ $ZnAl_2O_4$	$ZnFe_2O_4$ $ZnCl_2$
Cross-section	$ZnFe_2O_4$					

7.2.2.1 Interaction between Ilmenite and Zinc Chloride

An experimental investigation was conducted to obtain a better understanding of the reactions between Zn-bearing compounds and ilmenite (**Paper X**). The interactions were studied in a vertical tube reactor, as shown in Figure 11, using synthetic, fresh and used rock ilmenite with two gaseous Zn compounds: metallic Zn and $ZnCl_2$. The influence of activation and the presence of an ash layer were investigated. The main findings for the fresh and used ilmenite will be presented here. The latter was extracted after 200 h of OCAC operation with RWW and wood chips.

The results of the study indicate that the reaction between $ZnCl_2$ and ilmenite in the N_2 atmosphere is low, but that the presence of steam can promote the interaction. It is likely that steam promoted the oxidation of $ZnCl_2$ to ZnO, which in its turn reacted with ilmenite. The results also indicate that the Fe-rich layer formed during the activation of ilmenite enhanced the interaction with $ZnCl_2$ (see the example in Figure 17).

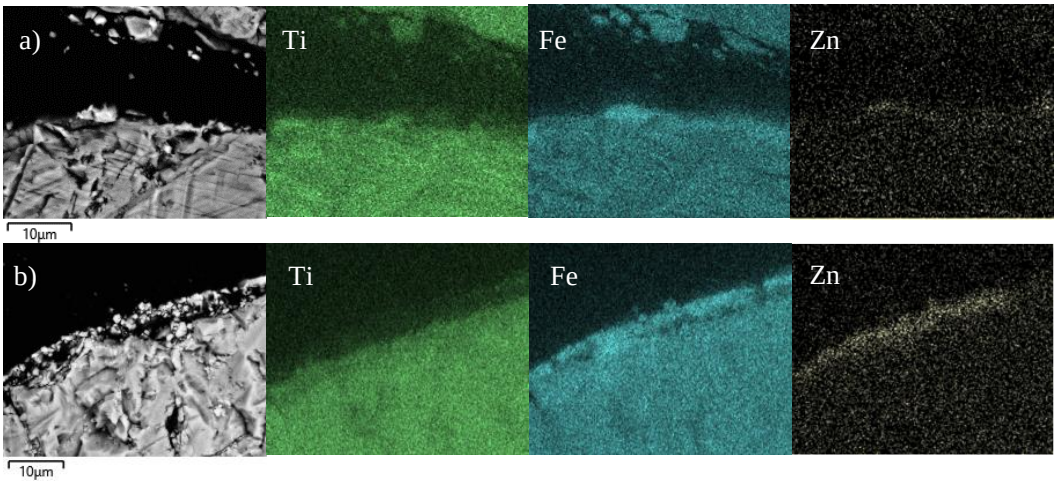

Figure 17. Cross-sectional micrographs of ilmenite (Figure a) after operation in 2 vol% H_2O in N_2, with $ZnCl_2$ and activated ilmenite (Figure b), along with chemical maps of Ti, Fe, and Zn.

The used ilmenite sample contained ash-forming elements such as calcium and sulfur, but also Zn before the experiments. The total Zn-concentration in the sample was measured by ICP-OES, before and after experiments. It was found that the concentration increased from 1.0 to 2.6 wt. %. The chemical maps of the cross-section of the particles after experiments showed that Zn was found in combination with Fe in the outer particle ash layer, but also inside particles which were not completely covered by other ash elements. These observations indicate that other ash components could restrict contact with Fe, potentially stopping or slowing down the rate of interaction.

7.2.2.2 Interaction between Ilmenite and Metallic Zinc

Studying the chemical maps of the cross-section after experiments with metallic Zn and fresh ilmenite showed a clear interaction between the two. As opposed to experiments with $ZnCl_2$, a deeper interaction depth was observed for metallic Zn. The reaction between ilmenite and metallic Zn resulted in the formation of $ZnFe_2O_4$, and some ZnO, both of which were identified by XRD. The interaction was found to be more prominent after ilmenite was activated. The Fe-rich layer formed after the activation of ilmenite, in combination with increased porosity and cracking, is likely the reason for the enhanced interaction .The crystalline phases $ZnFe_2O_4$ and ZnO were present in both the fresh and used ilmenite.

Following the experiments with used ilmenite, the Zn-concentration increased from 1.0 to 11.3 wt.%, as determined by ICP-OES . An example of the chemical distribution of Zn over the ilmenite cross-section is presented in Figure 18. The figure shows two particles that are distinct in terms of composition. For example, the chemical maps show that the left particle has high contents of Ca and S, while the right particle contains lower levels of these elements. Looking at the chemical map of Zn, the concentrations are higher on the surface of the right particle. This resembles the case with fresh ilmenite showing that the formation of $ZnFe_2O_4$ can also occur in ilmenite with an ash layer, where Fe is accessible.

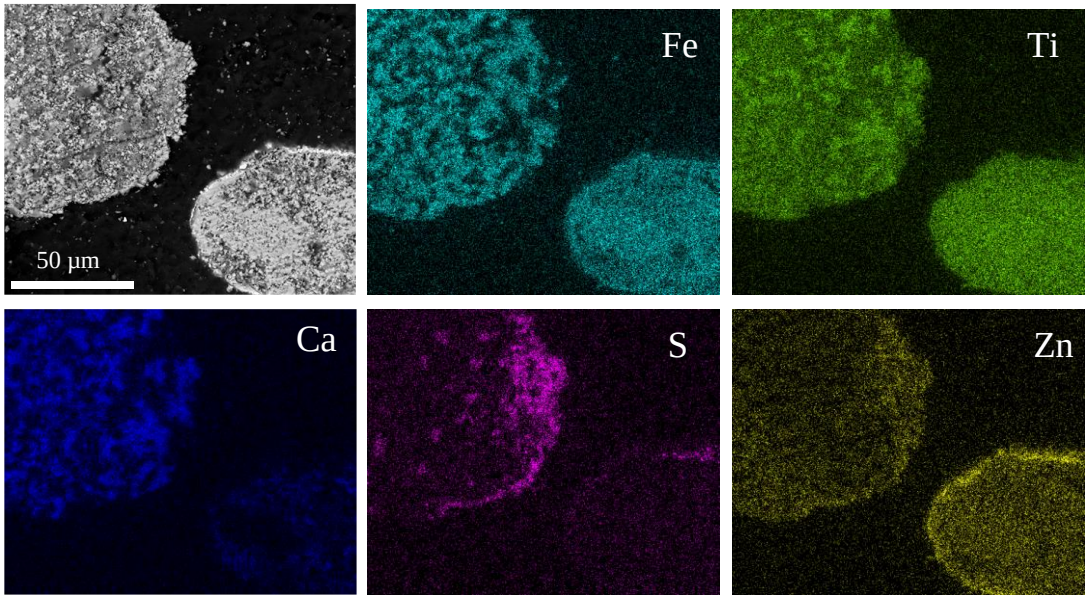

Figure 18. Micrographs and chemical maps of cross-sections of used ilmenite after exposure to metallic Zn. Chemical maps of Fe, Ti, and the ash elements Ca, S, and Zn. Before the exposures, the ilmenite was utilized in OCAC of RWW, from which the ash layer was obtained.

However, it is also likely that the ash could prevent direct contact between Fe and Zn. For example, particles with an ash layer containing $CaSO_4$ promote the production of ZnS. The formation of ZnS was observed experimentally, in the form of micrometer-sized crystals. A surface micrograph showing the area of interest is presented in Figure 19. ZnS was also identified by XRD. Consequently, it is likely that Zn undergoes a series of reactions depending on the surface composition of the ilmenite particle and the ash layer.

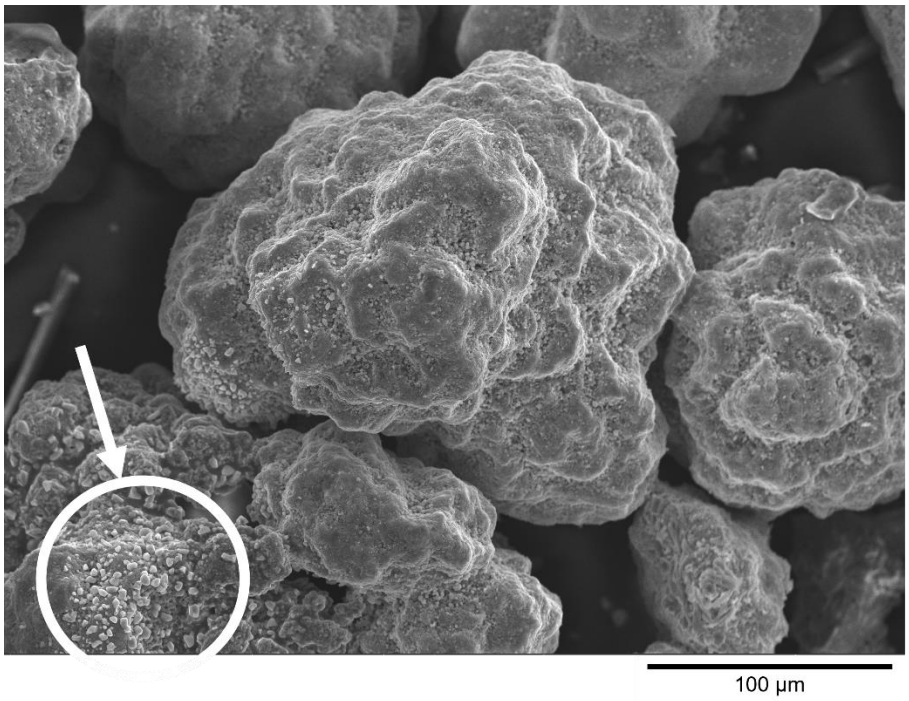

Figure 19. Surface micrograph (20 kV, SE-detector) of used ilmenite after experiments with metallic zinc. The region indicating the occurrence of zinc sulfide (ZnS) is highlighted.

7.2.3 Overview of Zinc Compounds in Chemical Looping

The previous section provided an experimental and theoretical overview of the stable Zn compounds in chemical looping processes. Comparing the phases predicted by TECs and experimental observations, it is evident that the thermodynamic data for Zn-bearing compounds are in accordance with the experimental observations. A summary of the relevant Zn-bearing compounds and descriptions of the conditions under which they form are presented in Table 9.

Table 9. Summary of relevant Zn-bearing compounds in chemical looping processes and the conditions under which they form.

Phase	Compound	pO_2 at 850°C [atm]	Conditions
Spinel	$ZnFe_2O_4$	$>10^{-11}$	Fe-based OCs Metal-rich fuel
Spinel	$ZnCr_2O_4$	$<10^{-11}$	Metal-rich fuel
Willemite	Zn_2SiO_4	$\sim10^{-13}$	Si-rich fuel or bed
Wurtzite	ZnS	$<10^{-10}$	S-rich fuel
Slag	ZnS	$<10^{-14}$	S-rich fuel
Slag	ZnO	$>10^{-14}$	Higher temperatures Si-rich fuel or bed
Gaseous	$ZnCl_{2\ (g)}$	$>10^{-12}$	Cl-rich fuel Higher temperatures Si-rich fuel or bed
Gaseous	$Zn(OH)_{2\ (g)}$	$>10^{-16}$	Cl-lean fuel
Gaseous	$ZnOH_{(g)}$	$<10^{-16}$	Cl-lean fuel
Gaseous	$Zn_{\ (g)}$	$<10^{-12}$	Higher temperatures

7.3 Chemical Speciation of Copper

The expected chemical speciations of Cu for different fuels and beds, as determined by TECs, are presented in Figure 20. The user-defined databases included the solid compounds $CuAl_2O_4$, $Cu_2Al_2O_4$, $CuCr_2O_4$ and Cu_2PbO_2, although these were not deemed to be stable in the global calculations. Under oxidizing conditions, the stability of Cu-oxides and Cu-ferrites is high, along with gaseous CuCl. For an ilmenite bed (with RWW) and silica sand bed, CuO is stable along with CuCl. At reduction potentials above $10^{-3.9}$, Cu_2S becomes stable, as does Cu_3As for RWW. The chemical speciation of Cu varies substantially, and the ferrite is reduced stepwise from $CuFe_2O_4$ to Cu for a reduction potential of 10^{-8} to $10^{-3.9}$ or for a reduction of the oxygen partial pressures (pO_2) from 21% to 10^{-11} atm.

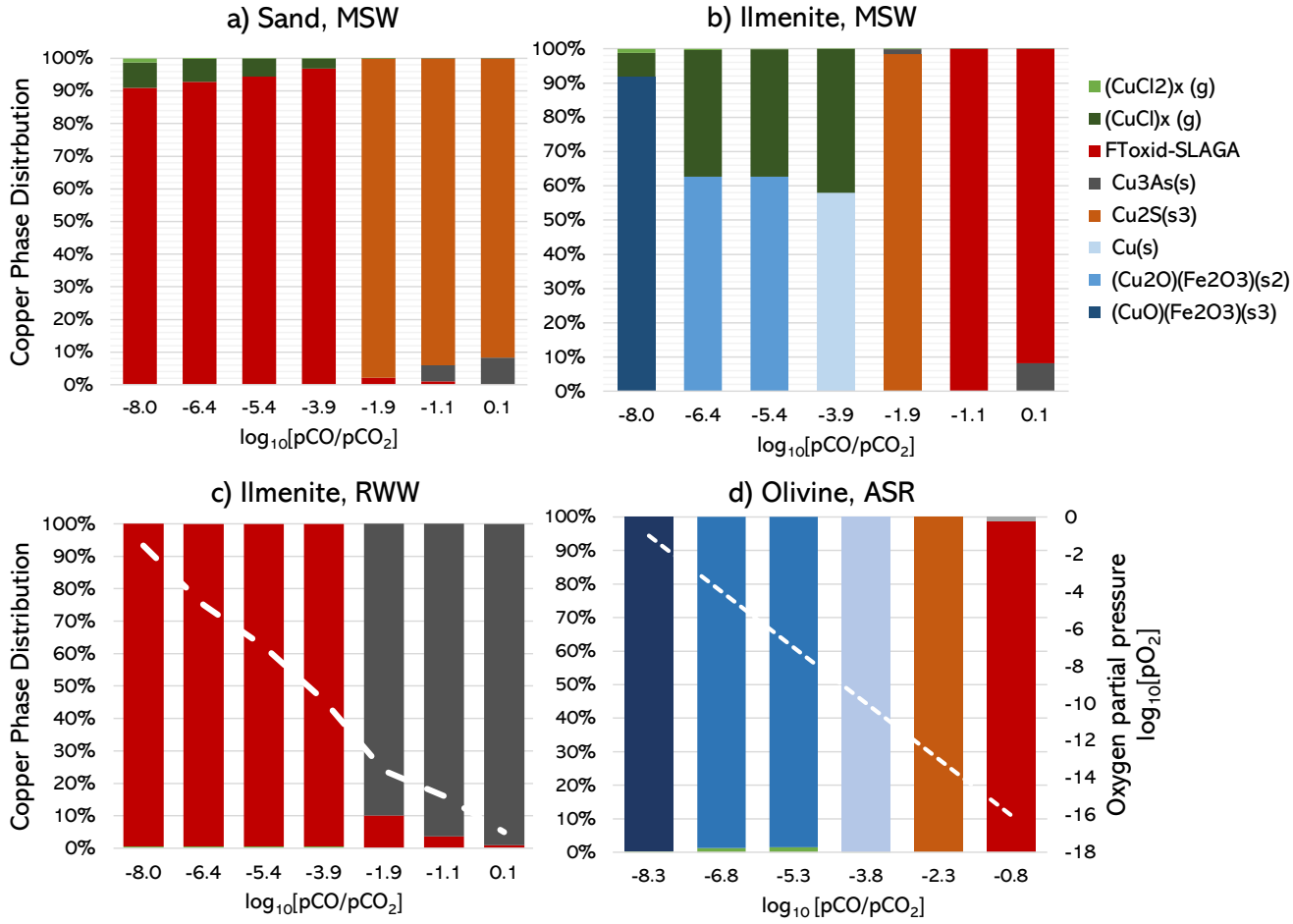

Figure 20. Chemical speciation of Cu and the influence of the reduction potential obtained by global TECs at 850°C and 1 atm. Thermochemical conversion of MSW: a) with silica sand; and b) with ilmenite. c) Thermochemical conversion of RWW with ilmenite, and d) thermochemical conversion of ASR with olivine (830°C). The secondary y-axis relates to the reduction potential to the oxygen partial pressure, displayed as a white dashed line.

7.3.1 Influence of Temperature

Compared to Zn, Cu is more heavily influenced by temperature. In a silica sand bed at temperatures <850°C, more than 70% of the Cu is found in the gas phase as CuCl. At temperatures >850°C, slag is formed, and the majority of the Cu is found in this phase as CuO. For ilmenite, however, the ferrite $CuFe_2O_4$ is stable up to 950°C, along with some CuCl. Above 850°C, Cu is found in the form of CuO in the slag.

7.3.2 Copper Distribution and Chemical States

Cu was difficult to observe when studying the chemical maps of the particle surfaces of ilmenite obtained from OCAC of RWW. This is likely due to the low Cu content of the fuel mixture. On the other hand, ilmenite utilized in OCAC of MSW showed the highest concentration of Cu at the particle surface and in the cross-section. It was, for example, observed with higher intensities at distinctive points on the particle surface (**Paper III**). Furthermore, studying particles over a period of 38 days (**Paper V**) showed enrichment of Cu in the particle cross-section. A micrograph of the cross-section of an ilmenite particle from OCAC of MSW is presented in Figure 21. Chemical maps of Fe, Ti, and the inorganic ash elements Ca, Zn, Cu, and S are shown in the figure. The small bright spots on the inside of the ilmenite particle show that Cu is present inside the particles.

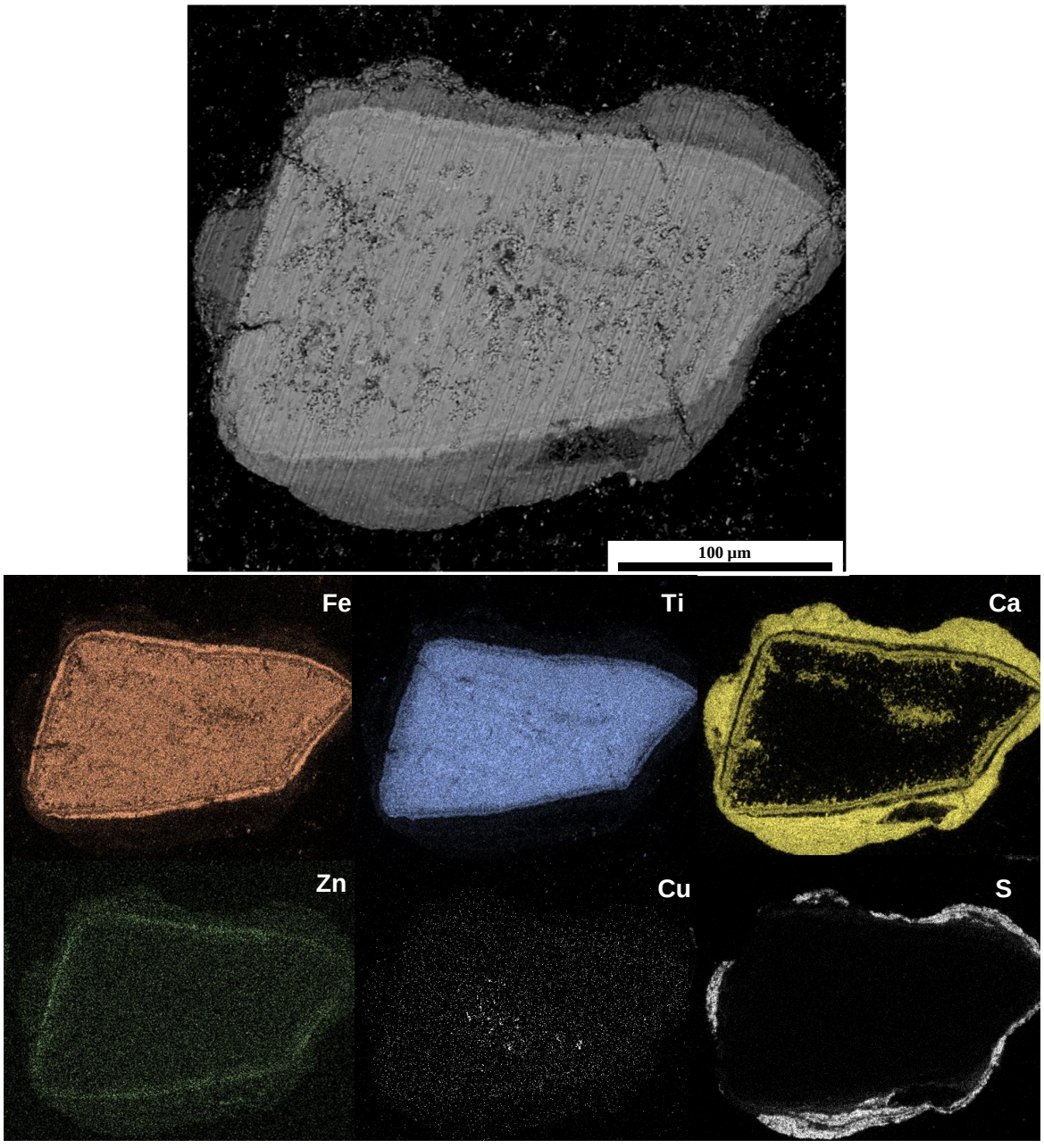

Figure 21. Cross-sectional micrograph of ilmenite obtained from OCAC of MSW, along with chemical maps of Fe, Ti, and the inorganic species Ca, Zn, Cu, and S.

The chemical states of Cu in the FA, on the particle surface, and in the particle cross-section were further studied by XPS. A summary of the possible components in the BA and FA is presented in Table 10. The FA contained a combination of Cu-chlorides and -ferrites. At the surface of the OC particles, the most commonly found compound was $CuFe_2O_4$. The Cu concentration was amongst the lowest in the ash obtained from OCAC of RWW.

Table 10. Summary of Cu-containing components identified with XPS. The cross-section of ilmenite obtained from OCAC of MSW was studied by molding the particles in epoxy.

Technology	**OCAC**				**CLG**	
Fuel	MSW		RWW		ASR	
Bed material	Ilmenite		Ilmenite	Sand	Olivine	
Ash type	BA	FA	BA	BA	BA	FA
Surface	$CuFe_2O_4$	$CuFe_2O_4$ $CuCl_2$	-	-	$CuFe_2O_4$ $CuSO_4$	$CuFe_2O_4$ $CuCl_2$
Cross-section	$Cu_2Fe_2O_4$					

7.3.3 Overview of Cu Compounds in Chemical Looping

Comparing the theoretical and experimental outcomes, it is evident that the results overlap. The experimentally observed components accord well with the phases predicted under oxidizing conditions. A summary of the relevant Cu-bearing compounds in chemical looping processes, and descriptions of the conditions under which they form are presented in Table 11.

Table 11. Summary of relevant Cu-bearing compounds in chemical looping and the conditions under which they form.

Phase	Compound	pO_2 at 850°C [atm]	Conditions
(s)	$CuFe_2O_4$	$>10^{-4}$	Fe-based OC Metal-rich fuel
(s)	$Cu_2Fe_2O_4$	$10^{-7}<pO_2<10^{-4}$	Fe-based OC Fe-rich fuel
(s)	$CuSO_4$	$>10^{-7.4}$	S-rich fuel
(s)	Cu_2S	$<10^{-7.4}$	S-rich fuel
(s)	Cu	$\sim10^{-10}$	Si-lean fuel or bed
Slag	Cu_2S	$<10^{-10}$	S-rich fuel
Slag	Cu_2O	$>10^{-10}$	Si-rich fuel or bed
Gaseous	CuCl	$>10^{-10}$	Cl-rich fuel
Gaseous	$CuCl_2$	$>10^{-2}$	Cl-rich fuel

7.4 Chemical Speciation of Lead

The influence of the reduction potential on the phase distribution of Pb is shown in Figure 22. The expanded database HSCA included the solid compounds $Pb_5Si_3O_{11}$, PbS_2SiO_4, $Pb(OH)_2$, Cu_2PbO_2, $K_2Pb(SO_4)_2$, $Pb_{12}O_{17}$, $Pb_{12}O_{19}$, Pb_3CO_5, Pb_2O_3, PbS_2O_3, PbS_3O_6, PbV_2O_6, $Pb_2V_2O_7$, $Pb_3V_2O_8$, PbS_2SiO_4, $PbSiO_4$, $Pb_5Si_3O_{11}$, Ca_2PbO_4, $K_2Pb(SO_4)_2$, and $Pb_3(AsO_4)_2$, as well as the gaseous compounds Pb_2S_2, PbS_2, and PbO_2. With HSCA, the global TECs largely predicted the stability of $PbSiO_4$. As this was not deemed reliable due to constraints on the thermodynamic data, where the component was valid up to 398 K, $PbSiO_4$ was removed from the calculations; the resulting phase distribution is presented in Figure 22. It can be observed that $PbCl_2$ is the major species under oxidizing conditions for all cases, with the exception of RWW. For RWW and silica sand with MSW, most of the Pb was associated with the slag phase up to the reduction potential of -3.9. Regardless of the fuel and bed material type, with increasing reduction potential the propensity to form PbS(g) followed by Pb(g), increased. In contrast to the case with sand or ilmenite, the stability levels of melilite and slag were higher for ASR and olivine.

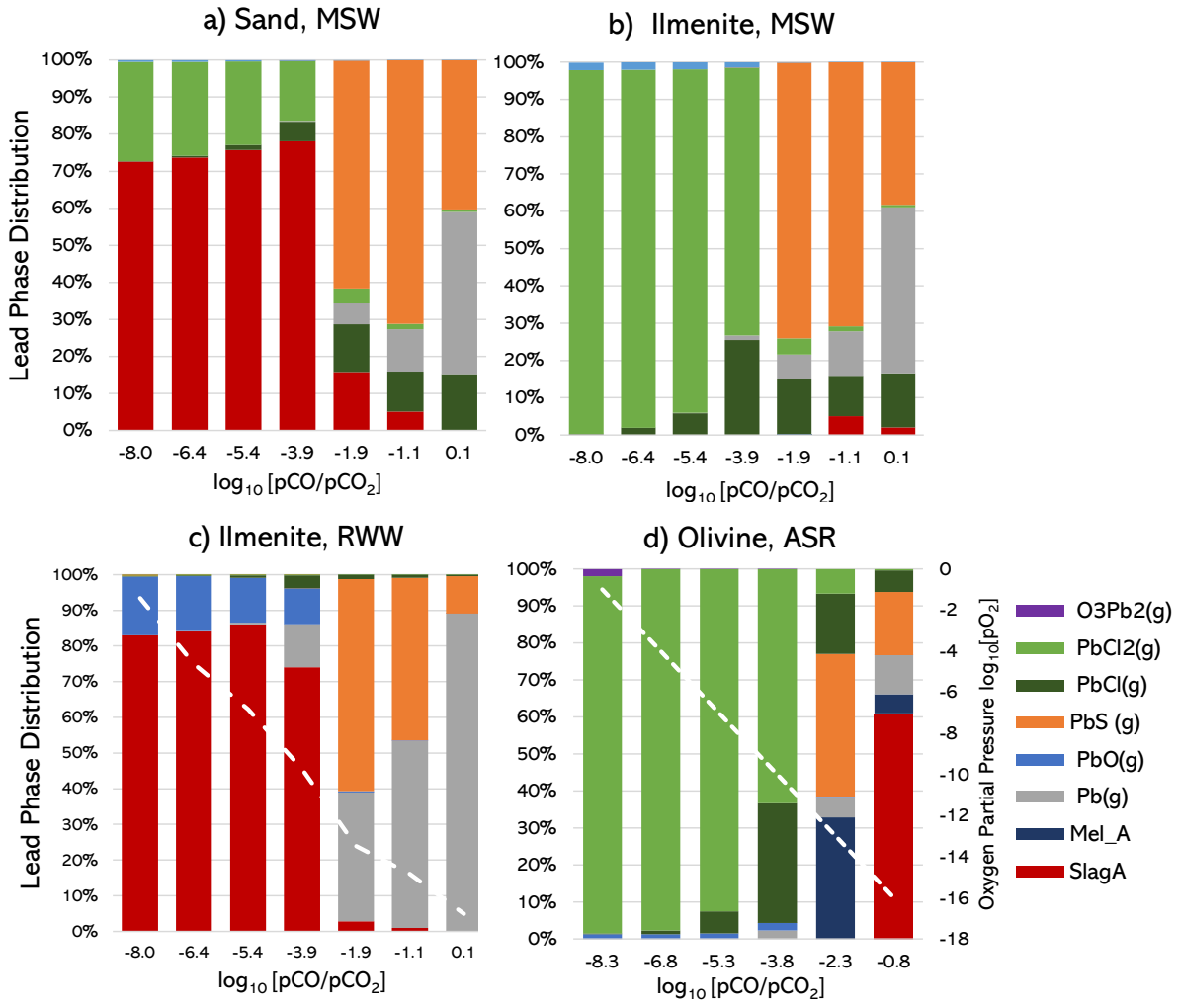

Figure 22. Chemical speciation of Pb and the influence of the reduction potential obtained by global TECs at 850°C and 1 atm. Thermochemical conversion of MSW: a) with silica sand; and b) with ilmenite. c) Thermochemical conversion of RWW with ilmenite, and d) thermochemical conversion of ASR with olivine (830°C). The secondary y-axis indicates the reduction potential to the oxygen partial pressure, displayed as a white dashed line.

7.4.1 Influence of Temperature

Pb is largely affected by the slag phase that forms at temperatures above 800°C (silica sand) and 950°C (ilmenite). Above these temperatures, PbO becomes associated with the slag phase. In an ilmenite bed, a combination of PbO and $PbCl_2$ is present in the gas phase, while a smaller share of $PbCl_2$ is present in the case with a silica sand bed.

7.4.2 Lead Distribution and Chemical States

Pb belongs to the elements that are present at the lowest concentrations in the BA, but at the highest concentrations in the FAs. Pb is more difficult to observe with SEM in the BA fractions due to its low concentrations. Despite the low concentration in the BA, it was possible to study the particle surfaces by XPS, which detected around 0.1 at% Pb. A summary of the observations is presented in Table 12. The main compound encountered in the FAs was $PbCl_2$. In ilmenite, both Pb-titanates and Pb-silicates were observed on the particle surfaces. Analyzing the particle cross-section did not reveal significant evidence of accumulation, although for a few particles, low concentrations of Pb (0.1 at%) were detected in the form of Pb-titanates.

Table 12. Summary of Pb-containing components identified with XPS. The cross-section of ilmenite obtained from OCAC of MSW was studied by molding the particles in epoxy.

Technology	**OCAC**				**CLG**	
Fuel	MSW		RWW		ASR	
Bed material	Ilmenite		Ilmenite	Sand	Olivine	
Ash type	BA	FA	BA	BA	BA	FA
Surface	$PbCl_2$ $PbSiO_3$ $PbTiO_3$	$PbCl_2$	$PbTiO_3$	$PbSiO_3$	$PbSiO_3$	$PbCl_2$ PbO
Cross-section	$PbTiO_3$					

7.4.3 Overview of Pb Compounds in Chemical Looping

Based on experiments and thermodynamic analyses, a summary of the relevant Pb-bearing compounds in chemical looping processes, and descriptions of the conditions under which they form are presented in Table 13.

Table 13. Summary of relevant Pb-bearing compounds in chemical looping and the conditions under which they form.

Phase	Compound	pO_2 at 850°C [atm]	Conditions
(s)	$PbTiO_3$	$>10^{-11}$	< 1000°C Ilmenite Ti-rich fuel
(s)	$PbSiO_3$	$>10^{-13}$	<750°C Si-rich fuel or bed
Slag	PbO	$>10^{-10}$	Si-rich fuel or bed
Melilite	$(Ca,Pb)_2(Mg, Fe, Zn)Si_2O_7$	$<10^{-13}$	Si-rich fuel or bed
Gaseous	$PbCl_2$	$>10^{-10}$	Cl-rich fuel Si-lean fuel Ilmenite
Gaseous	PbCl	$<10^{-10}$	Cl-rich fuel
Gaseous	Pb	$<10^{-10}$	S-lean fuel
Gaseous	PbS	$<10^{-10}$	S-rich fuel
Gaseous	PbO	$>10^{-10}$	Cl-lean fuel

7.5 Competing Balances between Inorganic Species

As evident from the figures and tables above, the phase distribution of the trace elements is affected not only by the main components in the OCs, but also by other ash species. For example, the solid phase distribution of Pb in Figure 22 shows the influence of fuel composition. The phase distributions and fractions of chlorides, sulfates, silicates and melts largely differ depending on the concentrations of the inorganic ash species. Table 13 shows that Si influences the chemical speciation of lead and will increase the stability of silica-based compounds or melts which dissolve the metals, while Figure 15 shows that larger fractions of $ZnCl_2$ form in a silica sand. This influence will be discussed further below with respect to the species of S, Cl, Ca, silica sand, and alkali metals. The influence of each species, under oxidizing and reducing conditions, based on the results obtained from TECs will be elaborated upon below.

Silica sand. Increasing the amount of Si in the bed will allow more alkali silicates to form. In oxidizing atmospheres, combined with high temperatures, these alkali silicates tend to melt, leading to high levels of slag. This slag can also dissolve heavy metals, as observed in Figures 15, 19, and 21. Under reducing conditions, the risk of melts is lower, and the silicates feldspar, nepheline, and leucite instead become stable.

Chlorine. For Cl-rich fuels, the HCl concentration increases in the gas phase along with some alkali chloride and metal chlorides, mainly $PbCl_2$ and $(CuCl)_x$. As a consequence, the amount of slag decreases. Chlorine affects metal volatility, specifically that of Cu and Pb, while the influence on Zn was not as evident (see **Paper V** for details). The formation of gaseous metal chlorides increases their mobility, which could aid the interaction with the bed material by

sticking to the surface or diffusing through pores and cracks in the particles. The release of these metals to the gas phase could also increase the risk of corrosion and fouling on heat transfer surfaces.

Sulfur. S-rich fuels cause an increase in the amount of SO_2 or H_2S in the gas phase under oxidizing and reducing conditions, respectively. Under reducing conditions, an increase in heavy metal sulfides, such as $Cu_2S(s)$, $ZnS(s)$, and $PbS(g)$, can be observed by TECs. The formation of ZnS has also been observed experimentally (**Paper X**) at the ilmenite particle surface, as presented in Figure 23.

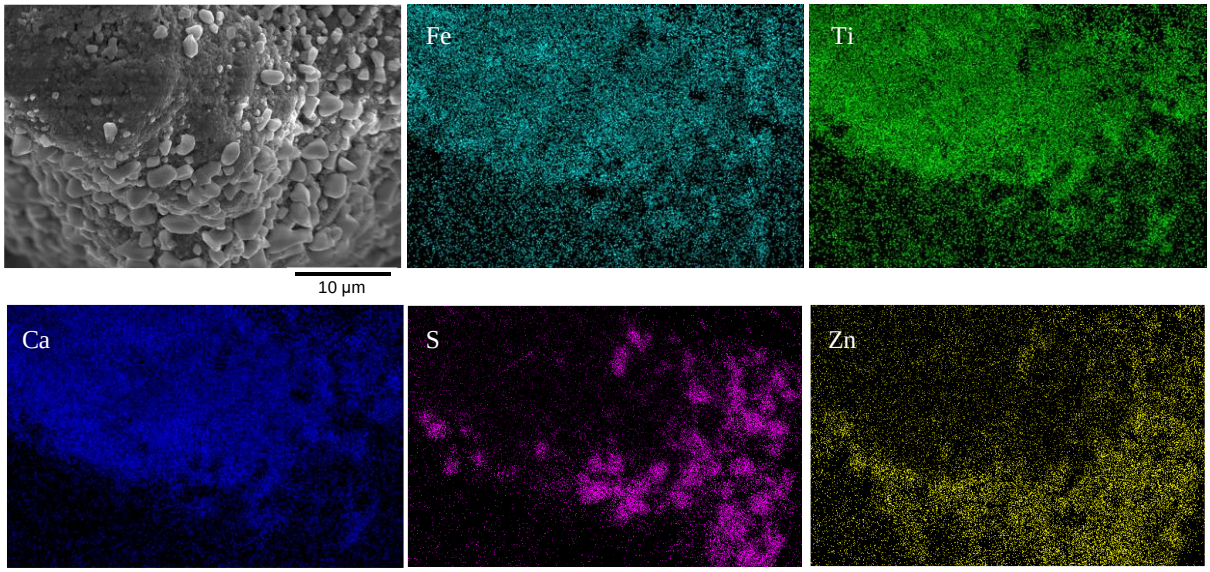

Figure 23. Surface micrograph of ilmenite after experiments with metallic Zn, along with the chemical mappings of the ash elements Ca and S, as well as Fe, Ti, and Zn. The ash layer on the ilmenite particle was formed during OCAC of RWW.

High SO_2 concentrations can also increase the stability of $CaSO_4$. The formation of Ca-sulfates, instead of Ca-silicates, will lead to an increase in the amount of slag. This is because Ca-silicates have higher melting points than alkali silicates. This will also affect the heavy metals, especially Cu and Pb, which are partially dissolved in the slag phase, resulting lower levels of Cu- and Pb-chlorides in the gas phase. The levels of Zn-chlorides decrease slightly as the concentration of S increases, although the metal is less-affected by changes in S.

Alkali metals. The concentrations of alkali metals govern the availability of the abovementioned elements for heavy metals. An increase in temperature can lead to the formation of an oxide slag phase, consisting of SiO_2, $(K, Na)AlO_2$, $(K, Na)_2O$, Cu_2O, PbO, ZnO, etc. The higher the temperature, the more slag is formed, leading to more metals being associated with this phase. Under oxidizing conditions, increasing the concentration of alkalis will lead to more alkali chlorides and more slag. This implies that there would be less $ZnCl_2$, CuCl, and $PbCl_2$ in the gas and, instead, an increase in the corresponding oxides in the melt. Besides this, the alkali metals can interact with the OC to form ferrites, titanates or ash layers surrounding the particles. This could also have implications for the heavy metal speciation. Capturing alkalis in the OC will result in less alkali in the gas phase, implying a higher availability of Cl for the heavy metals. Thus, it is also important to understand the reactions between alkali metals and OCs.

One example of the distribution of K and Na after OCAC of RWW is shown in Figure 24. The figure shows the micrograph and the associated factors after treating the chemical maps with positive matrix factorization. The factors correlate to different phases within the sample. Factor 1 is the Fe-rich phase within the ilmenite. Factor 2 represents the ilmenite that has interacted

with the ash, and it is rich in Ca. Factor 3 represents feldspar particles, which constitute 16% of the sample. Factor 4 represents the phosphates that coat the ilmenite particles. It is observed that most of the K is found in feldspars ($KAlSi_3O_8$), while Na, in the form of Na-phosphates, coats the ilmenite particles. There is a clear distinction between the alkali metals K and Na in this figure. Biomass fuels generally contain higher concentrations of K, so there has been less focus on Na and its interactions with OCs. However, when utilizing waste-derived fuels, the concentrations of Na can exceed those of K. It is shown here that there may be a difference in the associated compounds between the alkali metals.

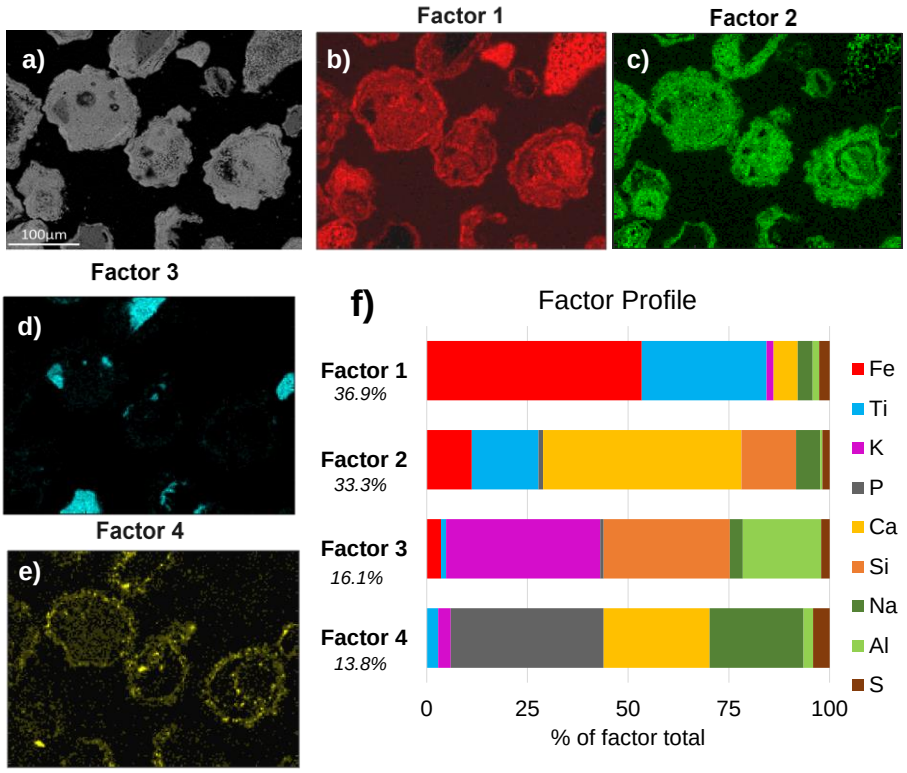

Figure 24. (a) Cross-sectional micrograph of ilmenite from OCAC of RWW after heating at 1,000ºC for 10 h. The four-factor solution is presented in panels (b–e). Panel (f) shows the fraction of each factor in the sample and the elemental contribution to each factor.

7.6 Chemical Transformations during CLC of Solid Fuels

A thermodynamic investigation was carried out for Fe-based and Mn-based OCs for CLC of solid fuels, more specifically for branches and treetops (BT) and RWW. The study utilized pure Mn-oxides and Fe-oxides, as well as more conventional materials such as ilmenite and Mn-ore. Moreover, the database DFTA was employed, which contains thermodynamic data obtained from first principles; a complete list of these compounds is provided in Table A3 in the *Appendix*. This distinguishes this investigation from the previous analyses presented in Sections 7.2-7.4, where only Fact-databases and HSCA were employed. The aim here was to gain a better understanding of the behaviors of inorganic species under conditions in the FR and AR modeled at levels that have been shown to be relevant to CLC operation.

The effect of the OC on the total gas-phase release of S, Cl, K, Na, Zn, Cu and Pb is presented in Table 14. According to the table, there are substantial differences in terms of the amounts of the problematic ash elements that are released to the gas phase. Since BT contains the lowest amount of S, Cl, and ash, even if the release is 100%, the total mass released can still be lower than for RWW. This is illustrated by the colors, where green corresponds to the highest released mass and red the lowest released mass, and the clear cells represent the gas-phase release in between.

Table 14. Weight percents of elements released to the gas phase in the FR during CLC of BT and RWW. Results shown are for the OCs Mn-oxide, Mn-ore, Fe-oxide and ilmenite. The highest (green) and lowest (red) amounts released are indicated in the table.

Release to the gas phase [wt% of the total amount]	**BT**				**RWW**			
Oxygen Carrier	**Mn-oxide**	**Mn-ore**	**Fe-oxide**	**Ilmenite**	**Mn-oxide**	**Mn-ore**	**Fe-oxide**	**Ilmenite**
S	64.1	82.7	99.98	99.97	41.2	52.7	62.3	96.7
Cl	100	100	100	100	100	100	100	100
K	30.3	0.01	13.1	0.89	78.9	0.03	11.7	6.8
Na	5.4	0.00	2.13	0.35	7.7	0.00	1.9	4.4
Zn	0.04	0.02	0.1	98.94	0.03	0.02	0.03	29.7
Cu	0.04	0.00	0.6	0.5	0.04	0.00	0.1	0.00
Pb	99.93	96.09	100	99.99	99.92	88.12	99.96	99.3

Zn shows a clear difference in behavior between the OCs. For Mn-based OCs, Zn is found in the monoxide-phase (Zn, Mn, Fe)O, while for Fe-oxide it is bound in the spinel as $ZnFe_2O_4$. For ilmenite, almost all the Zn is released to the gas phase, as all of the Fe is bound to ilmenite or titania spinel ($FeTiO_3$ or $FeTi_2O_4$) and these solid solutions do not dissolve Zn. Instead, Zn forms solid ZnS and Zn-silicates, such as willemite, olivine, and melilite. In the AR, a majority of the Zn is found as a spinel for both Fe-based OCs. In the AR, oxidation of ilmenite forms hematite and rutile, which means that the Fe is free to interact, and the conditions across the Fe-based OCs are more alike. Based on the observations described in Section 7.2.2.2, it is expected that the interaction between ilmenite and Zn will be enhanced after several reduction and oxidation cycles when Fe migrates to the ilmenite particle surfaces. As has been discussed previously, the Fe decoupling from the Ti has been observed in several studies. This effect is understandable considering the stability of the system at oxidizing conditions, but this work also shows that it can have implications for the trace element speciation.

Looking at the Cu distribution in the FR, only a small amount (<0.5 wt%) was found in the gas phase in the form of CuCl or Cu. The formation of Cu_5FeS_4 (s) is specific for Fe-oxide, while Cu_2S/Cu_2O in the slag was stable for ilmenite. For RWW, it was not uncommon that Cu_3As was formed. For the two Mn-based OCs, Cu was partly found in the monoxide phase as (Mn,Fe,Cu)O, and partly in the slag (Cu_2O). For all the investigated OC-fuel combinations in the AR, the Cu_2O in the slag was almost exclusively stable.

For Pb, the situation in the FR was more or less identical for all the investigated OC-fuel combinations. Over 99% of the total Pb introduced by the fuel exited the FR as PbS(g) and Pb(g). The Mn-ore showed the greatest propensity to retain Pb in the slag as PbS and PbO. For the Mn-ore, in the AR, no gaseous compounds were formed and instead the Pb was fully dissolved in the slag as PbO. For the other OCs, when the slag phase was carried over to the AR, it led to the release of Pb to the gas phase in the form of PbO(g).

The fact that a significant fraction of the inorganic species is released to the gas phase in the FR could be an advantage with respect to utilization of the CLC technology. The worst corrosion-related issues are expected in the FR for all the fuels and OCs investigated in this work. Furthermore, Table 14 shows that using Mn-ore as an OC for CLC of solid fuels will result in the lowest levels of alkali and heavy metals released to the gas phase, closely followed by ilmenite.

7.7 Implications for Operation, Recycling and Environment

The use of OCs for thermochemical conversion of biomass and waste-derived fuels could have environmental benefits with lower emissions of impurities and costs for carbon capture. Such chemical looping technologies have the potential to play a vital role in reaching the climate targets. It is shown in this thesis that OCs will affect the fates of inorganic species. By utilizing OCs, the metals Cu and Zn were captured in the bed. This is, partly, due to the Cu- and Zn-ferrites which have been observed and predicted widely throughout this thesis. These observations have certain implications for chemical looping operation, recycling and the environment:

- Interactions between OCs and heavy metals will prevent their release to the gas phase. This implies that corrosion-related problems could potentially be lower when implementing OCs. Not only due to their interactions with heavy metals but also alkali metals, prohibiting their release to the gas phase. Furthermore, there are certain benefits in implementing OC in dual fluidized bed systems as corrosive compounds will be concentrated in the outlet of one reactor, the FR. The gas flow in the FR is much lower than that in the AR [144], meaning that the inorganic species will be concentrated in a minor stream, which is an advantage for metal extraction. This also means that the AR is expected to be less prone to high-temperature corrosion. As the heat extraction will mostly take place in this reactor this could mean that higher steam temperatures can be used, enabling higher electrical efficiencies.
- Regarding the implication on the OC performance, the formation of these ferrites should not prohibit the oxygen transport capacity, as Cu-ferrites [145] and Zn-ferrites [146] have previously been studied as oxygen carriers. It is expected that the major ash components could have a more adverse influence.
- High concentrations of heavy metals in the FA affect the toxicity, handling cost, and utilization of the ash. By utilizing OCs, the heavy metal concentrations in the FAs could be lowered, which could be an advantage with respect to obtaining a more benign FA fraction.
- The choice of OC influences the behavior of the ash elements (Table 14) showing that there is a possibility to steer where the inorganic species should accumulate. If metal recycling from FA is desired, then implementing ilmenite in CLC would bear the benefit of prohibiting the gaseous release of alkali metals while allowing zinc to accumulate in the FA.
- Chemical looping could potentially be used to enrich OCs with precious metals before recycling. This is also possible in bed mixtures of for example ilmenite and silica sand because a metal-rich fraction can easily be obtained by magnetic separation.

8

RESULTS AND DISCUSSION PART II

This section will discuss the advances made in TECs for studying OC-ash interactions and the chemical speciation of heavy metals. The results obtained from multicomponent, multiphase equilibrium calculations are highly dependent upon the databases. Both the size of the database and the quality of the data are crucial. A major limitation associated with these databases has been the availability of experimental data. This has been a significant obstacle for constructing phase diagrams and simulating chemical looping processes, as well as for predicting the chemistries of ash components and their interactions with OCs. In this work, two different measures were taken to improve the outcomes of the calculations using the methodology presented in Figure 7. One possibility to expand the databases with these compounds is to find thermodynamic data and create a user-defined database. This was done using data available in the HSC Chemistry 9 and 10 databases. Another possibility is to obtain thermodynamic properties from first principles. These methods will be discussed in greater detail in the following sections. The compounds utilized in the HSCA and DFTA databases are presented in Tables A1 and A2 in *Appendix*.

To study the heavy metal subsystems using TECs, it is first important that the interactions between OCs and major/minor ash species are well-established. Therefore, Fe-based and Mn-based systems were evaluated concerning these ash components. Mixtures of OCs and salts were exposed to oxidizing and reducing conditions relevant to combustion. A summary of the identified interacting compounds is presented in Table 15. The table shows the crystalline phases formed due to interaction with the OC, and the influences of the support materials of the synthesized OCs MnSi, MnSiTi, MnFe and MnFeAl.

Table 15. Crystalline phases determined by XRD of compounds formed by interactions between the Mn-based and Fe-based OCs and the Ca-, K-, and P-based ash components. Identified crystalline phases for hematite, ilmenite, and pure Mn-oxide, along with the influences of the support material on the formed compounds, are described.

		Ash compound		
Oxygen Carrier	Interaction with:	$CaCO_3$	K_2CO_3	$CaHPO_4$
Mn_2O_3	Mn	$CaMn_2O_4$ $CaMnO_{3-\delta}$ $CaMn_7O_{12}$	K_2MnO_4 KMn_2O_4 K_3MnO_4	$Ca_{19}Mn_2(PO_4)_{14}$
MnSi	Si	$CaMn_{14}SiO_{24}$ $CaSiO_3$	$K_2Si_4O_9$ K_2SiO_3	
MnSiTi	Ti	$CaTiO_3$	$K_3Ti_4O_9$ $K_2Ti_2O_5$	
MnFe	Fe	$Ca_2Fe_2O_5$	$KFeO_2$ K_2FeO_4	$Ca_9Fe(PO_4)_7$
MnFeAl	Al	$Ca_2(Fe,Al)_2O_5$	$KAlO_2$	$Ca_9(Fe,Al)(PO_4)_7$
Fe_2O_3	Fe	$Ca_2Fe_2O_5$	$KFeO_2$ K_3FeO_4	
Fe_2TiO_5	Fe, Ti		$K_xFe_xTi_{1-x}O_2$* $K_2Ti_2O_5$ KTi_8O_{16}	

* x= 0.4, 0.85.

The phases observed for Fe-based OCs correlated well with the predicted phases, with the exceptions of the potassium-induced phases of $K_xFe_xTi_{1-x}O_2$ and $K_xFe_yO_z$. For the Mn-based OCs, the discrepancy was large for all the ash components and the interactions between Mn-based OCs and ash could not be described adequately with the existing data. At the time of the study, the FactSage 7.2 package and associated phases were utilized, and data were missing for the following phases: KTi_8O_{16}, $KFeO_2$, K_3FeO_4, $K_xFe_xTi_{1-x}O_2$ (x=0.4, 0.85), $CaMnO_{3-\delta}$, $CaMn_2O_4$, K_2MnO_4, K_3MnO_4, $CaMn_{14}SiO_{24}$, $CaMn_7O_{12}$, and $Ca_{19}Mn_2(PO_4)_{14}$. The updates issued following FactSage ver. 7.2 have expanded the databases and optimized the solid solutions relevant to studying OC chemistry. For example, $KFeO_2$ was added in FactSage update 7.3. Clearly, the oxide systems K-Fe, K-Ti, K-Mn and Ca-Mn are still not well-described and the major limitation for expanding the thermodynamic databases has been the limited amount of experimental data. To circumvent this problem, standard enthalpies and entropies of formation, as well as the temperature variation of the heat capacity, were estimated based on firstprinciple calculations. The procedure used to calculate the thermodynamic properties from first principles is presented in detail in **Paper VII**.

8.1 Iron-based Systems

The thermodynamic properties were first calculated from first principles for the reference compound $FeTiO_3$. A comparison with the values in the FactPS database showed remarkably good agreement. More precisely, the difference was less than 5 J/(mol K) for the entropy as well as the heat capacity, and 2 J/mol in the case of the enthalpy over a wide temperature range (293.15–1,200 K). Here, the influences of the calculated data on the phase diagrams will be discussed in more detail. The influence of the calculated Fe-based compounds on the Fe-Ti-K phase diagrams is shown in Figure 25. It is evident that the compounds KTi_8O_{16}, K_2FeO_2, and K_4FeO_3 are formed at low and high concentrations of K, respectively, and only under reducing conditions.

While certain phases are considered stable, a slow reaction could prevent the most stable thermodynamic phase to form. As shown in Figure 25, the compounds $K_xFe_xTi_{1-x}O_2$ (x=0.4, 0.85) are not deemed to be stable, although they have been observed experimentally. Assuming that the formation of K-titanates is slow, investigating the phase diagram reveals the formation of $K_{0.4}Fe_{0.4}Ti_{0.6}O_2$ under both oxidizing and reducing conditions. When ilmenite is oxidized, the outermost layer of the particle is exposed to the highest oxygen concentration. With continuous oxidation and reduction cycles, Fe migrates to the surface of the particle. This indicates that the distributions of Fe and Ti are not equal throughout the particle. This effect is not captured by the global equilibrium calculations, as these variations occur within ilmenite particles, achieving local equilibrium. Local equilibrium calculations are, therefore, useful to study and understand specific subsystems, such as K-Ti-O in this case.

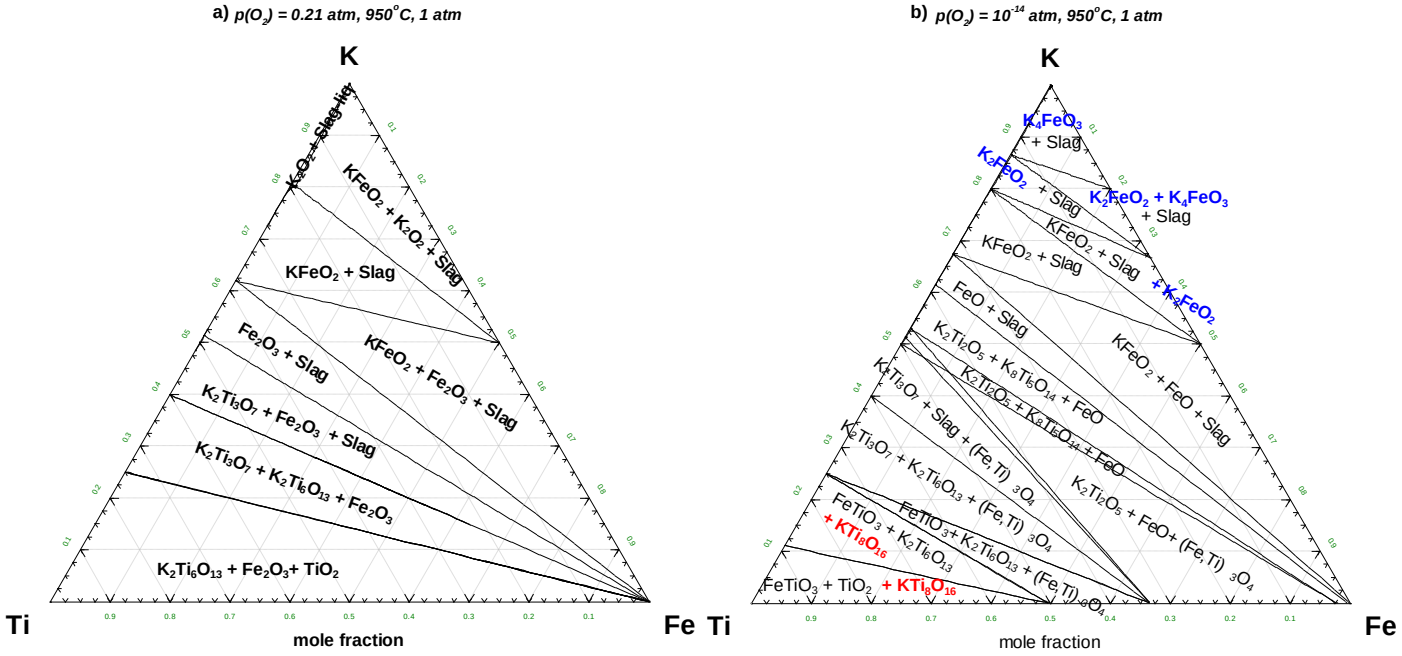

Figure 25. Ternary phase diagram of K-Ti-Fe at 950°C a) under oxidizing conditions of pO_2=0.21 atm, and b) reducing conditions of $pO_2 = 10^{-14}$ atm. Calculations were performed in FactSage 8.2 with the FactPS, FToxid, HSCA and DFTA databases. The stable phases from HSCA and DFTA are shown in blue and red respectively.

8.2 Manganese-based Systems

At the start of this work, the thermodynamic data describing Mn-based system were poor, especially concerning the important ash species Ca and K. The influence of the DFTA database on the K-Mn-O system is illustrated in Figure 26 which shows the phase diagram for K-Mn-O before and after the implementation of the DFT data. There is a remarkable difference between the two, where the interacting compound $K_xMn_yO_4$ is predicted across a wide range of oxygen partial pressures, suggesting that even though these compounds may not be stable in the global TECs they can still form in Mn-based OCs in the presence of K.

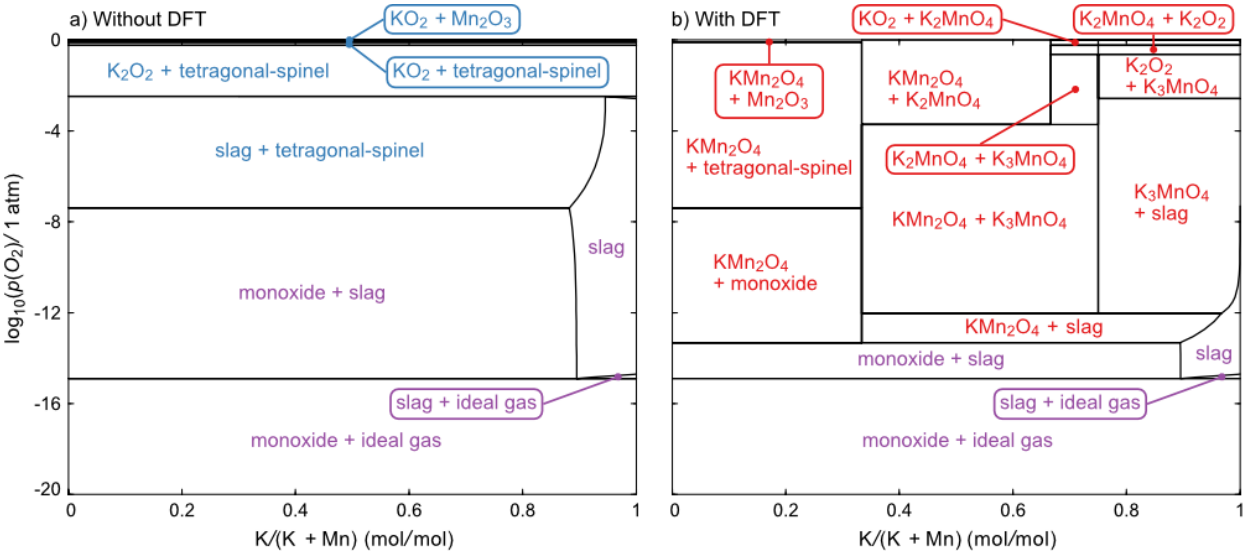

Figure 26. Phase diagram for the K-Mn-O system at 950°C and 1 atm, showing $log_{10}(p\,O_2)$ versus K/(K + Mn): a) generated using the FactPS and FToxid databases; and b) also including DFTA. Common phases have purple labels, while those colored blue and red are only present in panels a and b, respectively.

A comparison of the experimental results from **Papers I** and **II** with the data obtained here shows that the experimental findings are largely in line with the predicted compounds after implementing the DFTA database. Calculations were performed with the DFTA-database for the combination Mn_3O_4 and K_2CO_3. Under oxidizing conditions (pO_2 = 0.21 atm) TECs predict K_2MnO_4 with some KMn_2O_4, and both compounds have been reported under oxidizing conditions (**Papers I and II).** For reducing conditions (2.5% H_2, 47.5% Ar and 50% H_2O corresponding to the oxygen partial pressure $pO_2 = 10^{-13.7}$ atm) only MnO is predicted along with KOH(g). This is not aligned with Figure 26, which under the same conditions predicts KMn_2O_4 and a slag (with K_2O). However, it is the steam that enables evaporation of KOH (g) which is not captured by the phase diagram in Figure 26. For the combination Mn_3O_4 and K_2CO_3 investigated in **Paper II**, the major phases after exposure in reducing environments were MnO and K_2CO_3, with lower intensities for K_3MnO_4. This indicates that the interaction between the compounds was low. Except for the small peak observed for K_3MnO_4, the predictions are better aligned with the calculated phases after the implementation of the new DFTA database.

In this work, the thermodynamic properties of the perovskite $CaMnO_{3-\delta}$ with varying δ-values have been calculated using a semi-empirical approach. The influences of these calculated compounds on the Ca-Mn-O phase diagram are plotted in red and presented in Figure 27. The operating conditions and the range of temperatures and oxygen partial pressures within which the perovskite phase is stable are presented in the figure. This prediction agrees with previous studies examining $CaMnO_{3-\delta}$ as an OC, which have shown that it tends to decompose in favor of $CaMn_2O_4$ and $Ca_2MnO_{4-\delta}$. [147] The results obtained for the Mn-based OCs seem to be

promising in terms of their utilization in CLC of solid fuels. While the results shown here provide an overview of the stable phases, it will be of interest to validate these observations experimentally. Still, very few studies have been conducted on the ash interaction with Mn-based OCs, and specifically regarding the metals Zn, Cu and Pb.

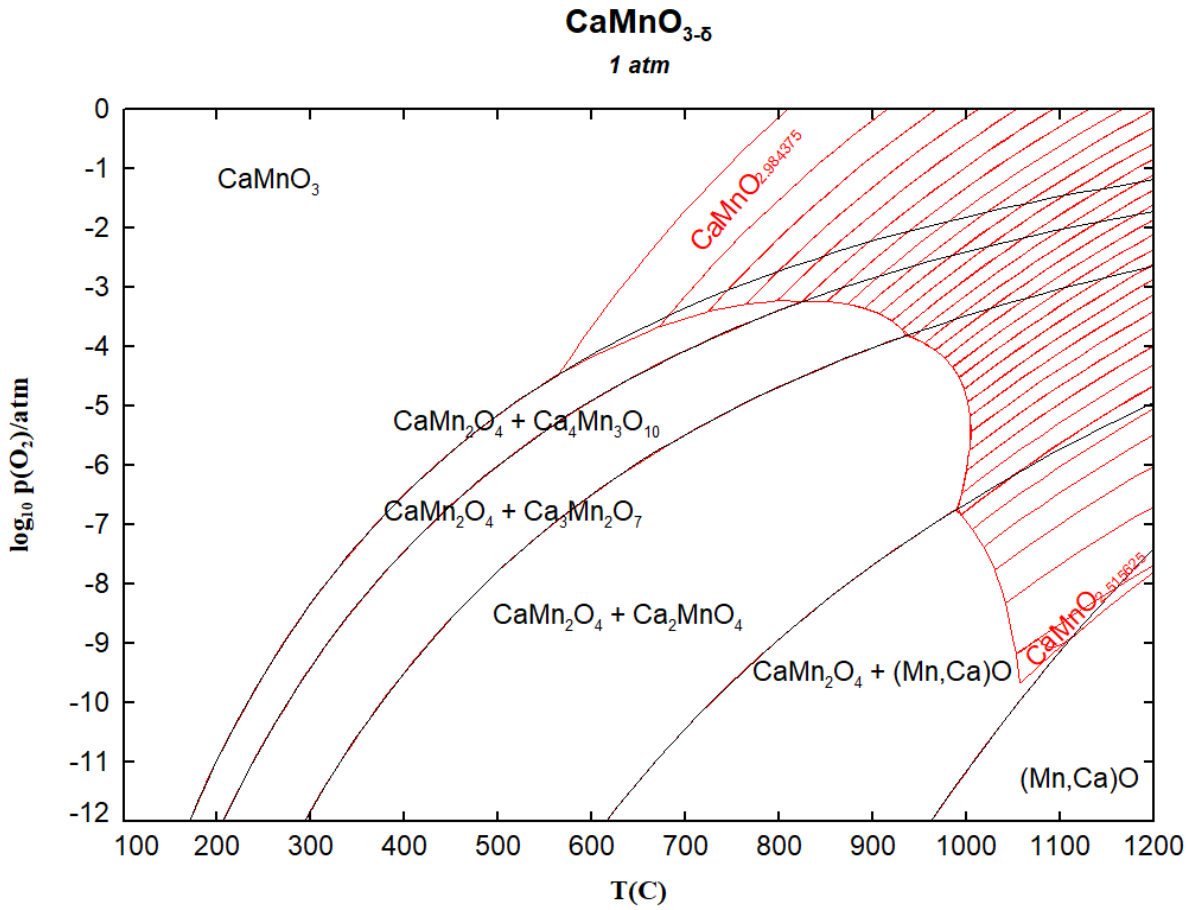

Figure 27. Stable phases in the perovskite $CaMnO_{3-\delta}$ system at 1 atm, showing $log_{10}(pO_2)$ versus temperature before and after (red) implementation of the calculated data. The phase transitions in red represent reductions (from left to right) in (3-δ) in steps of 1/64.

8.3 Limitations and Opportunities with TECs

The limitations to consider when utilizing thermodynamic calculations include: i) model assumptions; ii) kinetics; and iii) available databases. The global TECs do not consider the form of the participating elements that enter the system, the time required for combustion or the kinetics and transport phenomena. Even if equilibrium is not reached in the system, TECs are still useful for studying the system, since kinetic data are not always available for the chemical systems that pertain in the combustion system. However, it is not unreasonable to state that conditions in fluidized beds could approach equilibrium due to the good gas-solid contacts, mixing, and relatively long residence times of the solid particles. This is also indicated in Table 7 where the observed phases align well with the predicted phases. However, in boilers the temperature, pressure, and oxygen partial pressure vary temporally and spatially, but they are considered to be constant in the TEC calculations. To account for these variations a range of temperatures, bed materials, fuels, and oxygen partial pressures have been examined in this work.

To predict accurately the stability of phases in a system, it is important that all species are considered, and that the data is correct and consistent. If the data is incorrect, or important compounds are omitted from the calculations, the results could be wrong and misleading. In this work, important compounds in OC-ash subsystems have been identified, and an effort has been made to find and implement thermodynamic data of these missing compounds.

In fluidized bed systems, a combination of both global and local equilibrium is likely to occur, making local equilibrium calculations useful for studying specific subsystems or reactions. For example, during consecutive oxidation and reduction cycles of ilmenite, the outermost layer of the particle is exposed to the highest oxygen concentration and Fe migrates to the surface, resulting in an uneven distribution of Fe and Ti within the particle. This effect is not captured by the global TECs, which assume equal availabilities of Fe and Ti to interact with ash. However, when an Fe-rich layer forms on the surface of the particle, Ti is prevented from directly interacting with ash components and elements would need to diffuse through the outer layer to do so. When Ti is prevented from interacting with the ash, the resulting phases will be closer to the results obtained with Fe-oxide.

TECs is a powerful tool to understand and predict the fate of ash components. The results obtained here can be used to understand processes occurring in thermochemical conversion of waste-derived and biomass fuels The major limitation is the availability of thermodynamic data, although utilizing first principles to obtain these data has produced one of the most comprehensive databases to date for Fe-based and Mn-based systems. However, the opportunities with first principles extend beyond this purpose, in that the approach utilized here to obtain thermodynamic properties is applicable to almost any metal oxide. It is also convenient for obtaining the thermal properties of compounds that are not found in commercial or public databases. In addition, there may exist phases for which experimental measurements are unreliable because these are difficult to synthesize in pure form. Discrepancies may also arise due to human error and limitations of the experimental techniques used. Thus, it is likely that there exist materials for which this methodology is more cost-effective and yields more reliable estimates than experiments.

9

CONCLUSIONS

This thesis provides a rigorous and comprehensive view of the chemistry of important inorganic species. The knowledge obtained can be applied to thermochemical conversion technologies that utilize OCs. The inorganic species in focus have been the heavy metals Zn, Cu and Pb. Considering the research questions presented in Section 2, the conclusions derived from this work can be concisely summarized as follows.

1) *How are inorganic species affected by the presence of OCs?*

The influences that OCs exert on inorganic species have been studied experimentally with the focus on Fe-based OCs. It is observed that the OCs provide an additional reaction path for the ash-forming species. Studying samples derived from combustion and gasification processes that utilize OCs reveals the incorporation of Zn and Cu into the ash layer. In addition, for the OC ilmenite, there is accumulation of Cu inside the particle. When a combination of silica sand and ilmenite is utilized, it is possible to obtain an ilmenite- and Zn-rich fraction by magnetic separation. Pb is less affected by the OC and is primarily concentrated in the FA, regardless of the chemical looping technology and OC type investigated in this thesis. The presence of OCs is shown to play an important role in the fates of Zn and Cu.

2) *In what forms are inorganic species bound in OC particles?*

OC surfaces and cross-sections have been studied with electron microscopy and x-ray photoelectron spectroscopy. Thus, it was possible to observe several combined OC-heavy metal phases. For example, Zn was observed to be bound in the OC as $ZnFe_2O_4$. Further investigations with ilmenite showed that the formation of ferrites was promoted after ilmenite was subjected to several consecutive reduction and oxidation cycles, and this was due to the formation of an Fe-rich layer on the external surface. Cu was also observed on the particle surface, in the form of $CuFe_2O_4$, and in the particle cross-section, as $Cu_2Fe_2O_4$. As mentioned in the previous paragraph, the interactions between the OCs and Pb were limited. However, some Pb-silicates and Pb-titanates could be observed on the particles.

3) *How does the high reduction potential in the fuel reactor of CLC and CLG affect metal speciation?*

The influence of the reduction potential has essentially been studied using a thermodynamic equilibrium approach. The results show that the chemical speciations of Zn, Cu and Pb are highly affected by high reduction potentials i.e., low oxygen partial pressures. For example, oxygen partial pressures below 10^{-12} atm promote the sulfides Cu_2S (or Cu_3As), ZnS and PbS(g), and even lower pressures increase the stabilities of Zn(g) and Pb(g).

The phase stability during CLC of waste-derived fuels provides the first insights into the chemical speciation of important ash species such as K, Na, Zn, Cu and Pb. Alkali and heavy metals are well-known precursors for low-melting-point compounds, which can be problematic in thermal conversion systems. These inorganic species are expected to either exit with the gas in the FR or stabilize in the OC. The results show that a major fraction of the problematic inorganic compounds leave with the gas in the FR. This is beneficial in dual fluidized bed systems, as it can have positive implications for corrosion of the heat transfer surfaces in the AR.

4) *Can multicomponent, multiphase equilibrium calculations predict the fates of inorganic species, and what measures can be taken to improve the predictive potential of this approach?*

To improve the predictive potential of TECs, the databases have been expanded using either data from the literature or an approach based on first principles to obtain thermodynamic data regarding the experimentally identified crystalline phases. Correlating experimental observations with TECs has enabled the identification of systems that are not well described by TECs, such as the K-Fe-Ti-O, K-Mn-O and Ca-Mn-O systems. The expansion of the thermodynamic databases has contributed to the most-comprehensive thermodynamic database for Mn- and Fe-OC systems to date. After the implementation of the new data, the investigated subsystems were better aligned with the TECs. The TECs represent a powerful tool to understand and predict the fates of ash components. The obtained results can be used to understand the processes that occur during the thermochemical conversion of waste and biomass fuels.

REFERENCES

[1] IPCC. Climate Change 2014: Mitigation of Climate Change. Contribution of Working Group III to the Fifth Assessment Report of the Intergovernmental Panel on Climate Change. Cambridge, United Kingdom and New York, USA; 2014.

[2] IPCC. Summary for Policymakers. In: Global warming of 1.5°C. An IPCC Special Report on the impacts of global warming of 1.5°C above pre-industrial levels and related global greenhouse gas emission pathways, in the context of strengthening the global response to the threat of climate change, sustainable development, and efforts to eradicate poverty. Geneva, Switzerland.; 2018.

[3] Gasser T, Guivarch C, Tachiiri K, Jones CD, Ciais P. Negative emissions physically needed to keep global warming below 2 °C. Nature Communications. 2015;6(1):7958.

[4] Smith P, Davis SJ, Creutzig F, Fuss S, Minx J, Gabrielle B, et al. Biophysical and economic limits to negative CO2 emissions. Nature Climate Change. 2016;6(1):42-50.

[5] Armstrong McKay DI, Staal A, Abrams JF, Winkelmann R, Sakschewski B, Loriani S, et al. Exceeding 1.5C global warming could trigger multiple climate tipping points. Science. 2022;377(6611).

[6] Rockström J, Gaffney O, Rogelj J, Meinshausen M, Nakicenovic N, Schellnhuber HJ. A roadmap for rapid decarbonization. Science. 2017;355(6331):1269-71.

[7] Gasser T, Guivarch C, Tachiiri K, Jones CD, Ciais P. Negative emissions physically needed to keep global warming below 2°C. Nature Communications. 2015;6.

[8] Azar C, Lindgren K, Obersteiner M, Riahi K, van Vuuren DP, den Elzen KMGJ, et al. The feasibility of low CO2 concentration targets and the role of bio-energy with carbon capture and storage (BECCS). Climatic Change. 2010;100(1):195-202.

[9] Smith SM, Geden O, Nemet GF, Gidden MJ, Lamb WF, Powis C, et al. The State of Carbon Dioxide Removal - 1st Edition. The State of Carbon Dioxide Removal; 2023 2023.

[10] Fajardy M, Morris J, Gurgel A, Herzog H, Mac Dowell N, Paltsev S. The economics of bioenergy with carbon capture and storage (BECCS) deployment in a 1.5 °C or 2 °C world. Global Environmental Change. 2021;68:102262.

[11] Barker T., I. Bashmakov, L. Bernstein, J. E. Bogner, P. R. Bosch, R. Dave, et al. Technical Summary. In: Climate Change 2007: Mitigation. Contribution of Working Group III to the Fourth Assessment Report of the Intergovernmental Panel on Climate Change Cambridge University Press, Cambridge, United Kingdom and New York, NY, USA.; 2007.

[12] IPCC. Climate Change 2013: The Physical Science Basis. Contribution of Working Group I to the Fifth Assessment Report of the Intergovern-mental Panel on Climate Change Cambridge University Press, Cambridge, United Kingdom and New York, NY, USA.; 2013.

[13] Kormi T, Bel Hadj Ali N, Abichou T, Green R. Estimation of landfill methane emissions using stochastic search methods. Atmospheric Pollution Research. 2017;8(4):597-605.

[14] Sharma Kapil D, Jain S. Municipal solid waste generation, composition, and management: the global scenario. Social Responsibility Journal. 2020;16(6):917-48.

[15] Eurostat. Municipal waste by waste management operations: European Commission; [Available from: https://ec.europa.eu/eurostat/databrowser/view/env_wasmun/default/table?lang=en.

[16] EuropeanCommission. Communication from the commission to the european parliament, the council, the european economic and social committee and the committee of the region - The role of waste-to-energy in the circular economy. Brussels; 2017. Contract No.: COM(2017) 34 final.

[17] Khandelwal H, Dhar H, Thalla AK, Kumar S. Application of life cycle assessment in municipal solid waste management: A worldwide critical review. Journal of Cleaner Production. 2019;209:630-54.

[18] Hoornweg D, Bhada-Tata P, Kennedy C. Environment: Waste production must peak this century. Nature. 2013;502(7473):615-7.

[19] Kaza S, Yao LC, Bhada-Tata P, Van Woerden F. What a Waste 2.0: A Global Snapshot of Solid Waste Management to 2050. Washington, DC: The World Bank; 2018.

[20] Svensk Avfallshantering 2019. Avfall Sverige 2019.

[21] This is Improbed™ - improbed Malmö, Sweden [Available from: http://improbed.com/.

[22] Leckner B, Lind F. Combustion of municipal solid waste in fluidized bed or on grate – A comparison. Waste Management. 2020;109:94-108.

[23] Thunman H, Lind F, Breitholtz C, Berguerand N, Seemann M. Using an oxygen-carrier as bed material for combustion of biomass in a 12-MWth circulating fluidized-bed boiler. Fuel. 2013;113:300-9.

[24] Moldenhauer P, Gyllén A, Thunman H, Lind F. A Scale-Up Project for Operating a 115 MWth Biomass-Fired CFB boiler with Oxygen Carriers as Bed Material2018.

[25] Lind F, Corcoran A, Andersson B, Thunman H. 12,000 Hours of Operation with Oxygen-Carriers in Industrially Relevant Scale (75,000 kWth). VGB PowerTech. 2017(7):82-7.

[26] Abanades JC, Arias B, Lyngfelt A, Mattisson T, Wiley DE, Li H, et al. Emerging CO2 capture systems. International Journal of Greenhouse Gas Control. 2015;40:126-66.

[27] Coppola A, Scala F. Chemical Looping for Combustion of Solid Biomass: A Review. Energy & Fuels. 2021;35(23):19248-65.

[28] Di Giuliano A, Capone S, Anatone M, Gallucci K. Chemical Looping Combustion and Gasification: A Review and a Focus on European Research Projects. Industrial & Engineering Chemistry Research. 2022;61(39):14403-32.

[29] Larsson A, Seemann M, Neves D, Thunman H. Evaluation of Performance of Industrial-Scale Dual Fluidized Bed Gasifiers Using the Chalmers 2–4-MWth Gasifier. Energy & Fuels. 2013;27(11):6665-80.

[30] Mattisson T, Keller M, Linderholm C, Moldenhauer P, Rydén M, Leion H, et al. Chemical-looping technologies using circulating fluidized bed systems: Status of development. Fuel Processing Technology. 2018;172:1-12.

[31] Leion H, Mattisson T, Lyngfelt A. The use of petroleum coke as fuel in chemical-looping combustion. Fuel. 2007;86(12–13):1947-58.

[32] Mattisson T, Lyngfelt A, Leion H. Chemical-looping with oxygen uncoupling for combustion of solid fuels. International Journal of Greenhouse Gas Control. 2009;3(1):11-9.

[33] Bao J, Li Z, Cai N. Interaction between iron-based oxygen carrier and four coal ashes during chemical looping combustion. Applied Energy. 2014;115:549-58.

[34] Niu Y, Tan H, Hui S. Ash-related issues during biomass combustion: Alkali-induced slagging, silicate melt-induced slagging (ash fusion), agglomeration, corrosion, ash utilization, and related countermeasures. Progress in Energy and Combustion Science. 2016;52:1-61.

[35] Gatternig B, Karl J. Investigations on the mechanisms of ash-induced agglomeration in fluidized-bed combustion of biomass. Energy and Fuels. 2015;29(2):931-41.

[36] Dong C, Jiang J, Yang Y, Zhang J, Shan L. Research on the reactivity of oxygen carrier Fe2O3 for chemical looping combustion (CLC). Asia-Pacific Power and Energy Engineering Conference, APPEEC; 2010.

[37] Jerndal E, Mattisson T, Lyngfelt A. Thermal Analysis of Chemical-Looping Combustion. Chemical Engineering Research and Design. 2006;84(9):795-806.

[38] Abad A, Adánez J, García-Labiano F, de Diego LF, Gayán P, Celaya J. Mapping of the range of operational conditions for Cu-, Fe-, and Ni-based oxygen carriers in chemical-looping combustion. Chemical Engineering Science. 2007;62(1-2):533-49.

[39] Mendiara T, Abad A, de Diego LF, García-Labiano F, Gayán P, Adánez J. Biomass combustion in a CLC system using an iron ore as an oxygen carrier. International Journal of Greenhouse Gas Control. 2013;19:322-30.

[40] Linderholm C, Schmitz M. Chemical-looping combustion of solid fuels in a 100 kW dual circulating fluidized bed system using iron ore as oxygen carrier. Journal of Environmental Chemical Engineering. 2016;4(1):1029-39.

[41] Knutsson P, Linderholm C. Characterization of ilmenite used as oxygen carrier in a 100 kW chemical-looping combustor for solid fuels. Applied Energy. 2015;157:368-73.

[42] Cuadrat A, Abad A, García-Labiano F, Gayán P, de Diego LF, Adánez J. The use of ilmenite as oxygen-carrier in a 500Wth Chemical-Looping Coal Combustion unit. International Journal of Greenhouse Gas Control. 2011;5(6):1630-42.

[43] Moldenhauer P, Rydén M, Mattisson T, Younes M, Lyngfelt A. The use of ilmenite as oxygen carrier with kerosene in a 300 W CLC laboratory reactor with continuous circulation. Applied Energy. 2014;113(0):1846-54.

[44] Liu F, Zhang Y, Chen L, Qian D, Neathery JK, Kozo S, et al. Investigation of a Canadian ilmenite as an oxygen carrier for chemical looping combustion. Energy and Fuels. 2013;27(10):5987-95.

[45] Vigoureux M, Knutsson P, Lind F. Sulfur Uptake during Oxygen-Carrier-Aided Combustion with Ilmenite. Energy & Fuels. 2020;34(6):7735-42.

[46] Corcoran A, Marinkovic J, Lind F, Thunman H, Knutsson P, Seemann M. Ash properties of ilmenite used as bed material for combustion of biomass in a circulating fluidized bed boiler. Energy and Fuels. 2014;28(12):7672-9.

[47] Corcoran A, Knutsson P, Lind F, Thunman H. Mechanism for migration and layer growth of biomass ash on ilmenite used for oxygen carrier aided combustion. Energy and Fuels. 2018;32(8):8845-56.

[48] Gyllén A, Knutsson P, Lind F, Thunman H. Magnetic separation of ilmenite used as oxygen carrier during combustion of biomass and the effect of ash layer buildup on its activity and mechanical strength. Fuel. 2020;269:117470.

[49] Hildor F, Zevenhoven M, Brink A, Hupa L, Leion H. Understanding the Interaction of Potassium Salts with an Ilmenite Oxygen Carrier Under Dry and Wet Conditions. ACS Omega. 2020;5(36):22966-77.

[50] Rydén M, Leion H, Mattisson T, Lyngfelt A. Combined oxides as oxygen-carrier material for chemical-looping with oxygen uncoupling. Applied Energy. 2013;113:1924-32.

[51] Jing D, Arjmand M, Mattisson T, Rydén M, Snijkers F, Leion H, et al. Examination of oxygen uncoupling behaviour and reactivity towards methane for manganese silicate oxygen carriers in chemical-looping combustion. International Journal of Greenhouse Gas Control. 2014;29:70-81.

[52] Azimi G, Leion H, Rydén M, Mattisson T, Lyngfelt A. Investigation of different Mn-Fe oxides as oxygen carrier for chemical-looping with oxygen uncoupling (CLOU). Energy and Fuels. 2013;27(1):367-77.

[53] Rydén M, Lyngfelt A, Mattisson T. Combined manganese/iron oxides as oxygen carrier for chemical looping combustion with oxygen uncoupling (CLOU) in a circulating fluidized bed reactor system. Energy Procedia. 2011;4:341-8.

[54] Pérez-Vega R, Abad A, Gayán P, de Diego LF, García-Labiano F, Adánez J. Development of (Mn0.77Fe0.23)2O3 particles as an oxygen carrier for coal combustion with CO2 capture via in-situ gasification chemical looping combustion (iG-CLC) aided by oxygen uncoupling (CLOU). Fuel Processing Technology. 2017;164:69-79.

[55] Mungse P, Saravanan G, Rayalu S, Labhsetwar N. Mixed Oxides of Iron and Manganese as Potential Low-Cost Oxygen Carriers for Chemical Looping Combustion. Energy Technology. 2015;3(8):856-65.

[56] Larring Y, Braley C, Pishahang M, Andreassen KA, Bredesen R. Evaluation of a mixed Fe-Mn oxide system for chemical looping combustion. Energy and Fuels. 2015;29(5):3438-45.

[57] Wang X, Gao Y, Krzystowczyk E, Iftikhar S, Dou J, Cai R, et al. High-throughput oxygen chemical potential engineering of perovskite oxides for chemical looping applications. Energy & Environmental Science. 2022;15(4):1512-28.

[58] Ahmad A, Al Mamun MA, Al-Mamun M, Huque S, Ismail M. LFO Perovskites as Oxygen Carriers for Chemical Looping Oxygen Uncoupling (CLOU). Journal of Thermal Analysis and Calorimetry. 2022;147(12):6605-13.

[59] Jing D, Mattisson T, Leion H, Rydén M, Lyngfelt A. Examination of perovskite structure CaMnO3-δ with MgO addition as oxygen carrier for chemical looping with oxygen uncoupling using methane and syngas. International Journal of Chemical Engineering. 2013.

[60] Pishahang M, Larring Y, McCann M, Bredesen R. Ca0.9Mn0.5Ti0.5O3-δ: A suitable oxygen carrier material for fixed-bed chemical looping combustion under syngas conditions. Industrial and Engineering Chemistry Research. 2014;53(26):10549-56.

[61] Pishahang M, Larring Y, Sunding M, Jacobs M, Snijkers F. Performance of Perovskite-Type Oxides as Oxygen-Carrier Materials for Chemical Looping Combustion in the Presence of H2S. Energy Technology. 2016;4(10):1305-16.

[62] Adánez-Rubio I, Mattisson T, Jacobs M, Adánez J. Development of new Mn-based oxygen carriers using MgO and SiO2 as supports for Chemical Looping with Oxygen Uncoupling (CLOU). Fuel. 2023;337.

[63] Wang M, Zhang S, Xia M, Wang M. A Theoretical Study of the Oxygen Release Mechanisms of a Cu-Based Oxygen Carrier during Chemical Looping with Oxygen Uncoupling. Catalysts. 2022;12(3).

[64] Sundqvist S, Khalilian N, Leion H, Mattisson T, Lyngfelt A. Manganese ores as oxygen carriers for chemical-looping combustion (CLC) and chemical-looping with oxygen uncoupling (CLOU). Journal of Environmental Chemical Engineering. 2017;5(3):2552-63.

[65] Sundqvist S, Arjmand M, Mattisson T, Rydén M, Lyngfelt A. Screening of different manganese ores for chemical-looping combustion (CLC) and chemical-looping with oxygen uncoupling (CLOU). International Journal of Greenhouse Gas Control. 2015;43:179-88.

[66] Frick V, Rydén M, Leion H, Mattisson T, Lyngfelt A. Screening of supported and unsupported Mn–Si oxygen carriers for CLOU (chemical-looping with oxygen uncoupling). Energy. 2015;93, Part 1:544-54.

[67] Azimi G, Mattisson T, Leion H, Rydén M, Lyngfelt A. Comprehensive study of Mn–Fe–Al oxygen-carriers for chemical-looping with oxygen uncoupling (CLOU). International Journal of Greenhouse Gas Control. 2015;34(0):12-24.

[68] Arjmand M, Frick V, Rydén M, Leion H, Mattisson T, Lyngfelt A. Screening of combined Mn-Fe-Si oxygen carriers for chemical looping with oxygen uncoupling (CLOU). Energy and Fuels. 2015;29(3):1868-80.

[69] Abad A, García-Labiano F, Gayán P, de Diego LF, Adánez J. Redox kinetics of CaMg0.1Ti0.125Mn0.775O2.9−δ for Chemical Looping Combustion (CLC) and Chemical Looping with Oxygen Uncoupling (CLOU). Chemical Engineering Journal. 2015;269:67-81.

[70] Sundqvist S, Arjmand M, Mattisson T, Leion H, Rydén M, Lyngfelt A. Screening of different manganese ores for chemical-looping combustion (CLC) and chemical looping with oxygen uncoupling (CLOU). 11th International Conference on Fluidized Bed Technology, CFB 2014; 2014; Beijing: Chemical Industry Press.

[71] Rydén M, Leion H, Mattisson T, Lyngfelt A. Combined oxides as oxygen-carrier material for chemical-looping with oxygen uncoupling. Applied Energy. 2014;113:1924-32.

[72] Azimi G, Mattisson T, Leion H, Rydén M, Lyngfelt A. Comprehensive study of Mn–Fe–Al oxygen-carriers for chemical-looping with oxygen uncoupling (CLOU). International Journal of Greenhouse Gas Control. 2014;34:12-24.

[73] Leion H, Knutsson P, Steenari BM. Experimental evaluation of interactions between K, Ca and P and Mn/Si-based oxygen carriers. European Biomass Conference and Exhibition Proceedings; 2017: ETA-Florence Renewable Energies.

[74] Strömberg B. Miljö- och förbränningsteknik - Bränslehandboken. Värmeforsk, Värmeteknisk Forskning och Arbete: Värmeforsk; 2005.

[75] Determination of the fossil carbon content in combustible municipal solid waste in Sweden. Avfall Sverige Utveckling Report U2012:02; 2012.

[76] Pissot S, Berdugo Vilches T, Maric J, Cañete Vela I, Thunman H, Seemann M. Thermochemical Recycling of Automotive Shredder Residue by Chemical-Looping Gasification Using the Generated Ash as Oxygen Carrier. Energy & Fuels. 2019;33(11):11552-66.

[77] Humar M, Jermer J, Peek R. Regulations in the European Union with Emphasis on Germany, Sweden and Slovenia. 2006. p. 37-57.

[78] Krook J, Mårtensson A, Eklund M. Metal contamination in recovered waste wood used as energy source in Sweden. Resources, Conservation and Recycling. 2004;41(1):1-14.

[79] Senior C, Granite E, Linak W, Seames W. Chemistry of Trace Inorganic Elements in Coal Combustion Systems: A Century of Discovery. Energy & Fuels. 2020;34(12):15141-68.

[80] Camerani M, Somogyi A, Drakopoulos M, Steenari B. Synchrotron radiation induced μ–X-ray fluorescence spectroscopy on municipal solid waste fly ashes. Spectrochimica Acta Part B. 2001;56:1355-65.

[81] Camerani Pinzani M. Cadmium distribution and speciation by synchrotron radiation induced X-ray microprobe technologies. Gothenburg: Chalmers University of Technology; 2003.

[82] Golding A, Bigelow C, Veneman L. Concentrations of metals in ash from municipal solid waste combustors. Chemosphere. 1992;24:271-80.

[83] Stinespring CD, Stewart GW. Surface enrichment of aluminosilicate minerals and coal combustion ash particles. Atmospheric Environment (1967). 1981;15(3):307-13.

[84] Camerani MC, Somogyi A, Vekemans B, Ansell S, Simionovici AS, Steenari B-M, et al. Determination of the Cd-Bearing Phases in Municipal Solid Waste and Biomass Single Fly Ash Particles Using SR-μXRF Spectroscopy. Analytical Chemistry. 2007;79(17):6496-506.

[85] Clarke LB, Sloss LL. Trace elements - emissions from coal combustion and gasification. United Kingdom.1992. 111 p.

[86] Backman R, Hupa M, Hiltunen M, Peltola K. Interaction of the Behavior of Lead and Zinc With Alkalis in Fluidized Bed Combustion or Gasification of Waste Derived Fuels. 18th International Conference on Fluidized Bed Combustion. 2005.

[87] Khan AA, de Jong W, Jansens PJ, H. S. Biomass combustion in fluidized bed boilers: Potential problems and remedies. Fuel Processing Technology. 2009;90:21-50.

[88] Spiegel M. Shreir's Corrosion In: Cottis B, Graham M, Lindsay R, Lyon S, Richardson T, Scantlebury D, et al., editors. Oxford: Elsevier; 2010. p. 316-30.

[89] Ma W, Wenga T, Frandsen FJ, Yan B, Chen G. The fate of chlorine during MSW incineration: Vaporization, transformation, deposition, corrosion and remedies. Progress in Energy and Combustion Science. 2020;76:100789.

[90] Hupa M. Ash-related issues in fluidized-bed combustion of biomasses: Recent research highlights. Energy and Fuels. 2012;26(1):4-14.

[91] Edo M, Björn E, Persson P-E, Jansson S. Assessment of chemical and material contamination in waste wood fuels – A case study ranging over nine years. Waste Management. 2016;49:311-9.

[92] Karlfeldt Fedje K, Andersson S. Zinc recovery from Waste-to-Energy fly ash – A pilot test study. Waste Management. 2020;118:90-8.

[93] Schlumberger S, Schuster M, Ringmann S, Koralewska R. Recovery of high purity zinc from filter ash produced during the thermal treatment of waste and inerting of residual materials. Waste management & research : the journal of the International Solid Wastes and Public Cleansing Association, ISWA. 2007;25(6):547-55.

[94] Tang J, Steenari B-M. Leaching optimization of municipal solid waste incineration ash for resource recovery: A case study of Cu, Zn, Pb and Cd. Waste Management. 2016;48:315-22.

[95] Nagib S, Inoue K. Recovery of lead and zinc from fly ash generated from municipal incineration plants by means of acid and/or alkaline leaching. Hydrometallurgy. 2000;56(3):269-92.

[96] Jiao F, Zhang L, Song W, Meng Y, Yamada N, Sato A, et al. Effect of inorganic particulates on the condensation behavior of lead and zinc vapors. Proceedings of the combustion institute. 2013;34:2821-9.

[97] Häggström G, Karl Hannl T, Holmgren P, Broström M, Skoglund N, Öhman M. Fate of phosphorus in pulverized fuel co-combustion of sewage sludge and agricultural residues. Fuel. 2023;335:127059.

[98] Reinmöller M, Schreiner M, Laabs M, Scharm C, Yao Z, Guhl S, et al. Formation and transformation of mineral phases in biomass ashes and evaluation of the feedstocks for application in high-temperature processes. Renewable Energy. 2023;210:627-39.

[99] Niazi S, Bonk A, Hanke A, Baben MT, Reis B, Olsen E, et al. Thermal stability, hydrolysis and thermodynamic properties of molten KCl-CuCl. Materialia. 2022;21.

[100] Frandsen FJ, Dam-Johansen K, Rasmussen P. Trace elements from combustion and gasification of coal—An equilibrium approach. Progress in Energy and Combustion Science. 1994;20(2):115-38.

[101] Darwish E, Yılmaz D, Leion H. Experimental and Thermodynamic Study on the Interaction of Copper Oxygen Carriers and Oxide Compounds Commonly Present in Ashes. Energy & Fuels. 2019;33(3):2502-15.

[102] Bostrom D, Skoglund N, Grimm A, Boman C, Ohman M, Brostrom M, et al. Ash Transformation Chemistry during Combustion of Biomass. Energy & Fuels. 2012;26(1):85-93.

[103] Becidan M, Sørum L, Lindberg D. Impact of Municipal Solid Waste (MSW) Quality on the Behavior of Alkali Metals and Trace Elements during Combustion: A Thermodynamic Equilibrium Analysis. Energy & Fuels. 2010;24(6):3446-55.

[104] Konttinen J, Backman R, Hupa M, Moilanen A, Kurkela E. Trace element behavior in the fluidized bed gasification of solid recovered fuels – A thermodynamic study. Fuel. 2013;106:621-31.

[105] Malcolm W. Chase, Jr. NIST-JANAF thermochemical tables: Fourth edition. Washington, DC : American Chemical Society ; New York : American Institute of Physics for the National Institute of Standards and Technology, 1998.; 1998.

[106] Belov GV, Dyachkov SA, Levashov PR, Lomonosov IV, Minakov DV, Morozov IV, et al. The IVTANTHERMO-Online database for thermodynamic properties of individual substances with web interface. Journal of Physics: Conference Series. 2018;946:012120.

[107] Dinsdale A. SGTE Data for Pure Elements. Calphad. 1991;15:317-425.

[108] Davies RH, Dinsdale AT, Gisby JA, Robinson JAJ, Martin SM. MTDATA - thermodynamic and phase equilibrium software from the national physical laboratory. Calphad. 2002;26(2):229-71.

[109] Andersson JO, Helander T, Höglund L, Shi PF, Sundman B. Thermo-Calc and DICTRA Computational tools for materials science. Calphad. 2002;26:273-312.

[110] Roine. A. HSC Chemistry® [Software], Outotec, Pori 2018 [Available from: www.outotec.com/HSC.

[111] Bale CW, Bélisle E, Chartrand P, Decterov SA, Eriksson G, Gheribi AE, et al. FactSage Thermochemical Software and Databases - 2010 - 2016. Calphad. 2016;54:35-53.

[112] Talonen T. Chemical Equilibria of Heavy Metals in Waste Incineration: Comparison of Thermodynamic Databases [Licentiate]: Åbo Akademi University; 2008.

[113] Lundholm K, Nordin A, Backman R. Trace element speciation in combustion processes—Review and compilations of thermodynamic data. Fuel Processing Technology. 2007;88(11):1061-70.

[114] Lindberg D, Backman R, Chartrand P, Hupa M. Towards a comprehensive thermodynamic database for ash-forming elements in biomass and waste combustion — Current situation and future developments. Fuel Processing Technology. 2011;105:129-41.

[115] Kuba M, He H, Kirnbauer F, Skoglund N, Boström D, Öhman M, et al. Mechanism of layer formation on olivine bed particles in industrial-scale dual fluid bed gasification of wood. Energy and Fuels. 2016;30(9):7410-8.

[116] Frandsen F, Dam-Johansen K, Rasmussen P. GFEDBASE — A pure substance trace element thermochemical database. Calphad. 1996;20(2):175-229.

[117] Kramb J, Konttinen J, Backman R, Salo K, Roberts M. Elimination of arsenic-containing emissions from gasification of chromated copper arsenate wood. Fuel. 2016;181:319-24.

[118] Enestam S, Backman R, Mäkelä K, Hupa M. Evaluation of the condensation behavior of lead and zinc in BFB combustion of recovered waste wood. Fuel Processing Technology. 2013;105:161-9.

[119] Moulder JM, Stickle WF, Sobol PE, Bomben Kd. Handbook of X-ray Photoelectron Spectroscopy - A Reference Book of Standard Spectra for Identification and Interpretation of XPS Data. 6509 Flying Cloud Drive Eden Prairie, Minnesota 55344 United Stales of America: Perkin-Elmer Corporation - Physical Electronics Division; 1992.

[120] NIST X-ray Photoelectron Spectroscopy Database - NIST Standard Reference Database 20, Version 4. [Internet]. National Institute of Standards and Technology. 2012. Available from: http://dx.doi.org/10.18434/T4T88K.

[121] Paatero P, Tapper U. Positive matrix factorization: A non-negative factor model with optimal utilization of error estimates of data values. Environmetrics. 1994;5(2):111-26.

[122] Norris DG, Brown S, Bai S. EPA positive matrix factorization (PMF) 5.0 fundamentals and user guide. Washington DC2014.

[123] Lyngfelt A, Leckner B. A 1000 MWth boiler for chemical-looping combustion of solid fuels – Discussion of design and costs. Applied Energy. 2015;157:475-87.

[124] Saeed MN, Shahrivar M, Surywanshi GD, Kumar TR, Mattisson T, Soleimanisalim AH. Production of aviation fuel with negative emissions via chemical looping gasification of

biogenic residues: Full chain process modelling and techno-economic analysis. Fuel Processing Technology. 2023;241:107585.

[125] Arena U. 17 - Fluidized bed gasification. In: Scala F, editor. Fluidized Bed Technologies for Near-Zero Emission Combustion and Gasification: Woodhead Publishing; 2013. p. 765-812.

[126] Störner F, Hildor F, Leion H, Zevenhoven M, Hupa L, Rydén M. Potassium Ash Interactions with Oxygen Carriers Steel Converter Slag and Iron Mill Scale in Chemical-Looping Combustion of Biomass—Experimental Evaluation Using Model Compounds. Energy & Fuels. 2020;34(2):2304-14.

[127] Adánez J, Cuadrat A, Abad A, Gayán P, Diego LFD, García-Labiano F. Ilmenite activation during consecutive redox cycles in chemical-looping combustion. Energy and Fuels. 2010;24(2):1402-13.

[128] Gogolev I, Linderholm C, Gall D, Schmitz M, Mattisson T, Pettersson JBC, et al. Chemical-looping combustion in a 100 kW unit using a mixture of synthetic and natural oxygen carriers – Operational results and fate of biomass fuel alkali. International Journal of Greenhouse Gas Control. 2019;88:371-82.

[129] Mendiara T, Pérez-Astray A, Izquierdo MT, Abad A, de Diego LF, García-Labiano F, et al. Chemical Looping Combustion of different types of biomass in a 0.5kWth unit. Fuel. 2018;211:868-75.

[130] Niu X, Shen L, Gu H, Jiang S, Xiao J. Characteristics of hematite and fly ash during chemical looping combustion of sewage sludge. Chemical Engineering Journal. 2015;268:236-44.

[131] Wang H, Liu G, Veksha A, Dou X, Giannis A, Lim TT, et al. Iron ore modified with alkaline earth metals for the chemical looping combustion of municipal solid waste derived syngas. Journal of Cleaner Production. 2021;282:124467.

[132] Goldyreva EI, Leonidov IA, Patrakeev MV, Kozhevnikov VL. Thermodynamics of oxygen in CaMnO3 − δ. Journal of Solid State Electrochemistry. 2013;17(12):3185-90.

[133] Li F, Sun Z, Luo S, Fan L-S. Ionic diffusion in the oxidation of iron—effect of support and its implications to chemical looping applications. Energy & Environmental Science. 2011;4(3):876-80.

[134] Benisek A, Dachs E. The accuracy of standard enthalpies and entropies for phases of petrological interest derived from density-functional calculations. Contributions to Mineralogy and Petrology. 2018;173(11):90.

[135] Pelton AD. Phase Diagrams and Thermodynamic Modeling of Solutions2019.

[136] Weber CF. Convergence of the Equilibrium Code SOLGASMIX. Journal of Computational Physics. 1998;145(2):655-70.

[137] Stølen S, Grande T. Thermodynamic Foundations. Chemical Thermodynamics of Materials2003. p. 1-27.

[138] Eriksson G. Thermodynamic Studies of High Temperature Equilibria. Chemica Scripta. 1975;8:100-3.

[139] Smith WR, Missen RW. Chemical Reaction Equilibrium Analysis: Wiley; 1982.

[140] Pelton AD. 15 - Multiple-Sublattice Random-Mixing (Bragg-Williams—BW) Models. In: Pelton AD, editor. Phase Diagrams and Thermodynamic Modeling of Solutions. Amsterdam: Elsevier; 2019. p. 229-52.

[141] Chartrand P, Pelton AD. The modified quasi-chemical model: Part III. Two sublattices. Metallurgical and Materials Transactions A. 2001;32(6):1397-407.

[142] Eriksson G, Königsberger E. FactSage and ChemApp: Two tools for the prediction of multiphase chemical equilibria in solutions. Pure and Applied Chemistry. 2008;80(6):1293-302.

[143] Leion H, Frick V, Hildor F. Experimental Method and Setup for Laboratory Fluidized Bed Reactor Testing. Energies. 2018;11(10):2505.

[144] Lyngfelt A, Pallarès D, Linderholm C, Lind F, Thunman H, Leckner B. Achieving Adequate Circulation in Chemical Looping Combustion─Design Proposal for a 200 MWth Chemical Looping Combustion Circulating Fluidized Bed Boiler. Energy & Fuels. 2022;36(17):9588-615.

[145] Wang B, Yan R, Zhao H, Zheng Y, Liu Z, Zheng C. Investigation of Chemical Looping Combustion of Coal with CuFe2O4 Oxygen Carrier. Energy & Fuels. 2011;25(7):3344-54.

[146] Kuo Y-L, Huang W-C, Tseng Y-H, Chang S-H, Ku Y, Lee H-Y. Electric arc furnace dust as an alternative low-cost oxygen carrier for chemical looping combustion. Journal of Hazardous Materials. 2018;342:297-305.

[147] Bakken E, Norby T, Stølen S. Nonstoichiometry and reductive decomposition of CaMnO3−δ. Solid State Ionics. 2005;176(1–2):217-23.

APPENDIX

Table A.1 Gases and solids added to the HSCA database from HSC9; the terms s, s2 and s3 denote phase transitions.

Specie	Solids	Gases
As	As_2CoO_4 As_2O_4 (s, s2) As_2CuO_4 As_4O_6 (s, s2, s3) $As_2Ni_3O_8$ As_4S_6 As_2NiO_4 AsS (s, s2)	As_4O_7 AsO_2 As_4O_8 As_2O_3 As_4O_9 As_2S_3 AsH As_4O_{10} AsH_2
C	VCO_4 C_{60} $C_2H_6O_{12}Zn_5$	C_{60} CCl_2S C_2H_6Zn
Cl	-	Cl_4 $ClHO_3S$ $ClHO_4$ ClOS Cl_3
Cr	$Cr(OH)_2$ $CrVO_4$ $Cr(OH)_3$ $CrCl_4$ $PbCrO_4$ CrCl	Cr_2 Cr_2O_2 CrS_2 Cr_2O_3 Cr_2O CrH
Co	$Co_{10}S_{8.9}$ $CoMoO_4$ $Co_6S_{7.98}$ $Co(OH)_3$	Co_2 CoO CoH CoS CoH_2O_2
Mn	Mn_2O_4Zn Cl_3Mn Mn_2NiO_4 H_2MnO_2 MnO_6V_2 $HMnO_2$ $MnCl_3$ (s, s2)	MnO MnCl MnO_2 $MnClO_3$ $MnCl_3$ MnH $MnCl_4$ MnOH
Mo	$Mo_{10}O_{28.9}$ $ZnMoO_4$ $Mo_{12}Cl_{36.96}$ $MoCl_3$ Mo_2 $MoCl_2$ $MoNiO_4$	$MoHO_2$ $MoOCl_3$ $MoCl_2$ $MoOCl_4$ MoH_2O_3 MoCl $MoOCl_2$ MoOCl $MoCl_3$ $MoClO_2$ MoS
Ni	$Ni(OH)_3$ $Ni_3V_2O_8$	Ni_2 $NiCl_3$

		Ni_2Cl_4 NiOH
Pb	$Pb_5Si_3O_{11}$ Pb_2O_3 PbS_2SiO_4 PbS_2O_3 $Pb(OH)_2$ PbS_3O_6 $K_2Pb(SO_4)_2$ PbV_2O_6 $Pb_{12}O_{17}$ $Pb_2V_2O_7$ $Pb_{12}O_{19}$ $Pb_3V_2O_8$ Pb_3CO_5 $PbCrO_4$	Pb_2S_2 PbS_2 PbO_2 PbO_3
V	CuV_2O_6 V_8O_{15} V_6O_{11} V_6O_{13} V_6O_{13} $V_4O_{4.96}$ V_7O_{13} V_5O_9	VCl_3 VCl_5 V_4O_{10} $V_2H_4O_7$
Cu	CuV_2O_6	Cu_2S Cu_2Cl_2 CuH Cu_2Cl_4 CuOH Cu_4Cl_4 $CuCl_2$ Cu_5Cl_5
Zn	$C_2H_6O_{12}Zn_5$	$Zn(OH)_2$ ZnH ZnOH ZnO C_2H_6Zn ZnCl

Table A.2 Stoichiometric solids added to the HSCA database used from HSC10.

Specie	Solids
Cu	$CuAl_2O_4$ $Cu_2Al_2O_4$ $CuCr_2O_4$ Cu_2PbO_2
Pb	PbS_2SiO_4 $PbSiO_4$ $Pb_5Si_3O_{11}$ Ca_2PbO_4 $K_2Pb(SO_4)_2$ $Pb_3(AsO_4)_2$

Table A.3 List of the phases for which thermodynamic properties have been calculated from first principles, with the exception of $CaMnO_{3-\delta}$, which was calculated based on a semi-empirical approach.

Origin	Solids
Fe/Ti-based compounds (Paper II)	KTi_8O_{16} $KTi_8O_{16.5}$ $K_{0.4}Fe_{0.4}Ti_{0.6}O_2$ $K_{0.85}Fe_{0.85}Ti_{0.15}O_2$
Mn-based compounds (Papers I and **II)**	K_2MnO_4 K_3MnO_4 KMn_2O_4 $Ca_{19}Mn_2(PO_4)_{14}$ $CaMn_{14}SiO_{24}$ $CaMnO_{3-\delta}$